DOCTOR OF SCIENCE

Laser Processed Materials for Advanced Solar Devices

Yao, Jin

Award date:
2013

DOCTOR OF SCIENCE

Laser Processed Materials for Advanced Solar Devices

Jin Yao

2014

University of Dundee

Laser Processed Materials for Advanced Solar Devices

Jin Yao

Submitted for the Degree of

Doctor of Philosophy

from the University of Dundee

School of Electrical Engineering & Physics, University of Dundee

Nethergate, Dundee, DD1 4HN, Scotland, UK

2013

Acknowledgments

The author would like to express his gratitude to Prof. M. J. Rose for supervising this research work. Many thanks are also to Dr. Y. C. Fan, Dr. S. Persheyev and Dr. S. Reynolds for their valuable advice, and also to all the helpful technicians in the department of Electrical Engineering and Physics, University of Dundee.

The author also gives the thanks to his wife – Yan Yin, his father – Zhengkang Yao, his mother – Weiji He and his son – Yanbo Louis Yao for their selfless support both on finical and spiritual.

Jin Yao

Declaration

I certify that I, the undersigned, am author of this thesis, that I have consulted all cited references, that the work in this thesis was done by me and that this work has not previously been accepted for a higher degree.

Jin Yao

Acronyms Used

2T	2-Terminal
3T	3-Terminal
AFM	Atomic Force Microscopy
AM	Active Matrix
bSi	Black Silicon
bCu	Black Copper
CIS	$CuInSe_2$
CIGS	$CuIn_xGa_{1-x}Se_2$
CNTs	Carbon Nanotubes
CRT	Cathode Ray Tube
DLC	Diamond like Carbon
EL	Excimer Laser
ELA	Excimer Laser Annealed
ELC	Excimer Laser Crystallized
ELP	Excimer Laser Processed
EPD	Electrophoretic Deposition
FE	Field Emission
FED	Field Emission Display
FN	Fowler- Nordheim

FNT	Fowler- Nordheim Theory
FPD	Flat Panel Display
FTIR	Fourier Transform Infra- Red
HWCVD	Hot- Wire Chemical Vapor Deposition
ITO	Indium Tin Oxide
LCD	Liquid Crystal Display
MEMS	Microelectromechanical Systems
MWNT	Multi Walled Nanotube
NEA	Negative Electron Affinity
PDP	Plasma Display Panel
PEA	Positive Electron Affinity
PECVD	Plasma Enhanced Chemical Vapour Deposition
PETE	Photon Enhanced Thermionic Emission
PV	Photovoltaic
QFT	Quantum Filament Technologies
OLED	Organic Light Emitting Diode
RIE	Reactive Ion Etching
RF	Radio Frequency
RTFE	Resonant Tunnelling Field Emission
SC	Solar Cells
SCIBB	Space Charge Induced Band Bending

SEM	Scanning Electron Microscopy
SWNT	Single Walled Nanotube
TCOs	Transparent Conducting Oxides
TFT	Thin Film Transistor
TE	Thermionic Emission
TEC	Thermionic Energy Converter
UoD	University of Dundee
VFE	Vacuum Field Emission

List of Symbols

B	field-independent constant of dimensions	1.4×10^{-2} A/V^2
β	field emission enhancement factor	
E	applied electric field	
Φ	work function	
J_0	emission current density	
A_0	constant	1.20×10^{6} A/m^{2}K^2
λ_R	material- specific correction factor	0.5
T	absolute substrate temperature	
k_B	Boltzmann's constant	1.38×10^{-23} J/K
e	electron charge	1.6×10^{-19} C
ε_0	electric constant	8.854×10^{-12} F/m
n	electron density in the conduction band	
χ	electron affinity	
$\langle v_x \rangle$	average velocity perpendicular to the material surface	
S	Seebeck coefficient	
k	thermal conductivity	
σ	electrical conductivity	
ρ	electrical resistivity	
α	thermal diffusivity	

Cp	heat capacity
d	material density
t_f	film thickness
n_f	**r**efractive index
FF	fill factor
η	solar cell efficiency
AM	air mass
F	electric field
U	applied voltage
D	dimension of the vacuum gap

Abstract

Crystallized hydrogenated amorphous silicon (a-Si:H) by various methods have been studied for a long time, and among these techniques, excimer laser crystallization has the merits in rapid and stable. In this PhD project, the objective of the excimer laser processing is to develop 1) crystallized a-Si:H thin film as a promising field & thermionic emission candidate, and 2) a novel dark film – black silicon, which can highly absorb lights. And finally, a thermionic emission enhanced renewable energy device is purposed, which also adopt black silicon as the sunlights absorber.

This PhD thesis starts from the investigation of excimer laser processing hydrogenated amorphous silicon which resulting in the formation of the microstructures and change of the thermal, optical and electrical properties. The goal of this research is to perform an intensively study to understand this silicon based materials by experiments.

Various thickness of the a-Si:H which leads to different applications such as 'black silicon' layer, obtained by excimer laser to process thick (~400 nm) a-Si:H layer while a thinner (100nm) laser irradiated a-Si is a novel field emitter. This film has a black surface by the direct observation. A well understanding is then established via studying the microstructure by SEM images and optical experiments.

With the principle of the fabrication of black silicon, a n-i-p junction silicon nanowire solar device was fabricated and studied by the means of excimer laser process and doping. The device is able to enhance the light trapping due to the micro structure to strengthen the solar cell efficiency compared to the conventional planar amorphous silicon solar device.

The field and thermionic emission of excimer laser irradiated thin amorphous silicon (emitter) was then investigated to develop a prototype of photon enhanced solar thermal device with the black silicon layer as the light absorber. In this device, the lights are trapped by the bSi and the heats are transformed to the emitting cathode via the copper foil between the bSi and cathode. The thermal collected from bSi and passed to the emitters then enhances the threshold field of the emitters and electrons are launched via cathode and travel to the anode to form a electricity loop.

Key words: Electron Field Emission, Thermionic Emission, Excimer Laser Processing, Black Silicon, Silicon Nanowire, Solar Cells, Solar Thermal and Amorphous Silicon.

Email: jyao@dundee.ac.uk

Contents

1.0 Introduction……..….. 1

1.1 Objectives of this Study..... 1
1.2 Background..... 2
1.3 Current Solar Cells Technologies and Market..... 2
1.4 Thesis Structure..... 6

2.0 Literature Review..... 8

2.1 Review on Silicon Based PV Technologies and Models..... 8
2.1.1 Crystalline Silicon PV Cells..... 8
2.1.2 Single - Junction Amorphous Silicon Thin Film PV Cells..... 10
2.1.3 Multi - Junction Amorphous Silicon Thin Film PV cells..... 12
2.1.4 Amorphous Silicon Schottky Barrier Solar Cells..... 13
2.2 Enhancement of Light Absorption in Solar Cells..... 13
2.2.1 Silicon Nanowire Structure Solar Cells..... 14
2.2.2 Anti-Reflection Coating 15
2.2.3 Front Textured Surface Anti-Reflection Coatings 16
2.2.4 Back Reflector Enhancement 17
2.3 Review on Excimer Laser Processing..... 1 8
2.3.1 Excimer Laser Crystallization of Hydrogenated Amorphous Silicon (a-Si:H)..... 18
2.3.2 Excimer Laser Doping..... 19
2.4 Review of Electron Field Emission Materials and Models.....19
2.4.1 Electron Field Emission Models..... 20
2.4.2 Field Emission Cold Cathode Materials..... 25
2.5 Review on Electron Thermionic Emission and Thermoelectric Effect..... 33

2.5.1 Richardson's Law..... 33
2.5.2 Schottky Emission..... 34
2.5.3 Cathode Materials of Thermionic Emission..... 34
2.5.4 Photon Enhanced Thermionic Emission (PETE) Model..... 36
2.5.5 Thermoelectric Effect and Measurements..... 39
2.6 Review on Fabrication of Black Silicon Films..... 42
2.7 Summary..... 44

3.0 Experimental Techniques..... 46

3.1 Thin Film Deposition Techniques..... 46
3.1.1 DC Sputtering of Base Metal Plates..... 46
3.1.2 Plasma Enhanced Chemical Vapor Deposition (PECVD) Technique.... 47
3.1.3 Hot Wire Chemical Vapor Deposition (HWCVD) Technique..... 49
3.2 Excimer Laser Processing Technique..... 50
3.3 Thin Film Characterization Techniques..... 52
3.3.1 Scanning Electron Microscopy (SEM) & Energy- Dispersive X- Ray Spectroscopy (EDX)..... 52
3.3.2 Transmission Electron Microscopy (TEM)..... 53
3.3.3 Fourier Transform Infra- Red Spectroscopy (FT-IR)..... 55
3.3.4 UV-VIS-NIR Spectroscopy..... 56
3.3.5 Thermoelectric Power (Thermopower) Measurement..... 57
3.3.6 Solar Cell Efficiency Measurement..... 60
3.4 Electron Field Emission and Thermionic Emission Measurement Techniques.... 61
3.4.1 Probe Type Electron Field Emission Measurement..... 62
3.4.2 Thermionic Emission Measurement..... 62
3.5 Summary..... 65

4.0 Results and Discussion: Fabrication, Surface Morphology and Optical Properties of Large Area 'Black Silicon' Films..... 66

4.1 Fabrication of Black Silicon (bSi) Film with Excimer Laser Technology..... 67
4.2 Growing Conditions of Black Silicon Films..... 71
4.3 Electrical and Optical Properties of Black Silicon Films..... 86
4.4 Comparison with Black Copper (bCu)..... 93
4.5 Summary..... 95

5.0 Results and Discussion: Single Junction Amorphous Silicon Nanowire Solar Cell..... 97

5.1 Fabrication of the n-i-p Substrate-type Device..... 98
5.2 Surface Morphology and Micro Structure of the n-i-p Substrate Junction..... 99
5.3 Optical and Electrical Measurements..... 101
5.4 Summary..... 107

6.0 Results and Discussion: Field Emission and Thermionic Emission Properties of ELP Amorphous Silicon and Carbon Nanotubes (CNTs)..... 108

6.1 Excimer Laser Processed Amorphous Silicon as Field/Thermionic Emission Cathode Materials..... 108
6.1.1 Substrate Preparation..... 109
6.1.2 Surface Morphology of ELP a-Si emitters..... 112
6.2 Synthesis of CNT Thin Film as Field/Thermionic Emission Cathode Materials. 114
6.2.1 Electrophoretic Deposition Method (EPD) for the Growth of CNTs..... 114
6.2.2 PECVD System for the Growth of CNTs..... 117
6.3 Electron Field Emission Measurements..... 120
6.3.1 ELP a-Si:H Emitters..... 120
6.3.2 CNTs Emitters..... 121

6.4 Electron Thermionic Emission Measurements..... 124
6.4.1 ELP a-Si:H Emitters..... 119
6.4.2 CNTs Emitters..... 127
6.5 Summary..... 128

7.0 Development of the Novel Solar Thermal Device..... 130

7.1 Device Structure..... 130
7.2 Device Working Principle..... 132
7.3 Summary..... 142

8.0 Summary and Future Work..... 144

8.1 Summary..... 144
8.2 Future Work..... 145
8.2.1 p-i-n Single Junction Nanowire Solar Cell Design..... 145
8.2.2 Improvements of Solar Thermionic Generator..... 147

References..... 148

List of Figures

1 Different photovoltaic technology market share in 2010. Silicon based PV cells (multi- Si, mono- Si and amorphous- Si) share roughly 93% of the solar PV energy market ……3

2 Working principle and device structure of a novel solar thermal device with excimer laser processing technique……...5

3 Schematic of standard mSi (left) and pSi (right) solar cells panels……....9

4 Formation of a substrate- type (a) and superstrate- type (b) a-Si:H solar cell……..11

5 Schematic diagram of a triple- junction cell……12

6 Schematic diagram of light trapping in an a-Si:H p-i-n solar cell……....17

7 Schematic of Cathode- Vacuum- Anode junction under high applied field…….21

8 Band diagram of (a) PEA and (b) NEA materials under an applied electric field…23

9 Produce flow of Spindt tips arrays fabrication. (a) Electrode and dielectric layer deposition on glass substrate. (b) Definition of emitter well using photolithography technique. (c) Formation of emitter well. (d) Deposition of sacrificial lift-off layer, typically aluminum, by angle evaporation. Rotation of glass substrate during deposition is indicated by arrow. (e) Tip deposition by electron beam evaporation. Tip materials are usually refractory metals such as molybdenum or niobium. Rotation of substrate is indicated by arrow. (f) Removal of sacrificial and closure layers. (g) SEM of a 3×3 array of spindt tips field emission emitters. (h) SEM of cross section of a single gated emitter cone……..26

10 Molecular structures of a single-walled carbon nanotube (SWNT) and of a multi-walled carbon nanotube (MWNT)……27

11 (a) Schematic of fully sealed CNTs FED model. (b) Emission current of CNTs and graphite as a function of electric field. (c) Emitting image of 4.5 inch fully sealed SWNT-FED at color mode with RGB phosphor columns……30

12 Schematic of a PETE device……37

13 Total PETE/thermal efficiency compared with PETE efficiency as a function of cathode bandgap at ×1000 concentration, assuming a 285^{o}C anode thermally coupled to a 31.5%- efficient thermal engine……...38

14 Seebeck coefficient, electrical conductivity, thermal conductivity, and figure of merit (ZT) with respect to free carrier concentration……41

15 Schematic of light trapping in black silicon micro spikes……43

16 Cross-section view of DC Sputtering chamber……..47

17 Cross view of PECVD chamber……48

18 Cross view of HWCVD chamber……..50

19 Schematic Diagram of KrF Excimer Laser System Layout……..50

20 Beam profile of excimer laser……...…51

21 Schematic representation of a SEM system……..53

22 Schematic of a TEM system……54

23 Working principle of a FT-IR system ……..……55

24 Schematic of UV-VIS-NIR Spectroscopy system……56

25 (a) Schematic of thermoelectric power measurement chamber. (b) Side view of the measurement substrate. (c) Top view of the measurement substrate...……58

26 Home- made thermo-power measurement system a) chamber overview, b) chamber top view and c) heating and pumping controller……...59

27 Schematic of solar cell efficiency testing chamber……...……61

28 Schematic of probe type field emission measurement……..62

29 (a) Cr anode based on glass substrate. (b) Schematic of thermionic emission system……63

30 Sample in substrate holder (upper) and TE measurement system (lower)……64

31 Schematic diagram of excimer laser microstructuring a-Si:H films using a slope beam profile, (a) top view laser beam pattern (4 mm × 8 mm), (b)top- flat beam profile along the long axis Y, (c) slope beam profile along the short axis X, (d) cross section view of the sample and the sample scan direction in ±X relative to the laser beam……..68

32 Live images of laser beam profiles both in horizontal and vertical axis (a) Gaussian, and (b) Semi-Gaussian……..68

33 Images of black silicon on Cu plate. (a) Excimer laser processed strip with substrate on X scanning direction. (b) Excimer laser processed strip with substrate on –X scanning direction…….……70

34 The mechanism for the silicon spikes array formation by ELP of a-Si. (a) Bump micro-features of the a-Si film. (b) Flow of molten liquid toward the peaks contributes to the increase in height. (c) Sharp pillar micro-features at the finish stage……71

35 SEM images of excimer laser microstructuring a-Si:H film on Mo substrate with different laser energy. (a,b) 160 mJ, (c,d) 180 mJ, (e,f) 200 mJ, (g,h) 220 mJ. With an overall viewing angle of 20^{o} to the surface normal……74

36 SEM images of excimer laser microstructuring a-Si:H film on Cr substrate with different laser energy. (a,b) 160 mJ, (c,d) 180 mJ, (e,f) 200 mJ, (g,h) 220 mJ. With an overall viewing angle of 20^{o} to the surface normal……76

37 SEM images of excimer laser microstructuring a-Si:H film on Al substrate with different laser energy. (a,b) 160 mJ, (c,d) 180 mJ, (e,f) 200 mJ, (g,h) 220 mJ. With an overall viewing angle of 20^{o} to the surface normal……79

38 SEM images of excimer laser microstructuring a-Si:H film on ITO coated glass substrate with different laser energy. (a,b,c) 160 mJ, (d,e,f) 220 mJ. With an overall viewing angle of 20^{o} to the surface normal……82

39 SEM images of excimer laser processed 400 nm a-Si:H films with low energy as the leading edge in SF_6 with the titled angle of 30^{o}……83

40 SEM images of excimer laser processed 400 nm a-Si:H films with low energy as the leading edge in vacuum with the titled angle of 30^{o}……83

41 EDX measurement of 3μm × 3μm area of bSi film……84

42 EDX measurement on the tip of bSi micro spike……85

43 EDX measurement on the middle of bSi micro spike……85

44 EDX measurement on the bottom of bSi micro spike……85

45 FT-IR spectra of high energy leading and low energy leading laser processed amorphous silicon films……87

46 Reflection of (a) the black silicon (from excimer laser processing 400 nm a-Si:H film on Cu)and (b) Moth-eye structure between wavelength range of 380- 740 nm……88

47 Raman – Spectra for the substrates produced with (a) the high energy as leading edge (HELE, -X direction) scanning method and (b) with the low energy as leading edge (LELE, X direction) method, with annealing fluences in the laser power range of 140-280 mJ/cm^2……89

48 High resolution TEM (HR-TEM) image at 285,000 X magnification of a representative silicon structure on the surface of a bSi substrate. 2D Fourier transforms of the areas 1, 2 and 3, indicative of the crystallinity within these areas, are shown below the main panel……..…….91

49 SEM micrograph of a silicon 'moth-eye' antireflection surface……...…92

50 The cross-hatching regime where laser beam was scanned in both x and y directions, to form a grid pattern on Cu……...….93

51 (a) Image of laser processed 1cm × 1cm black Cu. (b) Top close view of the surface of the Cu target after irradiation with laser fluence of 2.5 J/cm^2……..……94

52 Schematic n-i-p structure a-Si:H nanowire cell……...….98

53 Scanning electron micrographs of high frequency and high energy excimer laser processed 300nm a-Si:H film. (a) overall view at an angle of 20^o to the surface normal, (b) close up view of the micro pillars……100

54 Scanning electron micrographs of low frequency and low energy excimer laser processed 400nm a-Si:H film in N_2. (b) overall view at an angle of 20^o to the surface normal, (b) close up view of the micro pillars……...….101

55 Reflection of the excimer laser processed a-Si:H film (including 1st and 2nd Laser processed) between wavelength 380- 740nm……...…102

56 Transmission in the range of the wavelength of 350 nm to 1000 nm of ultrathin Cr film by DC sputtering…….……..……103

57 Solar cell performance by Newport solar simulator…….....104

58 J_{sc}, J_{max}, P_{max}, V_{max} and V_{oc} marked in the original data for efficiency and fill factor calculation……104

59 Thermopower measurements of a-Si film excimer laser processing on Al and in N_2……..……106

60 Flow chart of cleanroom standard of cleaning glass based substrates…….……...110

61 SEM image of (a) and (b) top view of ELP a-Si thin film on Al substrate, and (c) 45 degree titled view of ELP a-Si as field emitters……..114

62 Schematic of EPD method for deposition of CNTs……....115

63 SEM images of CNTs on ITO coated substrate by EPD growing method…..…..116

64 SEM images of carbon nanotubes grown by CVD method using Ni catalyst (upper image is at 10,000 X and lower one is at 15,000 X on right)……..…119

65 Emission current versus applied field of ELP aSi films……...……..121

66 Emission current versus applied field of CNTs……..122

67 Emission current versus applied field of CNTs and ELP aSi films……123

68 Top and side view of the stainless steel sample holder designed for thermionic emission measurement……125

69 Thermionic emission curves of ELP a-Si films at 300K, 400K, 500K and 600K..126

70 Thermionic emission curves of CNTs at 300K, 400K, 500K and 600K……127

71 Schematic of a novel solar thermal device with black silicon as sun light absorber and ELP a-Si as emitters……131

72 The experimental setup of the real time temperature with Bentham white light source (solar light simulator), thermocouples and thermal meter……...133

73 Real time temperature of the Cu foil with bSi absorber and thermionic emission arrays as well as the temperature on both sides of a pure Cu foil.……..135

74 SEM images of the ELP a-Si:H thermionic emitters.....137

75 Thermopower of the intrinsic and excimer laser irradiated 100 nm amorphous silicon deposited on polished Cu foil……..139

76 The mechanism of the ELP a-Si:H on Cu substrate.....140

77 Thermionic emission curves of ELP a-Si films at 300K, 400K, 500K and 600K……140

78 Two possible p-i-n silicon nanowire PV cells structures.....145

List of Tables

1 Different solar cell technologies and current efficiency……...……..4

2 Different materials of single layer AR coating for thin film solar cells……...….15

3 Various thin film grown by PECVD system.....48

4 KrF excimer laser processing parameters.....52

5 The thermal conductivity of Mo, Cr and Al……..…79

6 Frequently-used targets of DC Sputtering System.....…...110

7 Real time temperature on the bSi film and Thermionic emission array sides with time from 10, 20, 30, 40, 50 and 60 minutes under sun light simulator…….134

8 Real time temperature on the both sides of pure Cu foil without any additional films with time from 10, 20, 30, 40, 50 and 60 minutes under sun light simulator…….134

1 Introduction

1.1 Objectives of this Study

The objectives of this research study are described below:

1. To investigate the field emission and thermionic emission of excimer laser processed amorphous hydrogenated silicon (a-Si:H) films.
2. Development of 'Black Silicon' by processing amorphous hydrogenated silicon with excimer laser. Surface morphology, optical and field emission properties are also studied.
3. Development of silicon nanowire solar device using excimer laser processes, p and n type materials are achieved by excimer laser doping.
4. Design and fabrication of a novel type of solar cell, combines the black silicon sunlight absorber and the thermionic emission effect to create electricity loop.

1.2 Background

Since human beings realized the importance of the living environment and how grievous the 'Green Effect' threat is to themselves from last century industrial expansion, renewable energy has been raised to the top of the list of various topics by many scientists and politicians. Renewable energy means the energy from natural sources. These sources are replenished and also have little impact on environment. Currently (2012), the mainstream of the renewable energy research are a focus on solar energy, wind power, hydropower, marine, biomass, bio-fuel and geothermal energy etc. Among these renewable energy candidates, solar energy is much less site-dependant than any other application [1],

and also, the silicon based solar photovoltaic modules can be maturely manufactured inexpensively, both in commercial and laboratory environments.

Conventional solar modules also known as p-n type photovoltaic (PV) cells, converting light straightforward into electricity by the photovoltaic effect. The solar cell has had a long history since the 19th century. However, the first practical PV cell was developed at the Bell Laboratory by Chapin, Fuller and Pearson in 1954 [2]. Silicon is the second most abundant element in the earth's crust (28.2%, next to Oxygen 46.1% [3]) and silicon- based solar cells occupy roughly 93% of all solar cells in the market. There are two types of silicon solar cells: crystalline and amorphous (a type of thin film silicon solar cell (SC)), and details of these technologies will be discussed in *Chapter 2*.

In this PhD thesis, the focus is on developing a novel type of solar thermal device based on adopting excimer laser crystallized hydrogenated amorphous silicon (a-Si:H) film on Copper (Cu) as the basic cathode substrate to produce a nanocomposite material with 'tunable' electrical and thermal conductivity. The thermionic emission from a-Si:H replaces the conventional p-n junction PV effects to generate electricity, and also, we employ the esoteric black silicon (bSi) film as the sunlight absorber layer in this device. Field emission enhancement is also studied. Meanwhile, a novel type of p-i-n junction a-Si:H nanowire SC is also fabricated by excimer laser crystallized and doping.

1.3 Current Solar Cells Technologies and Market

As mentioned in the previous section and as shown in *figure 1*, 93% of PV cells in the market are silicon material based, amorphous silicon PV cells and crystalline silicon PV cells, which include mono (single) crystalline silicon and multi (poly) crystalline silicon PV cells.

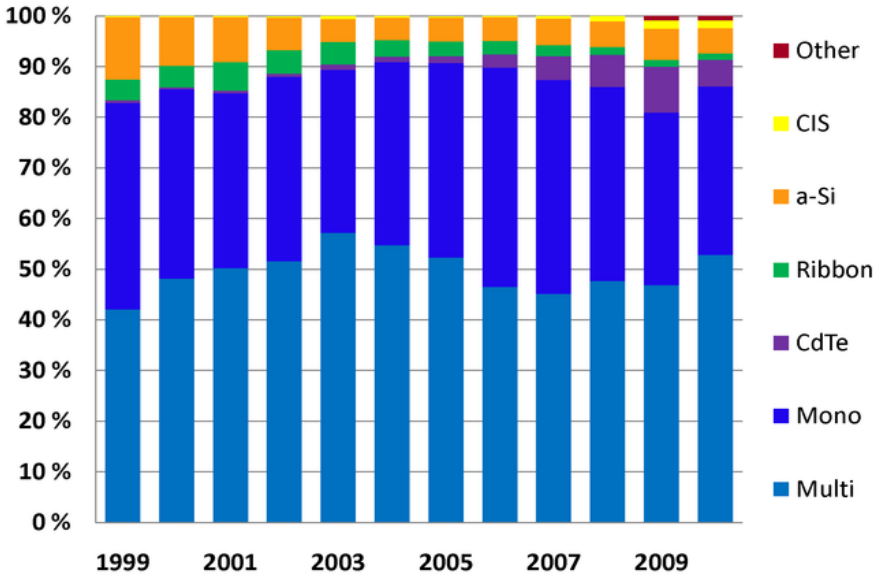

Figure 1: Different photovoltaic technology market share in 2010. Silicon based PV cells (multi- Si, mono- Si and amorphous- Si) share roughly 93% of the solar PV energy market [4].

In thin film solar cell technology, the major subjects are amorphous silicon (s-Si) solar cells, $CuInS_2$ based as well as newly developed $CuIn_xGa_{(1-x)}Se_2$ and Cu_2ZnSnS_4 thin film solar cells, CdTe – based solar cells, Dye- sensitized cells, and Thermal photovoltaic (TPV) devices. Among these technologies, a-Si:H SC shares most attention both in research and commercial environments.

The cost of materials and the size of the devices have always been limiting factors in the development of the PV industry, so reducing the amount of investment capital needs to build a solar farm while achieving large scale is the future trend. Large scale deposition of high quality a-Si:H films with controllable thickness by plasma enhanced chemical vapour deposition (PECVD) and the use of promising excimer laser process technology could just match this trend in the solar industry.

In table 1, a summary of the solar cell technologies and current efficiencies is listed. In this table, single and multi-silicon solar cells are bulk techniques, which will be discussed in Chapter 2.5.3 and 2.5.4. Thin film solar cells, as mentioned, are the most popular research trends to day. The highest efficiency record now is still kept by GaAs tandem device, which can absorb red, green and blue lights efficiently.

Techniques	Efficiency (%)	Reference
Mono-Si	25	UNSW PERL [5]
Poly-Si	20.4	FhG-ISE [6]
Thin film a-Si	10.1	Oerlikon Solar Lab [7]
CuInGaS	20.4	EMPA [8]
CuZnSnSe	11.1	IBM Solution Grown [9]
GaAs	28.8	Alta Device [10]

Table 1: Efficiency table of various PV techniques.

In the solar energy family, the solar thermal device is another important technology that harnesses solar energy for heat which is different from and more efficient than the photovoltaic effect [11]. Recently, scientists developed various models to fabricate novel solar thermal devices which introduced methods such as photon enhanced thermionic emission (PETE) of nano-materials and high performance flat-panel solar thermoelectric devices [12]. Mills reported that 600 megawatts of solar thermal power is up and running worldwide, another 400 megawatts is under construction and there are 14,000 megawatts of 'serious' concentrating solar thermal projects being developed [13] so that the solar thermal technology will play an extreme important role in future renewable energy industries.

In this PhD study, a novel solar thermal device was proposed. Different from conventional thermal energy converter, this device introduced excimer laser processing technique and cost- effective & well developed amorphous silicon materials. In figure 2, the working principle and device structure are presented. This thermal device can be

divided into cathode and anode, and the vacuum gap (100μm to 500μm depend on emitting materials) between them creates the path for the electrons to travel. The cathode side of the thermal device is a copper based component that composed by a sunlight absorber layer - 'black silicon' layer, which is fabricated by excimer laser processing 400 nm amorphous silicon. On the other side of the copper paper, an excimer laser crystallized thin a-Si (100nm) is introduced, which is known as the cathode thermionic emitter. The gate structure is then grown by photolithography to enhance the thermionic emission. On the anode of the device, a copper plate is utilized to collect the electrons emitted from cathode and as well as collecting the waste heat irradiated from cathode for other uses, for example, connect with a water system to warm up the water. Sunlight is collected and trapped in black silicon layer and transfer to the emitters via the thermal conductive copper layer, and with the increase of the cathode temperature, the emitter array is able to emit electrons to the anode, and ideally, this device performs better when the temperature increases. The technical details in this solar thermal unit will be discussed in the following chapters.

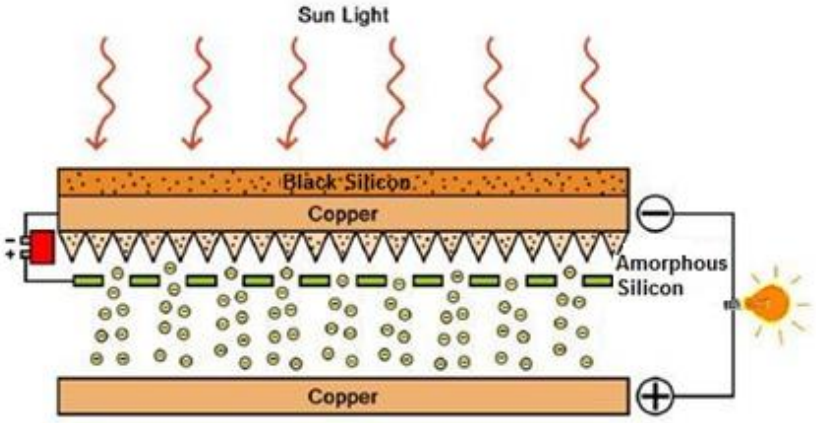

Figure 2: Working principle and device structure of a novel solar thermal device with excimer laser processing technique.

1.4 Thesis Structure

Chapter 1 Introduction – Starts by giving a brief overview of the renewable energy and solar cells, includes PV and solar thermal industries setting the scene for the purpose of this research work and its objectives.

Chapter 2 Literature Review – A review of previous relevant work and research on various electron emission models, excimer laser characterisation technique, thermionic emission effect, PETE device and thermoelectrics, developments of black silicon as well as current thin film solar cell technologies.

Chapter 3 Experimental Techniques – The techniques and equipment involved in the study, including thin film growing methods – DC Sputtering, PECVD and HWCVD, followed by introducing the KrF excimer laser processing system in the University of Dundee. In this chapter, the thin film characterization techniques, such as SEM, TEM, FT-IR, UV-VIS-NIR spectroscopy and Seebeck are also posted. On the final part of this chapter, a home-made field emission and thermionic emission measurement chambers used to examine laser processed a-Si are explained.

Chapter 4 Discussion and Results 1 – Present the experimental results of the black silicon films fabrication, optical & electrical properties and also a comparison with laser processed black copper is discussed as well. In this chapter, excimer laser processed 400nm a-Si films showed a micro-pillar shape surface morphology that can absorb and trap sunlight to be an ideal choice as a sunlight absorber in solar industry.

Chapter 5 Discussion and Results 2 – Present the experimental results of the development of n-i-p single junction nanowire a-Si:H solar cells and the measurements are revealed. With the experience and practices in developing black silicon films as well as excimer laser doping technique, a p- and n-type a-Si:H nanowires are fabricated, and adopted into a nanowire PV cell.

Chapter 6 Discussion and Results 3 – Discussion and analysis of the experiments of the field emission and thermionic emission of the excimer laser processed a-Si:H on various back contacts as well as the carbon nanotubes (CNTs) films grown by chemical vapour deposition and electrophoretic deposition methods.

Chapter 7 Discussion and Results 4 – Present the novel solar thermal device with excimer laser processing technique. In this chapter, the black silicon is examined as the sun lights absorber and the thermionic emission of laser processed a-Si as the emitting layer.

Chapter 8 Summary and Future Work – Summarise the works in this PhD study and discuss some possible further work.

2 Literature Review

In this chapter, reviews of excimer laser crystallisation, field/thermionic emission principle and models, black silicon fabrication and a-Si:H solar cells technologies will be discussed. This chapter starts from a review of crystallisation of a-Si:H based on furnace thermal annealing (FTA), rapid thermal annealing (RTA), laser crystallisation (LC) and laser doping. This review will focus on each method in terms of nucleation, thermodynamics and growth mechanism as found in the literature. The second part will focus on the literatures of various field emission and thermionic emission models discussed currently. In the third part, an introduction to the fabrication process of black silicon (bSi) films by different methods will be discussed. The last part of this chapter presents the current status of a-Si:H based solar cells fabrications and technologies.

2.1 Review on Silicon Based PV Technologies and Models

2.1.1 Crystalline Silicon PV Cells

As the dominant material and technique in commercial PV industry, crystalline silicon has seen huge attention by scientists and researchers. Crystalline silicon PV cells can be divided into Mono- crystalline silicon (mSi) cells and large- grained poly-crystalline silicon (pSi) cells, which share the 41% and 52% of the market on year 2010, respectively (on *figure 1*). Monocrystalline has a dark grey homogeneous appearance (*figure 3 left*) whereas Polycrystalline has a blue sparkly appearance (*figure 3 right*). Classical mSi and pSi PV cells are wafer based bulk devices while mSi cells are more expensive but more efficient than pSi cells.

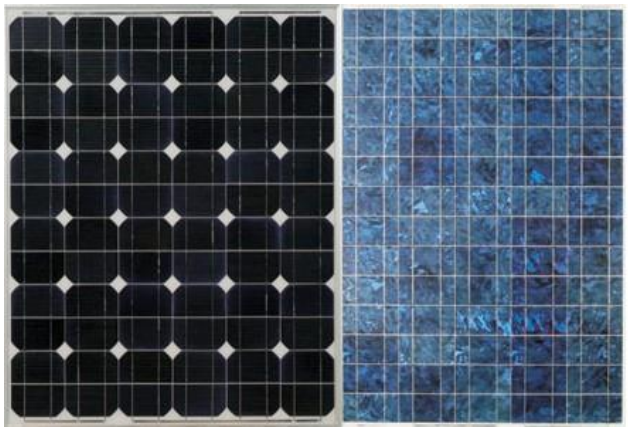

Figure 3: Schematic of standard mSi (left) and pSi (right) solar cells panels.

(***Nova New Energy***)

2.1.1.1 Mono- Crystalline Silicon (mSi) Solar Cells

Mono- Crystalline silicon PV cells, also known as single crystalline PV cells, are the first generation of solar cells when Si was firstly adopted in PV technology in 1955 [14]. The mSi solar cell is normally made using the Czochralski Growth method, which tends to be expensive due to the wafers are cut from cylindrical ingots and the round wafer need to be resized to meet the commercial square shape device requirement. Dopants usually incorporated in silicon solar cell are phosphorus (n) and boron (p). The mSi solar cell with 17% efficiency was demonstrated by Sunpower recently [15].

2.1.1.2 Poly- Crystalline Silicon (pSi) Solar Cells

Compare to mSi PV cells, pSi ones are less expensive because that pSi is made from casting square silicon ingots made by melting the silicon material and pouring it into a die. Other advantages of pSi over mSi are higher throughput and a higher tolerance to poor feedstock quality [16]. However, the efficiency of pSi cell is overall lower than mSi one. A 19.3% efficiency pSi solar device was presented by Mitsubish Electric Honeycomb [17].

2.1.2 Single- Junction Amorphous Silicon Thin Film PV Cells

Different from bulk silicon PV applications, amorphous silicon is in thin film solar cell catalogue due to its thickness and development techniques. As one of the most important material in thin film PV market, a-Si:H PV was intensively studied since it has been the leading thin film PV material since the first investigation by D. Carlson and his colleagues in Radio Corporation of America (RCA) Research Laboratory on 1972 [18]. And later in 1976, D. Carlson and C. Wronski reported an a-Si:H based solar cell with 2.4% conversion efficiency [19]. Actually, in the very first stage, a-Si:H SC was designed as n- i- p structure. However, in a SC device, most light is absorbed around the top, and then the p- i- n formation was adopted to increase the device efficiency because a stronger electric field is generated between p and i layer [20]. There are two configurations of classical p- i- n single junction a-Si:H solar cell: substrate and superstrate- type. The a-Si:H SC combine positive, intrinsic and negative a-Si:H thin layers, a back metal electrode (stainless steel normally used in substrate- type while Mo or Al in superstrate- type) and a front contact layer of transparent conducting oxide (TCO), which is typically indium tin oxide (ITO), as shown in *figure 4*.

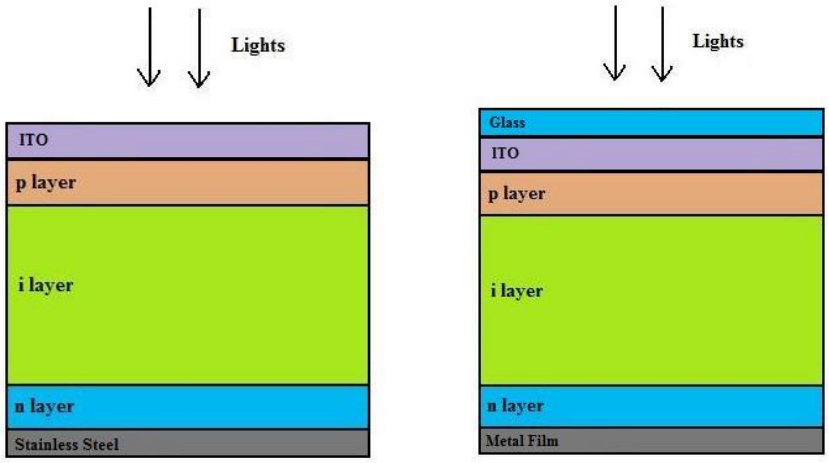

Figure 4: Formation of a substrate- type (a) and superstrate- type (b) a-Si:H solar cell.

The intrinsic a-Si:H has a direct optical band gap of 1.8 eV, which is very effective in absorbing the sun's light. Hence, a single micron thick of a-Si:H film is able to absorb as much as one hundred microns thick of c-Si. This indicates that the cost of a-Si:H SC is greatly reduced. To gain penetration in the solar cell markets, a decrease of the cost is essential. Meanwhile, researchers are also keen on increasing the efficiency by improving the technologies. Till 1982, an efficiency more than 10% a-Si:H SC was developed [21]. Scientists have been trying to achieve higher device efficiency and lower cost of the a-Si:H SC over the last 40 years. Various techniques have been developed to optimize a-Si solar cells, such as nanowire structure to effectively trap the lights [22]. Other approaches, such as plasmonic enhancement by scattering of Au nanoparticles (concentration of 3.7×10^{8} cm^{-2}) into the top ITO layer of the p- i- n a-Si:H SC, has shown a 8.3% increase of energy conversion efficiency and 8.1% increase of short- circuit current density [23]. A-Si:H thin film SC can be deposited onto large, flat substrates of glass or stainless steel and also flexible plastic materials through conventional vacuum evaporation processes with low temperature by mature thin film deposition technologies, such as PECVD. Polyethylene-naphtalate (PEN) and polyethylene- teraphtalate (PET) sheets based thin film a-Si:H SCs are implemented to achieve 8.8% internal efficiency for PEN [24] and 5.8% stable efficiency for PET [25] respectively.

2.1.3 Multi- Junction Amorphous Silicon Thin Film PV Cells

In order to increase the convert efficiency and stability, a number of cells stacked together form multi junction a-Si:H SC. This multi layers structure obviously increases the cell thickness resulting in obtaining more photon absorption and forms a tandem circular.

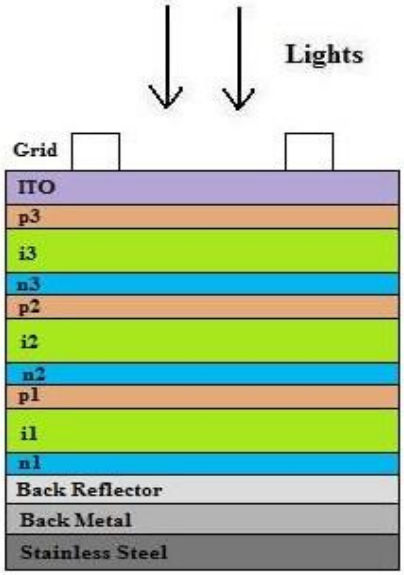

Figure 5: Schematic diagram of a triple- junction cell

A triple- junction structure cell (shown in *figure 5*) has been found to achieve the highest initial cell efficiency of 14.6% with three different bandgaps of i layers, which are 1.8 eV, 1.6eV(10% germanium (Ge) doped), and 1.4eV (40% Ge doped) from top to bottom. This setup can efficiently absorb blue, green and red photons [26]. And in 1994, hydrogenated nanocrystalline silicon (nc-Si:H) was identified as a potential replacement for the a-SiGe:H intrinsic layer for a tandem cell device [27]. The nc-Si:H SC has a higher current density and also reduced the light- induced degradation, although, it requires a thicker intrinsic layer (about 1μm) due to the fact that the nc-Si:H absorption coefficients are much lower than in a-SiGe:H film [28]. Dr. Guha's group used high rate very high frequency (VHF) glow charge method to achieve nc-Si:H i layer and obtained higher

efficiency, 15.4% in 2008 [29]. United Solar who has started to manufacture multi- junction solar applications since 1986 and have a current annual production capacity of 180MW predicts that a-Si:H and nc-Si:H based PV structure is a promising candidate for next generation of silicon thin film solar devices.

2.1.4 Amorphous Silicon Schottky Barrier Solar Cells

The Schottky barrier is also known as the metal/semiconductor (MS) barrier. The Schottky barrier devices are the simplest and potentially most inexpensive with low-temperature processes. The properties of this layer could mainly determine the performance of the device, and also the metal can be replaced by an ITO (transparent, wide band-gap, oxide and highly conducting) option [30].

The first a-Si:H Schottky barrier SC was fabricated by RCA in 1976 with an efficiency of 5.5%, which is more efficient than other types of solar devices [31]. A group in University of Surry employed excimer laser irradiation of the a-Si:H film to form a layer of nc-Si:H film, which is sandwiched by the intrinsic a-Si:H and a heavily phosphorous doped n type lays, and this Schottky barrier SC fabrication results a 40% increase of the external quantum efficiency (EQE) [32].

2.2 Enhancement of Light Absorption in Solar Cells

The enhancement of absorbing light can be achieved by various means, such as modification of the surface of solar cells to make it rough enough to trap the lights, for example, to fabricate nanowire or nanorod arrays which can efficiently reduce the reflection of the sun light, and this can be obtained by using chemical etching and laser technology. Another approach is to add a highly absorbing front layer or a highly reflective

rear layer to capture or bounce the lights to transfer photons into electrons through the p-n junction. Detailed reviews of these techniques are presented below.

2.2.1 Silicon Nanowire Structure Solar Cells

Compared to the half- century history of planar PV technology, Si nanostructure solar cells are still in their infancy. Since the idea was first proposed and simulated by Kayes and colleagues on 2005 [33], this solar cell architecture has been considered as a promising candidate for future PV applications. In their theory, the efficiency of SC is enhanced by the nanostructure for short- carrier- diffusion- lengths. The Si nanowire SC technology has caught lots of attention from scientists and researchers due to its properties which could improve the efficiency with enhancing optical absorption. Recently, a few groups have already investigated the light trapping effect in Si based nanowire-array structure SC [34 - 39].

Silicon nanostructures, especially amorphous silicon nanowires or nanocones structure SCs are attractive owing to their low cost, large scale potential and low temperature deposition of a mature technology on various substrates. Conventionally, researchers develop a-Si:H nanostructure film via reactive ion etching (RIE) process with achieving an increase in cell efficiency [38 - 40]. According to the numerical simulations of Pei et al., including increasing the efficiency, the a-Si:H nanowire SC is also able to minimize the photo- induced degradation effect [41].

However, as far as the author is aware knowledge, utilizing excimer laser process to fabricate and a-Si:H nanostructure SC have not been reported yet.

2.2.2 Anti- Reflection Coating

An Anti-reflection (AR) coating is utilized to reduce the reflectivity of the air-semiconductor interface. This coating results in a dramatic drop of the reflectivity from over 30% to a few percent. The AR coating consist of a thin layer of dielectric material, with a specially chosen thickness so that interference effects in the coating cause the wave reflected from the AR coating top surface to be out of phase with the wave reflected from the semiconductor surfaces. Common AR single layer materials in thin film solar cell applications are described as below:

Single layer of AR material	Thickness (t_f)	Refractive index (n_f)	Applications
SiO or TiO_2 or Ta_2O_5	2272Å	2.0 or 2.2 or 1.98	Silicon solar cells (in IR region)
Ta_2O_5	610Å	1.975	Au/GaAs Schottky barrier solar cells
A mixture of SiO, TiO_2 and SnO_2	693 Å	2.0	Silicon solar cells
Cu_2S	630Å	1.94	Cu_2S/CdS solar cells

Table 2: Different materials of single layer AR coating for thin film solar cells [42].

To further improve the reflectivity, two or more thin AR films could be applied, and actually, the more AR layers, the greater the range of wavelength over which reflectivity can be minimized. However, due to the high cost and the sensitivity to angle of incidence, multi-layers AR coatings are not utilized in solar cells. Double layers of AR coating are used on some high efficiency cells.

2.2.3 Front Textured Surface Anti- Reflection Coatings

As a mainstream method to reduce the net reflection of light and increases the optical depth of the cells mostly in crystalline and polycrystalline materials, textured surface of transparent conducting oxides (TCOs) in solar cells have been adopted. One typical pyramid structure surface could be achieved by anisotropic chemical etc. which acts preferentially along the (111) crystal planes [42]. Payne et al. have reported the surface textured ZnO:Al films which were deposited by reactive hollow cathode sputtering with Zn target for the applications of thin film solar cells. The experimental results showed that ZnO:Al textured films possess significant physically, electrical properties, moreover, in the wavelength region of 450-900nm, 75% transmission is obtained, which is just slightly less than 80% of commercial Asahi U-type AR films [43]. Moth-eye structure is another superior wide wavelength range AR coating design in solar applications. The moth-eye structure was firstly discovered by Bernhard [44] in 1967, and after 6 years, the first artificial moth-eye film was made by Clapham and Hutley [45]. Now, moth- eye structures have been intensive studied to develop as the anti-reflective surface in silicon PV cells fabrication to maximize the photons absorption. Recently, Huang et al. have adopted an Ar/H_2 plasma etching technique in an electron cyclotron resonance reactor to develop tall, dense conical needles arrays in silicon with needle base widths <200 nm. They demonstrated broadband reflectance of <3%, <0.8% and <0.6% for needles arrays of heights 1.6mm, 5.5mm and 16mm, respectively [46]. Likewise, Toyota et al. who have fabricated conical shaped features, which has a structure of a height of 750 nm and a period of 250 nm into fused silica using reactive ion etching (RIE) through a Cr mask defined by electron beam lithography. This results a reflectance of less than 0.5% across the wavelength range of 400–800 nm [47]. Boden and Bagnall demonstrated a technique of rigorous coupled wave analysis (RCWA) to study and simulate the SiN_x/TiO_2 double layer coating of moth- eye arrays, which gave approximately 2% for the laboratory cell and approximately 3% for the encapsulated cell, demonstrating great promise as alternatives to standard ARC schemes for photovoltaic [48].

2.2.4 Back Reflector Enhancement

To harvest the sunlight in solar cells, besides developing top ARC, back reflector layers have also been studied so that they can efficiently reduce the net reflection of light and increases the optical depth of the cell. Metal and metal/dielectric back surface reflectors could yield internal reflectance values more than 90% which conspires to keep the light in the solar cell [49]. The back reflectors typically consist of a thick thermal oxide and evaporated metal layer, and enhance the surface passivation as well as light trapping. In *figure 6*, a diagram of light trapping in an a-Si:H p-i-n solar cell with back reflector is presented. The back reflector can be developed by surface texture technique such as photolithography and reactive-ion etching [50].

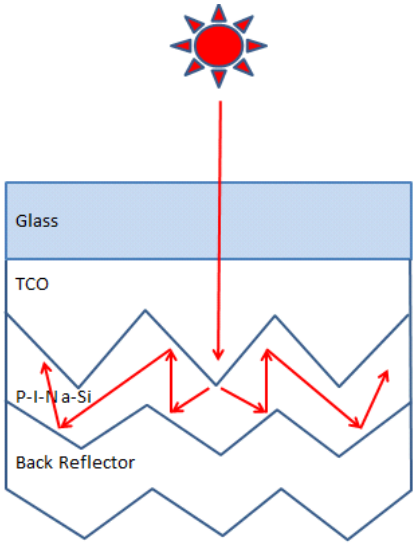

Figure 6: Schematic diagram of light trapping in an a-Si:H p-i-n solar cell.

2.3 Review of Excimer Laser Processing

2.3.1 Excimer Laser Crystallization of a-Si:H

The excimer laser was invented by Basov et al. at the Lebedev Physics Institute in 1970 and firstly employed to treat a-Si:H films in the mid-1980s by Sameshima and Usui's group at the Sony Research Centre [51, 52]. The advantage of excimer laser is that it has very short wavelengths (at ultraviolet and deep ultraviolet) which allows excimer laser focusing on a tiny spot with high transfer of photon energy and high laser beam quality. The excimer laser crystallisation of a-Si:H film proceed via ablation, which has no thermal damage to the surrounding materials. However, the other laser technology, for example, CO_2 laser (wavelength at 10.6 μm) process material by evaporation, or simply boiling off. The basic goal of the research in excimer laser crystallisation is to seek a glass substrate-compatible means of preparing crystalline a-Si:H films known as polycrystalline silicon (pc-Si). The softening point of glass substrates is approximately 600^{o}C, and the excimer laser process allows for the a-Si:H to reach its melting point without damaging the underlying substrates, eg., glass and plastic substrates [53]. This is due to the rapid melt mediated crystallisation, which takes advantage of the spatial and temporal localisation of the heating. The temperature rise by the photon energy is only to a depth of a few nano-meters beneath the film surface [54].

It is reported that according to the low temperature of the substrate during the crystallization process, the untreated a-Si:H still keeps its properties [55]. Pc-Si can switch faster and has higher carrier mobility than a-Si:H material. However, direct ways of growing pc-Si requires temperature of 600^{o}C at least, and with these methods, poorer electrical properties, with relative low mobilities, typically about 5 cm^2/Vs were obtained [56].

Excimer laser processing of a-Si:H on glass substrates has been intensively studied in the past 30 years [53 - 56] not only in the applications of thin-film transistors for large area electronics [57], but ELP has also been introduced to PV industry [58- 60].

2.3.2 Excimer Laser Doping

Doping is distinctly important and indispensable in semiconductor industry as well as in solar cells since it was first developed by J. R. Woodyard [61] and related research was then performed at Bell Laboratory by G. K. Teal and M. Sparks after World War II [62]. As a promising technique in the fabrication and development in microelectronics and semiconductor areas, excimer laser has already been paid a lot of attention due to its fast-processing and suitability to large scale applications.

Excimer laser doping technique, as a newly developed one-step technique, has been widely adapted using various dopant precursors, such as sulphur adsorbate $(NH_4)_2S_x$ doping into GaAs film [63], tertiarybutylarsine (As element) into silicon doping [64], boron doping of silicon [65], using SiH_4 as the dopant into GaAs film [66] and Nitrogen into silicon [67] and silicon nanowires [68] . This technique can achieve n and p type doping as well as has the advantage of simplification of the device fabrication and development processes, and control preciously by simply adjusting the laser fluence & power and laser pulse number [63].

2.4 Review on Electron Field Emission Materials and Models

It is planned in this work to exploit the surface morphology and internal structure of the novel laser processed nanocomposite material and to use field emission enhancement to extract more electrons from the system. Field emission (FE) is also known as cold emission, is the physical process whereby electrons are emitted from the surface of a material, and

tunnel through a barrier caused by a high electric field. Electrons can be emitted from a conductor through field emission, thermionic emission (discussed in chapter 2.3), photo - emission and secondary emission methods.

In this section, a number of different field emission models and various types of field emission cold cathode emitter materials will be reviewed, focusing on the nanocomposite structure appropriate to this work.

2.4.1 Electron Field Emission Models

2.2.2.1 Fowler- Nordheim (FN) Emission Model

Fowler-Nordheim model was named after R. Fowler and L. Nordheim who put forth a theoretical explanation of the field emission electrons into vacuum from metallic surfaces under the influence of an applied strong electric field [69]. As shown in *figure 7*, field emission is described as a result of the tunneling of electrons through the potential barrier that exists at the interface between a cathode- vacuum- anode junction. A high enough applied electric field lowers the barrier and makes the cathode emitted electrons sufficiently penetrable or able to tunnel through, towards the metal anode. So the barrier is relatively thin and low**.**

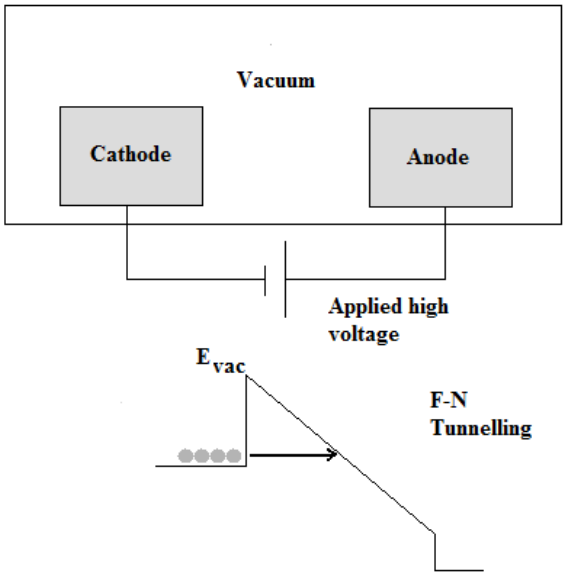

Figure 7: Schematic of Cathode- Vacuum- Anode junction under high applied field.

A few of assumptions have been made to form this model: the free-electron approximation model is applied; no thermally excited electrons and the metal surface is atomically flat and smooth; the model does not take into account space-charge induced effects such as band bending etc. The model being proposed by Fowler and Nordhkeim is expressed below:

$$J = B(\beta E)^2 \, exp(-C\phi^{3/2}/\beta E) \qquad (2.1)$$

where J is the emission current density (A/cm^2), B is the field- independent constant of dimensions= 1.4×10^{-2} (A/V^2), β is the field emission enhancement factor, E is applied electric field (V/m), C is constant=6.8×10^9 and ϕ is the work function (eV).

Here, β is defined as the ratio between the local electric field and the macroscopic applied field.

$$\beta = E_{local}/E_{macro} \qquad (2.2)$$

The F-N model was further developed by Wentzel, Kramers and Brillouin [70]. They described the F-N model by applied voltage, emission current and emission area.

$$I = \frac{AB(\beta V)^2}{\phi} \exp\left(-C\phi^{3/2}/\beta V\right) \quad (2.3)$$

Using the equation (3), the F-N plot could be generated that will the x-axis of *1/E*, and the y-axis of *log(I/E^2)*. From this plot, it can be observed that the β-factor and emission area A can be determined.

$$gradient = -C\phi^{3/2}/\beta V \quad (2.4)$$

$$y_{intercept} = -log\ \phi/AB\beta^2 \quad (2.5)$$

Since this model had been established, it was considered as the standard model by research community working on electron field emission devices. The model was adopted to confirm different plots from different cathode materials to determine whether they with or without significant electron field emission.

2.4.1.2 Negative Electron Affinity (NEA)

Negative electron affinity (NEA) describes the materials whose conduction band energy level (E_C) is greater than the vacuum energy level (E_{VAC}). A positive electron affinity (PEA) and NEA are presented in *figure 8*. Materials having a NEA would emit electrons from conduction band in to vacuum almost effortlessly. However, PEA of materials would emit electrons from conduction band into vacuum by tunneling through the barriers.

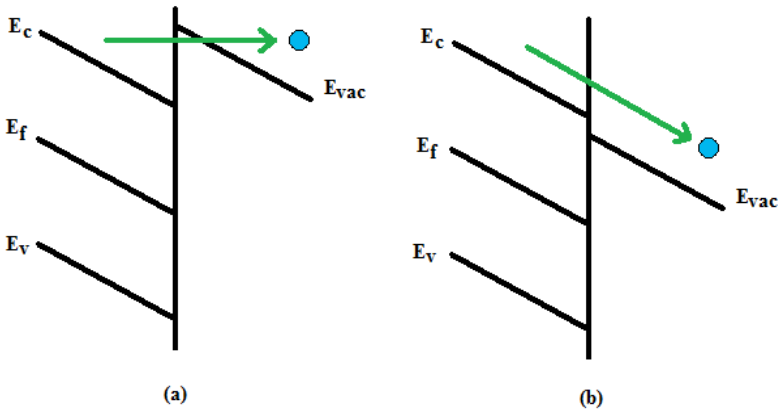

Figure 8: Band diagram of (a) PEA and (b) NEA materials under an applied electric field.

2.4.1.3 Space Charge Induced Band Bending (SCIBB)

The model of hot electrons emission was firstly built by Bayliss and Latham, and explained the concept of electrons tunneling through insulator materials [71]. This concept showed the energy obtained by electrons when they move down the electric field with the lattice, allowing the electrons to obtain greater than that of an equilibrium electron, so it is noted the electron gets 'hot'.

SCIBB was then developed by Amaratunga and Silva with the hot electron model to describe the field emission mechanism in amorphous semiconductors materials [72, 73]. Normally, the conducting electrons lose energy due to electron- photon collision or scattering. However in the case of high fields, a hot electron does not lose all energy through a collision with a phonon and possess sufficient energy to be able to tunnel through the vacuum barrier as 'hot' electrons. The Schottky barrier junction between the metal substrate and thin film supports to fully deplete the thin amorphous semiconductors, such that the electrons that enter the conduction band of the film due to thermionic emission become 'hot'. This results in significant band bending and high localized fields in this region which is much greater than the applied field.

2.4.1.4 Geometric Field Enhancement

Material surface with sharp or rough features could lower the field emission threshold. This enhancement is known as geometric field enhancement which complements the F- N model. The geometric field enhancement is referred to as the enhancement factor β, and can be used in F- N equations. The electric field at the cathode feature can be much greater than the applied macroscopic field, and support in the conduction band of the cathode material can tunnel through the barrier and emit into vacuum. However, a high β factor has also been observed in flat surface of material [74]. These flat thin films should have a geometric field enhancement factor of 1. F- N equation discussed previously could be used for calculating β factor when work function ϕ known. Conversely, ϕ could also be calculated when β is known. If β=1 is used in the F- N equation, it is indicated that for planar surface material, there is no geometric field enhancement, and then an unrealistic work function is obtained. These low ϕ values are termed as the effective work functions achieved from field enhancement.

2.4.1.5 Conductive Filaments Field Enhancement

Field enhancement from conductive filaments shares a similar principle as that for the geometric field enhancement discussed previously. The emitting structure has a high aspect ratio and local electric field lines become crowded, which results in higher electric fields. Poa presented that around the conductive filament, the electric field perpendicular to the filament and also a high electric field parallel to the conductive filament [75].

2.4.2 Field Emission Cold Cathode Materials

2.4.2.1 Spindt tip (metallic) field emitters

Spindt tips sub- micron size conical cold cathode emitter were first developed in 1976 by Spindt and his coworkers [76]. The Spindt tips array is fabricated by thin-film deposition and electron beam microlithography techniques. Each of these cones has its own aperture inside the gate electrode which is well insulated from the bottom electrode by a thin dielectric layer [77]. A typical development process and SEM images of Spindt tips array are presented in *figure 9* [78].

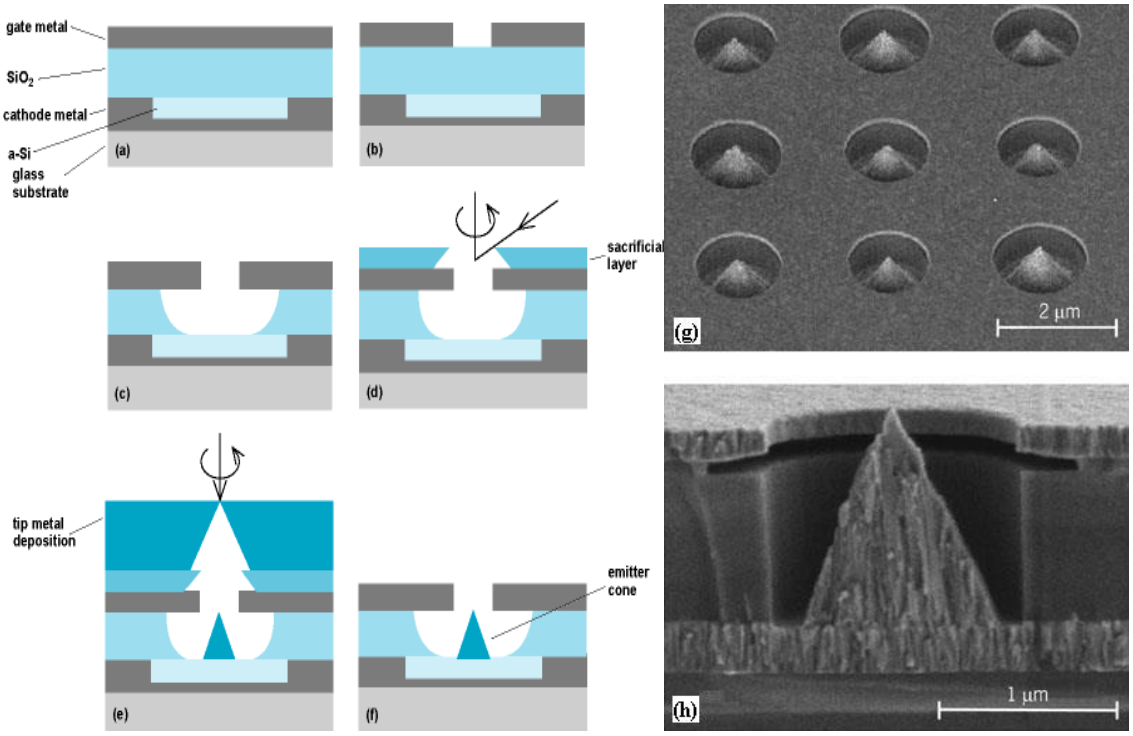

Figure 9: Produce flow of Spindt tips arrays fabrication. (a) Electrode and dielectric layer deposition on glass substrate. (b) Definition of emitter well using photolithography technique. (c) Formation of emitter well. (d) Deposition of sacrificial lift-off layer, typically aluminum, by angle evaporation. Rotation of glass substrate during deposition is indicated by arrow. (e) Tip deposition by electron beam evaporation. Tip materials are usually refractory metals such as molybdenum or niobium. Rotation of substrate is indicated by arrow. (f) Removal of sacrificial and closure layers. (g) SEM of a 3 × 3 array of spindt tips field emission emitters. (h) SEM of cross section of a single gated emitter cone. [78]

2.4.2.2 Carbon Nanotubes (CNTs) emitters

The carbon nanotube (CNTs) were discovered by Iijima in 1991 [79]. CNTs are a form of carbon which exhibit both metallic and semiconductor properties. CNTs are available as single- wall (SWNTs) and multi- wall (MWNTs) nanotubes. *Figure 10* shows the images of SWNTs and MWNTs. MWNTs contains at least two graphitic layers, and the model discovered by Iijima was MWNTs. SWNTs were then developed by Iijima and

Ichihashi of NEC [80] and Bethune et al. of the IBM Almaden Research Center in California [81]. The individual SWNTs tube has a very small diameter, typically ~ 1nm while the inner layer of MWNTs diameters of around 4 nm. CNTs have attracted a lot of attention for field emission applications due the right combination of properties exhibited: nanometer- size diameter, high mechanical strength, high chemical stability, high electrical and thermal conductivity and sputter resistance combined with a preferential geometry for field emission [82 - 84].

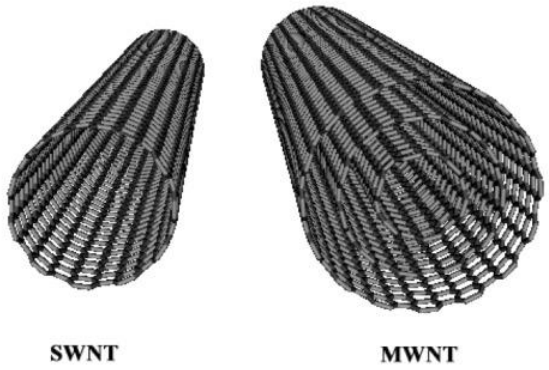

Figure 10: Molecular structures of a single-walled carbon nanotube (SWNT) and of a multi-walled carbon nanotube (MWNT). (from CNRS)

CNTs could be grown by means of arc discharge, laser ablation of graphite and chemical vapor deposition (CVD) such as plasma enhanced chemical vapor deposition (PECVD), hot wire chemical vapor deposition (HWCVD) and microwave plasma chemical vapor deposition (MPCVD) [84]. For CVD technique, a suitable catalyst and different gases mixture can achieve fine quality of CNTs films. A various works have been done to develop CNTs films by CVD method with different source gases: methane (CH_4)/hydrogen (H_2) [83], methane (CH_4)/nitrogen (N_2) [85] and acetylene (C_2H_2)/ammonia (NH_3) [86]. The catalyst material usually is Ni [85], however, other metals Al/Fe/Mo [87] have also been successfully demonstrated. The growth process of CNTs is: the low temperature heated substrate is exposed to a mixture of carbon containing gases in the growth vacuum chamber. The nanotube growth is dominated by surface diffusion of carbon gases onto the

catalyst particle and carbon is transported to the edge of the particle, where the nanotube forms. The metal catalyst particle usually stays at the top of CNT during the growth process. In our research group, Goher has grown CNTs film via PECVD from Titanium (Ti) and Tantalum (Ta) buffer layers on catalyst Nickel coated on silicon substrate with low temperature. From the results, Ta is a good candidate for long, straight and large diameter nanotubes growth while Ti is a good choice for short diameter and uncontaminated nanotube growth [88].

Another rapid, popular and reliable way to deposit CNTs is called Electrophoretic Deposition (EPD) method. In this study, we also produced CNTs by EPD as the field emission emitters. The solution based EPD method of deposition CNTs is to use the electrophoresis effect that when applied a DC electric field across the suspension and the charged particles move towards the electrode of opposite polarity in a proper solvent medium.

The field emission of CNTs was firstly demonstrated on 1995 [80]. Choi's fabricated sealed SWNTs based field emission display by arc discharge method, and for the field emission measurement, the turn- on field was less than 1V/μm and at 3V/μm, the current density J = 90 μA/cm^2 with high brightness, see *figure 11* [89]. The emission current significantly deviated from F-N behavior in the high field region. Smith has investigated the gap between cathode and anode of field emission of CNTs. Various separations of the gap from 1 to 60 μm were applied, the enhancement factor increased according to the drop of the threshold field, however, the threshold field decrease follows asymptotic value dependent on the geometric of the CNT [90]. Cheng and Zhou also calculated the field emission from CNTs film, which gave a threshold field of 2V/μm, for J = 1mA/cm^2 and match the classic F –N behavior. At the same time, they also confirmed the stability and the uniformity of the electron field emission from CNTs. These are very important to the CNTs applications [91]. Samsung demonstrated 4.5 inch color FED from CNTs, and CNTs with enhanced performances will be the promising candidate of commercial in future.

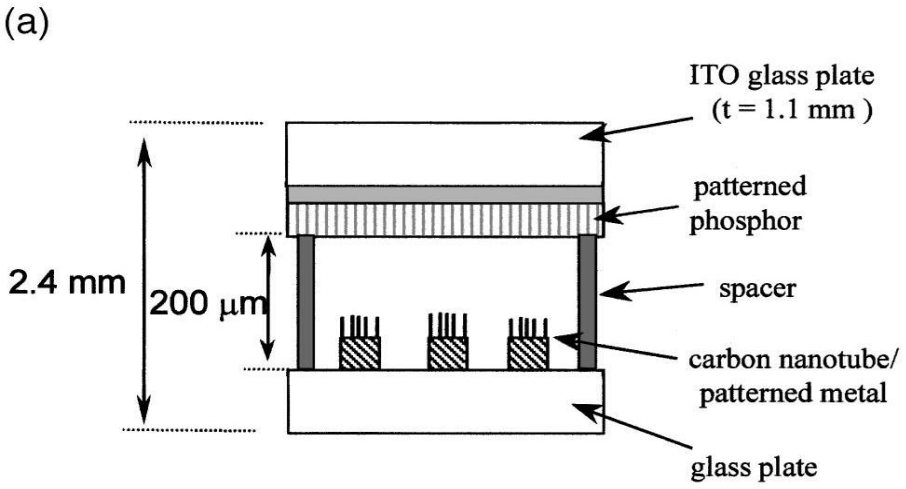
(a)
ITO glass plate
(t = 1.1 mm)
patterned
phosphor
spacer
carbon nanotube/
patterned metal
glass plate
2.4 mm
200 μm

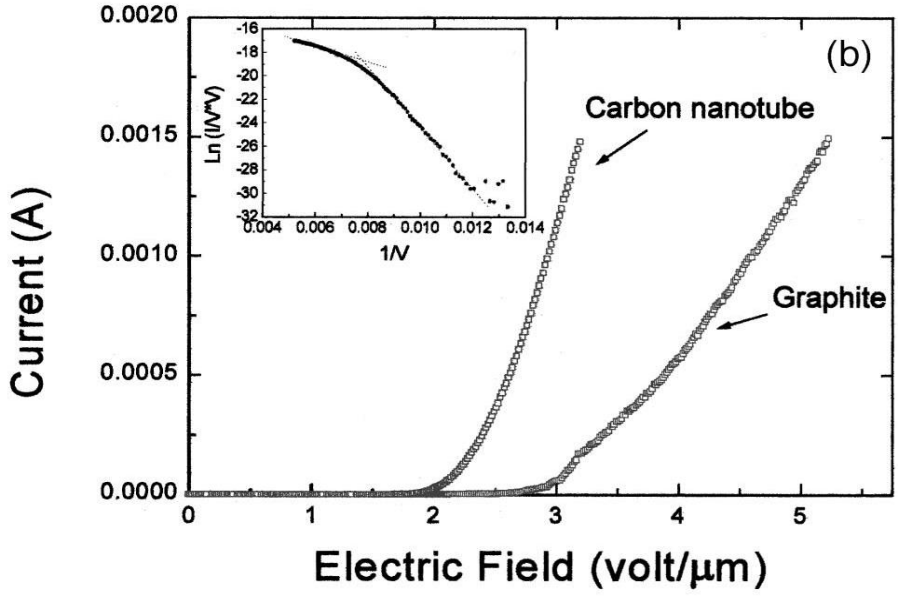
(b)
Carbon nanotube
Graphite
Current (A)
Electric Field (volt/μm)
Ln (I/V²)
1/V

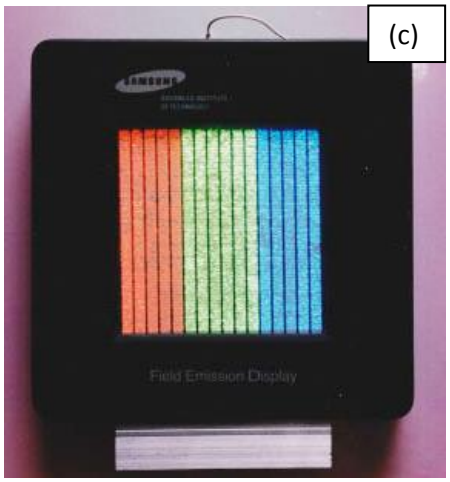

Figure 11: (a) Schematic of fully sealed CNTs FED model. (b) Emission current of CNTs and graphite as a function of electric field. (c) Emitting image of 4.5 inch fully sealed SWNT-FED at color mode with RGB phosphor columns. ([89], from *Samsung*)

2.4.2.3 Silicon based field emitters

As one of the most important semiconductors, silicon has been used as a cold cathode material for electron field emission due to its excellent electronic, crystalline and mechanical properties. Silicon emitters are compatible with existing well- developed fabrication techniques including reactor ion etching (RIE) [92], laser process [93] and plasma- assisted hot filament chemical vapor deposition (HFCVD) [94] and the fact that these techniques are the most widely used for large scale cold cathode emitters. Silicon has a low emission efficiency and poor stability because of its relative high work function.

In order to enhance the emission from silicon field emitters, various coating materials have been adopted to reduce the work function and also prevent from oxidation. Chen utilized Tungsten to coat silicon based field emitters with gate structures, and achieved a turn on voltage of 30V [92]. Han investigated the characteristics of $CoSi_2$ (40nm)/TaN (20nm) bilayer coating Si emitters. The advantages of each material are: high emission current by $CoSi_2$, and low turn-on voltage and long-term stability of TaN. The

field emission measurement results showed a lowered turn-on voltage which confirmed by F-N slope [95]. Bai presented a 3nm thick amorphous carbon (a-C) coated silicon nanotip array to obtain the enhancement of turn-on field and threshold field, and the results showed an enhancement of both, 1.6 and 3V/μm, respectively [94].

Besides Si tips emitters, other types of cathodes Si- based materials have been reported. Wu and his coworkers synthesized CNTs and ZnO nanowires (ZnO NWs) by CVD on rough silicon rods (r-SiRs) which had grown on silicon wafer by a modified electroless metal deposition (EMD) process. Electron field emission was also measured by this group, CNTs on r-SiRs and ZnO NWs on r-SiRs showed a low turn- on field of 2.3 and 2.9 V/μm, respectively [96]. In our department, we reported the poly-Si field emitters of microstructure a-Si:H film by KrF excimer laser on metal based substrate. The field emission results follow the F-N behavior, and a low turn-on electric field of 15 V/μm was measured [97].

2.4.2.4 Diamond and Diamond related materials emitters

Diamond like CNTs, is another allotrope of carbon, has also attracted much attention as the cold cathode field emission emitters because of the negative electron affinity (discussed in Chapter 2.4.1), mechanical and chemical robustness and commercial reasonable cost. The most favorable property of diamond is its NEA surface that is stable in air to allow the surface to emit electrons under low electric field which makes the diamond as a high performance cold cathode material. Zhu reported low field electron emission from commercially available 10-100 nm micropolycrystalline diamond particles developed by explosive synthesis without any metal. The results showed low threshold voltage of 1.5 V/μm for an average current density of 1 $\mu A/cm^2$ which also exhibits uniform, reproducible and stable emission [98]. Kang has reported the vacuum field emission device with gated diamond pyramidal tips, which was fabricated by conventional micro-pattern and etching techniques and their FE results conforms the liner F-N behavior [99]. Different qualities of

FE of the diamond films were also investigated by Fox. In his report, the diamond thin films were produced with different concentrations of CH_4 of 6%, 10% and 12%, and the field emission results indicated that the a higher graphite content diamond film has a lower threshold field and higher emission current. Meanwhile, Fox also pointed that boron- doped diamond thin film exhibited the best field emission performance and were less susceptible to dielectric breakdown [100]. Besides diamond films, field emission property of diamond-like carbon (DLC) thin film has also been studied, Silva has established the space charge induced hot electron model to explain the FE of DLC [101], and May presented the whole process of fabrication of DLC films with different deposition r.f. powers, and the field emission measurements showed the different results upon different r.f. power growing DLC films, however, both follow the F-N curve [102]. Ahmed added different quantities of si into the growing chamber to incorporate DLC. The turn-on fields of Si-DLC in the range 3.61 to 16.19 V/μm when the concentration of Si is 19.31% to 0% [103].

2.5 Review on Electron Thermionic Emission and Thermoelectric Effect

This section will present the principle and model of thermionic emission (TE) and the thermoelectric effect, and also review the current candidates' cathode materials in thermionic emission applications.

2.5.1 Richardson's Law

The effect of discharge of electrons from heated materials is known as the thermionic emission, and this has interested researchers over the world since it was first discovered by Thomas A. Edison in 1883, and then developed by followers after that. This well - known technology has been applied to television picture tube, mass spectrometers, X-ray tubes, SEM and so on. In thermionic emission, the heat supplies some electrons with at least the minimal energy required to overcome the attractive force holding them in the structure of the metal. This minimal energy, called the work function (ϕ), is characteristic of the emitting material and the state. Richardson's law described the thermal electron emission mathematically [104].

$$J_0 = A_0 \lambda_R T^2 exp(-\phi / k_B T) \qquad (2.6)$$

In Eq. (2.6), $J_0[A/cm^2]$ is the emission current density, $A_0\ [A/cm^2K^2]$ is constant, which equals to $4\pi m k_B^2 e/h^3 = 1.20\times10^6\ A/m^2K^2$, λ_R is a material- specific correction factor that is typically 0.5, T is the substrate temperature, k_B is Boltzmann's constant, and $\phi\ [eV]$ is the work function of the material. So, from equation (1), the temperature and the work function of the cathode are the only two factors which can determine the emission current density.

2.5.2 Schottky Emission

The Schottky Emission effect, with a simple modification of Richardson's Law (see equation (2.8)), which reveals that the thermionic emission current is enhanced due to a field, which is applied to its surroundings to lower the surface barrier by an amount $\Delta\phi$ [105].

Hence, $J(F,T) = A_0\lambda_R T^2 exp[-(\phi - \Delta\phi)/k_B T]$ (2.7)

and, $\Delta\phi = (e^3F/4\pi\varepsilon_0)^{1/2}$ (2.8)

where e is electron charge, ε_0 is the electric constant. Eq. (2.8) also indicates that the thermal- field emission current density $J(F, T)$ is highly dependent to applied field F and the temperature T.

2.5.3 Cathode Materials of Thermionic Emission

Carbon based materials have attracted a lot of attention due to their low threshold emission fields as electrons sources. The thermal- field emission of amorphous diamond and nanostructured carbon and diamond materials also been studied. Thermal field emission from nano-tips of amorphous diamond was investigated up to 300^{o}C, which is a relatively low temperature. However, the results showed a great improvement with repeatability of turn-on applied field from 7.6 V/μm on room temperature to 5.5 V/μm on 300℃ [106].

Koeck and his co-workers have employed thermionic emission on various nanostructured carbon and diamond materials, which include nitrogen-doped diamond, phosphorus-doped diamond and sulphur-doped nano-crystalline diamond films. The plasma assisted CVD is utilized to dope N_2 into diamond film on Si wafer. A strong increase of electron emission was observed when the temperature reaches 720^{o}C. From their results,

the measurement between 700 to 950^{o}C shows a significant thermionic emission of the material [107]. Phosphorus doped diamond film low work-function (0.9 eV as the lowest measured work function of any discovered materials) thermionic emission emitters also achieved by plasma assisted CVD but on metallic substrates. The thermionic measurement was measured up to 765^{o}C without an evident drop of the electron emission current, which indicates that the diamond surface is stable on H_2 passivation [108]. Another work of this group is to dope sulphur with nano-crystalline diamond by plasma assisted CVD on Mo substrate, and a distinct increase of emission current with the emitter temperature from 620 ^{o}C to 808^{o}C [109].

As mentioned in Chapter 2.4.2, CNTs have been proved to be a promising material for field emission applications. The thermionic emission of CNTs is also intensively studied. A remarkable thermionic emission result, starting from 2150K to 2900K, is also published by Cox with individual multi-wall carbon nanotubes (MWNTs, ϕ=4.9eV) grown by CVD at low temperature [110]. Thermionic emission is also a method of determining the work function of CVD- grown MWNTs [111]. The emission of single-wall carbon nanotubes (SWNTs) was also studied for temperature from 25 to 1207^{o}C, and the results showed the thermionic emission starts at round 700^{o}C [112].

The exponential increase of the anode current with applied heating power supported the thermionic nature of 3C silicon carbide (3C-SiC) micro-structured filaments, which were investigated by Lee et el. in Stanford University [113].

As discussed above, thermionic emission are occurred in various nanostructured carbon and diamond materials relative in low temperature than that of carbon nanotubes.

2.5.4 Photon Enhanced Thermionic Emission (PETE)

PETE was developed by Dr. Melosh and his co-workers in Stanford University in 2010. This novel process combines photovoltaic and thermionic effects into a single physical process, and has similar vacuum- gap parallel- plate geometry as conventional thermionic energy converters (TEC). As shown in *figure 12*, the photons from the sunlight bombard the PETE cathode, which emits electrons with heat energy to the anode. The PETE anode is united with a thermal engine (steam turbine or stirling engine etc.), which takes advantage of the waste heat to generate electricity to boost a greater total efficiency. This impressive process can simultaneous harness the concentrated light and heat of the sun, and claimed to offer more than double the efficiency of the current PV technologies [114]. The PETE process can also be considered as a combination of a high- temperature PV cells with a thermal cycle. The PETE process does not reach its peak efficiency when operated at 200 ^{o}C due to the cathode emitting GaN material. However, the current silicon based PV cells are not able to compare with PETE device as they become less efficient when the working temperature increases, moreover, they will be inert after the temperature exceeding 100^{o}C [115]. For the current commercial bismuth telluride alloy based thermoelectric device, the working temperature is also limited under 200 ^{o}C that cannot satisfy the high temperature loads. The power output of the PETE converter (P_{PETE}) is presented in equation (2.9), and it is calculated from the difference between the cathode current and the reverse thermionic current from the anode, multiplied by the operating voltage, and the operating voltage is calculated by the difference between the cathode and anode work functions and other extra voltage across the vacuum gap. For the ideal PETE device, to achieve maximum power output, the extra voltage should be zero.

$$P_{PETE} = JV = (J_C - J_A)(\phi_C - \phi_{A+} V_{bias}) \qquad (2.9)$$

where, J_C, J_A, ϕ_C, ϕ_A, and V_{bias} respectively represent the cathode current, the reverse thermionic current from the anode, cathode work function, anode work function and the extra voltage supply. The cathode current J_C can be calculated in equation (2.10) by

determining the steady- state conduction- band population *n* through balancing the rates of photo-excitation, thermionic emission and recombination.

$$J_C = en\langle v_x \rangle e^{-\chi/kTc} \quad (2.10)$$

where, *n* is the electron density in the conduction band, $\langle v_x \rangle$ is average velocity perpendicular to the material surface and χ is electron affinity.

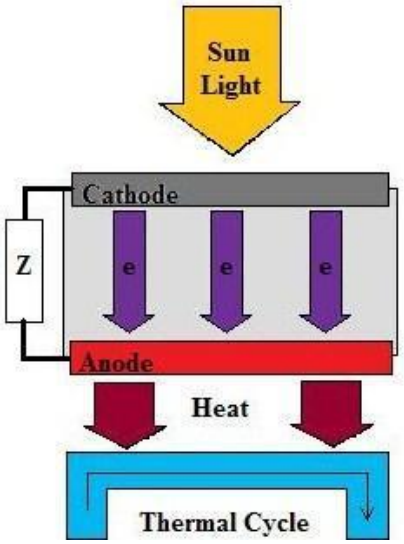

Figure 12: Schematic of a PETE device.

The Alkali metal, Caesium (Cs) - based coating is the most common method to lower the work function and also to reduce a semiconductor anode's or cathode's electron affinity in photocathode research [116, 117]. Identifying the potential cathode material candidates of PETE is the first step that the cathode material should have following properties: low toxicity, large scale availability, bandgaps in the range of 1-2 eV, good thermal stability (>600K), high photoemission efficiency, and low electron affinities. Cs coated Gallium Nitride (GaN), which is an ultraviolet photocathode with high thermal stability, and in a PETE device, the required amount of the semiconductor is quite small. However, GaN is not a suitable material for SC applications due to only around 1% of solar photons have higher energies than the bandgap of GaN (E_g=3.3eV). According to the Eq. 3,

the material of anode should have an as low as possible work function, keep the anode temperature low (minimize the reverse thermionic current J_A) and also have the high-temperature stability. The phosphorous doped diamond, which possesses 0.9eV work function with at least 1000K thermal stability is adopted as the anode in the PETE device [118]. In additional, Cs coated materials are also the possible candidates of the anode, for example, Cs coated Tungsten (ϕ=1.7eV) and Cs coated Titanium (ϕ=1eV).

According to Dr. Melosh's experiments, a tandem PETE/ thermal- engine conversion efficiency as a function of *Eg* and concentration (×100 and ×1000) of the direct + circumsolar AM (air mass) 1.5G solar spectrum are shown in *figure 9*, and it is assumed of an anode temperature of 285°C and a thermal- to- electricity efficiency of 31.5% of the compact linear Fresnel reflection (CLFR) system [119]. It is observed that the best region of cathode bandgap is between 1.1 and 1.7eV and reach the efficiency peak with a bandgap of 1.15eV from the *figure 13*. And the total conversion efficiencies exceeding 53% are possible even at these low anode temperature, constituting a 70% increase over the thermal cycle alone [120].

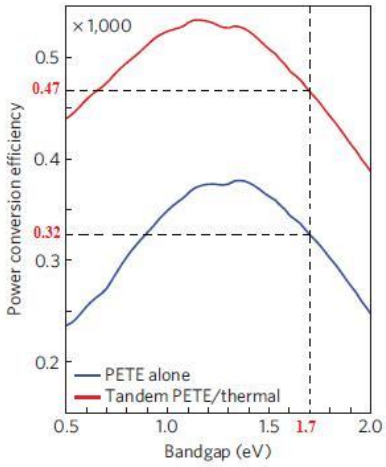

Figure 13: Total PETE/thermal efficiency compared with PETE efficiency as a function of cathode bandgap at ×1000 concentration, assuming a 285°C anode thermally coupled to a 31.5%- efficient thermal engine. [120]

The theoretical and experimental investigations of the PETE concentrate on the fundamental physical processes under various operating conditions, the development of a surface plasmon interface to maximize photon absorption, the study of nanostructured cathode materials to enhance the quantum yield, the engineering of the emitting cathode surface to decrease its work-function and the design of an operating device.

Therefore approaches are being considered to enhance photon absorption. These include surface texturing and the use of nanostructured cathode materials, and the implementation of photonic systems using surface plasmon resonance to absorb and concentrate light into the semiconductor absorber. The working PETE devices are being fabricated and their integration with existing solar thermal designs is being evaluated. Preliminary calculations show that their utilization as topping cycles for thermal engine systems could potentially result in a ~45% increase in overall efficiency.

Different PETE schemes are also being evaluated in this project, such as thermal enhancement of photoelectric emission from a metallic cathode, or the use of low bandgap semiconductor cathodes where thermally excited free electrons in the conduction band would be promoted above the vacuum energy barrier by photon absorption.

PETE performs ambitious at high temperatures, which normal PV cells could not reach. More inspiring, the PETE device could be a candidate in solar concentrators such as parabolic dishes, which can get as hot as 1000K.

2.5.5 Thermoelectric Effect and Measurements

The first of the thermoelectric effects was discovered in 1821 by T. J. Seebeck, and this effect was also named Seebeck effect. The Seebeck effect explains that an electromotive force can be generated by heating the junction between two different electrical conductors, and one classical example is the thermocouple, which is a common temperature measurement technique in vacuum technology. The conventional type K thermocouple makes a connection between two different metals (Chromel and Alumel).

The output voltage reading can be directly observed and converted into temperature via the chart. Thermoelectric materials convert heat into electric current, and vice versa [121].

The thermoelectric efficiency is described in terms of the thermoelectric 'figure of merit', *ZT*, which can help to understand and investigate thermoelectric material. *ZT* is a function of Seebeck coefficient (*S*), thermo conductivity (*k*), electrical conductivity (σ) and absolute temperature (*T*), which is shown in equation (1) below.

$$\boldsymbol{ZT} = S^2\sigma T/k \qquad (2.11)$$

From the above equation, the high ZT material should have high Seebeck coefficient and the electrical and thermal conductivity should be as low as possible. As shown in *figure 14* [122] parameters of Seebeck coefficient, electrical conductivity, thermal conductivity and ZT are respect to the free carrier concentration. It is not easy to get high S and high k at the meaning time that limits the efficiency of the materials and the thermoelectric convert devices. The most common commercial bulk Bismuth Telluride (Bi_2Te_3) based p and n type material can nearly reach ZT = 1 by introducing precise doping techniques. The undergoing researches on nanostructured alloy materials, such as nanowires, nanocomposites, quantum dots, and quantum wells etc., which have been reported to possess over 2 high ZT values [123- 127].

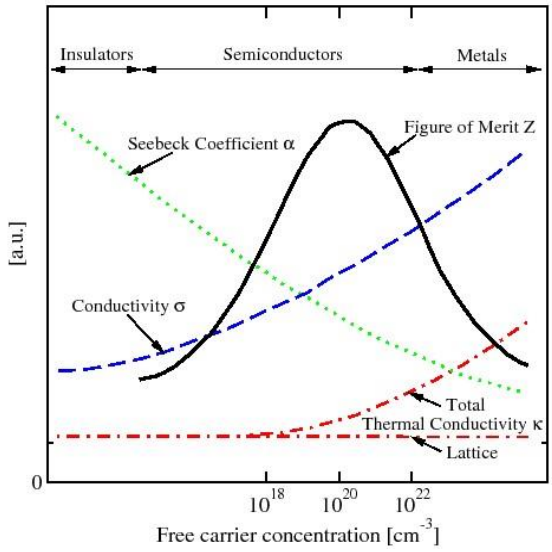

Figure 14: Seebeck coefficient, electrical conductivity, thermal conductivity, and figure of merit (ZT) with respect to free carrier concentration [122].

Seebeck coefficient is measured by the magnitude of an induced thermoelectric voltage in response to a temperature difference between the ends of the target material [128]. The thermopower has units of volts per kelvin (*V/K*) although it is more often given in microvolts per kelvin ($\mu V/K$).

The Seebeck coefficient measurement method in this study, a self-designed vacuum chamber with soldering heaters, K type thermocouples, and liquid N_2 cooling system is presented in Chapter 3.3.

The electrical resistivity ρ is measured by 4- pin probe portable resistance meter, and the electrical conductivity is then calculated by equation (2.12).

$$\sigma = 1/\rho \qquad (2.12)$$

Principally, thermal conductivity is normally calculated through thermal diffusivity α, heat capacity Cp and material density d, shown in the equation (2.13).

$$k = \alpha \cdot Cp \cdot d \qquad (2.13)$$

2.6 Review on Fabrication of Black Silicon Films

The black silicon (bSi) is a novel material which was first discovered by a research group headed by Professor Eric Mazur in Harvard University. In one solar cell device, bSi seems to be a good candidate to replace the high cost anti- reflection coating materials because the bSi is significant in low cost and the rough surface allows broadband to lower reflection. The process of Mazur's experiment is to use regeneratively amplified Ti:sapphire laser to irradiate n type (arsenic doped) silicon wafer with a strain of 800 nm, 100 fs laser pulses in the presence of backfilled SF_6 or Cl_2 gas with the chamber pressure of 500 Torr. The spatial laser profile is nearly Gaussian, with a 200- μm beam waist at the sample and a fixed fluence of 10 kJ/m^2 at the center of the spatial profile. The 40- μm tall with cross section of about 6×10 μm^2 conical spikes are then formed, capped by a 1.5- μm ball [129, 130]. In addition to laser irradiation, the black silicon can also be achieved by other methods. J. S. Yoo et al. from Sungkyunkwan University reported the possibility of obtaining the uniform bSi surface on both n- type c-Si and mc-Si wafers with a multi-electrode embodiment radio frequency (RF) mutli-hollow cathode discharge system with applying the RF power (13.56 KHZ frequency) of about 20W per one hollow cathode glow, SF_6/O_2 ratio at 2.5 with the pressure of 50 mTorr for 20mins [131]. Recently, Y. Xia and his colleagues in Chinese Academy of Sciences presented another way to fabricate black silicon from the boron doped p type single c-Si wafer. They have successful produced very low reflectance black silicon by plasma immersion ion implantation (PIII) technique with a 900W radio frequency power supplied chamber of SF_6 and O_2 mixture gas (20 and 90 sccm respectively), and the working pressure is 0.86Pa with 10 mins treatment [132]. Another popular way to develop bSi is chemical etching techniques. Branz used 5nm colloidal gold in a solution of 0.4mm $HAuCl_4$, adding an equal quantity of HF: H_2O_2:H_2O (1:5:2) to etch the Boron- doped p type Czochralski silicon wafer for 2 mins to develop bSi [133]. A similar approach is also achieved by Koynov with adopting the ratio 1:5:10 of HF: H_2O_2:H_2O solution at room temperature for 2 minutes to wet chemical etch silicon wafer with a 0.7-1 nm thick Au layer on top [134]. The Advanced Material Group at the University of Dundee has presented a rapid and novel technique, excimer laser processing,

to develop large scale ‘black silicon’ on silicon substrate [135] and also the first to fabricate black silicon on metal coated glass substrates [136]. Various ways to develop the remarkable bSi layer by just couples of simple steps make it popular that may be used to replace the surface textured layer as the sunlight absorber in a PV cell device to harvest the thermal absorbing. In *figure 15*, the principle of the lights trapping in bSi film is demonstrated. The lights hit the sides of the bSi and reflect with some random angles and then reflect several times between two neighbouring silicon micro spikes, and considering the height of the micro pillars (typically around 2 μm) and the separation of them is normally around couples of hundred nanometres, the lights will stay in the bSi features for a longer time, which let bSi be a promising light absorbing layer.

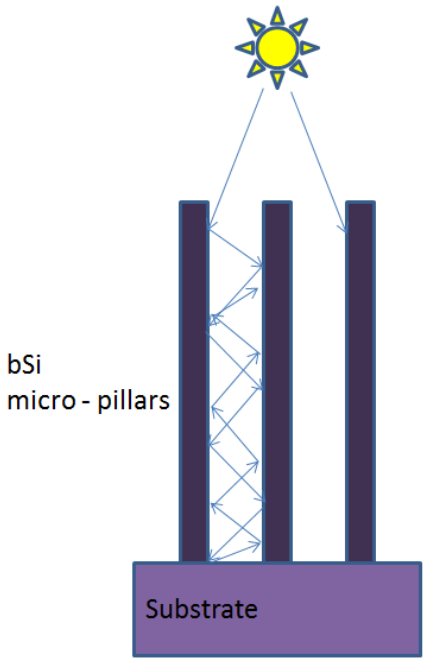

Figure 15: Schematic of light trapping in black silicon micro spikes.

2.7 Summary

In this chapter of reviewing relevant literature, we started from discussing excimer laser technology, followed by field and thermionic emission models and some promising cathode materials. We also reviewed the fabrication methods of a black silicon layer. Finally, an introduction to a-Si:H based thin film solar cells and light absorption enhancements by different technologies was presented.

The excimer laser irradiation of a-Si:H films on glass substrates has a history of more than 30 years in TFTs for large size electronic applications and recently adopted in PV cells to fabricate high quality and efficiency solar devices.

The black silicon is an innovative application in various ways, and one of them is to perform as the sunlight absorber to enhance light trapping. The various fabrication methods make black silicon to be used in large scale application with low costs. In our study, excimer laser processes are utilized to develop black silicon array on copper substrate.

Five models- Fowler-Nordheim (F-N) emission, negative electron affinity (NEA), space charge induced band bending (SCIBB), geometric field enhancement and conductive filaments enhancement of field emission models with promising cathode materials of spindt tips, CNTs, silicon based emitter and diamond & diamond-related emitters were introduced, which are the basic of this work. A further study of thermionic emission models of Richard's law, Schottky emission principle and PETE model and materials of carbon-based, amorphous diamond and CNTs are essential to understand the work of the prototype of the thermal enhanced photon PV device (will be discussed in Chapter 7).

A review of a-Si single, multi and Schottky Barrier solar cells is studied to understand the principle of a-Si:H solar devices, furthermore, a few of enhancement methods such as nanowire or nanorod structure, surface texture treatment, anti-reflection front coating and rear reflector were reviewed.

This chapter of literature review acts as the foundation of the whole thesis, and all the research works are relative and developed from here. In the purposed novel solar

thermal device shown in figure 2, the key factors are, the first, light absorber, which is required to maximized absorb and trap the sun lights and then transfer the heats to the emitters via the copper foil with a minimized loss. The second key point in the research is the emitting materials. As reviewed in this chapter, CNTs and carbon based material, such as diamond film are great candidates for field emission. However, CNTs has no signs of thermionic emission unless applying more than 2000K, and diamond materials are relative expansive as well as time consuming in deposition. So in this research, a fabrication of large scale, cost effective and rapid growing sunlight absorber – black silicon and excimer laser crystallized amorphous silicon emitting materials will be introduced and studied in next two chapters.

3 Experimental Techniques

3.1 Thin Film Deposition Techniques

In this section, three important thin film production techniques in silicon technology will be discussed. DC Sputtering of the metallic backplane, plasma enhanced chemical vapour deposition (PECVD) and hot wire chemical vapour deposition (HWCVD) of a-Si:H films.

3.1.1 DC Sputtering of Base Metal Plates

The DC sputtering is a physical vapour deposition (PVD) method that comprises two electrodes in a stainless steel vacuum chamber with an Argon inlet. The rotatable substrate holder (for uniform coating) acts as the anode in the chamber, and the cathode holds the sputter target as well as a high voltage supply. The plasma is excited between electrodes during the Argon gas at a pressure of 1 Pa by the high DC voltage. The positive Ar ions which have high enough energy are accelerated to bombard the sputtering target on the cathode, and to free the atoms or molecules from the target in all directions. The surface of the rotatable substrate on anode, meanwhile, coated a desired layer of the target material. *Figure 15* is a schematic of the DC sputtering chamber.

In the experiments, for the measurement of electron field emission, thermionic emission and thermopower of the excimer laser treated thin amorphous silicon film, the DC sputtering is used to deposit different metal contacts such as molybdenum (Mo), chromium (Cr), aluminium (Al) and copper (Cu) by different thickness. These sputtering targets are all high purity and mounted and fixed by a stainless steel ring in the bottom centre of the chamber as shown in *figure 16.*

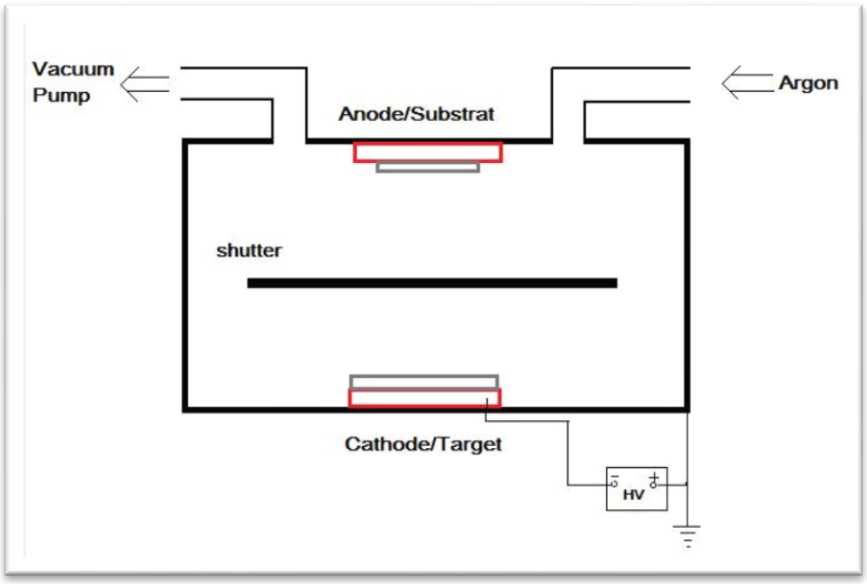

Figure 16: Cross-section view of DC Sputtering chamber.

3.1.2 Plasma Enhanced Chemical Vapour Deposition (PECVD) Technique

Plasma enhanced chemical vapour deposition (PECVD) is a type of chemical vapour deposition (CVD) process which enhances the reactions and allows relatively low temperature deposition and large scale deposition. Pure a-Si:H or doped a-Si:H thin films or silicon nitride or silicon dioxide can be deposited by PECVD for many purposes, such as TFT arrays in active matrix liquid crystal displays (AMLCDs), p-i-n junction amorphous solar cells, sensors and other opto- electronics applications [137]. This process is also known as the 'glow discharge' process. To develop a-Si:H films by PECVD, radio frequency (r.f.) power is introduced at 13.56MHz and at a gas pressure of 0.1-1 Torr between two parallel electrodes. A hydride of silicon called silane (SiH_4) and diluting gas hydrogen (H_2) are introduced into the reactor and decomposed to a plasma, which is confined between two electrodes, excited by the uniformly distributed r.f. power resulting in SiH_3, SiH_2, SiH, Si, H, H_2, electrons-photons and other fragments forming a weak

plasma. The system is illustrated in *figure 17*. With this process, a-Si:H films can be deposited to various thicknesses depending on the operation time on the heated substrates (normally 250^{o}C). To receive optimum quality of a-Si:H films, many parameters can be altered, such as gas flow rate, pressure, r.f. power and substrate temperature.

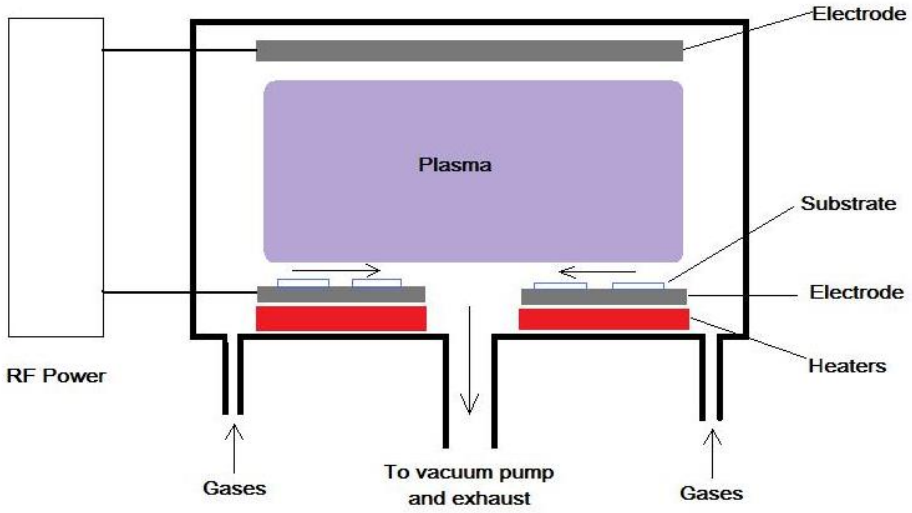

Figure 17: Cross view of PECVD chamber.

PECVD system can also produce n and p type a-Si films with introducing dopant gases. It was firstly reported by Spears and LeComber in the University of Dundee to adapt Diborane (BH_3) diluted SiH_4 to achieve n-type a-Si:H thin film with using Phosphine (PH_3) diluted SiH_4 to produce p-type [138]. Table 3 lists various thin films deposited by PECVD technique.

Thin Films	Precursor Gasses	Dopant Gases
Silicon Dioxide (SiO_2)	Dichlorosilane or Silane	Oxygen
Silicon Dioxide (SiO_2)	Tetraethoxysilane (TEOS)	Oxygen or Oxygen-Argon
Silicon Nitride (SiN)	Silane	Ammonia or Nitrogen
p-type a-Si:H	Silane	Phosphine
n-type a-Si:H	Silane	Diborane

Table 3: Various thin films grown by PECVD system.

To achieve high quality of a-Si:H film, the PECVD system at the University of Dundee also has an Argon inlet with electronic mass flow controllers. Before depositing a-Si:H, an Ar plasma is employed to clean the surface of the substrate. A pumping system comprises rotary pump and turbo pump with a pressure meter attached to the chamber, which allows the chamber to achieve a base pressure of 1×10^{-5} mbar. To vary the content of bonded hydrogen of the a-Si:H, a mix gas of H_2 and SiH_4 is introduced to obtain a process pressure of 150 mTorr.

3.1.3 Hot Wire Chemical Vapour Deposition (HWCVD) Technique

The hot wire chemical vapour deposition (HWCVD, *figure 18*) is commonly used to prepare a-Si:H and nano or microcrystalline silicon thin films. HWCVD offers many advantages, such as delivering high deposition rates (typically 10-50 Å/s) than the PECVD process. In addition, in the deposition process, the HWCVD process has zero ion damage [139]. The HWCVD process can also produce films at low substrate temperature with high quality on cheap or flexible base substrates [140]. The principle of HWCVD process is chemically decomposing SiH_4 into atomic radicals at the surface of a heated tungsten or tantalum filament (1500-1700^{o}C). The surface of the base substrate (keeps at 200-220^{o}C) then forms a layer of desired thin film due to the reactive species transportation. Additionally, a-Si:H film deposited by the HWCVD process can retard the degradation when exposed to light due to its owns low hydrogen contents reducing the Staebler-Wronski effect [141]. The stability of the thin film is important to commercial and laboratories use.

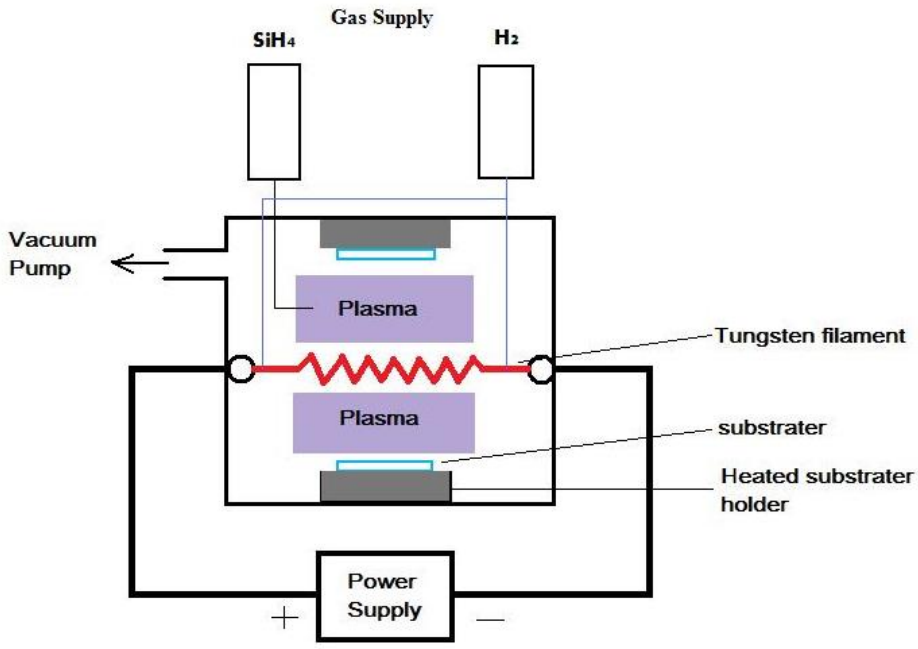

Figure 18: Cross view of HWCVD chamber.

3.2 Excimer Laser Processing Technique

In this study, the a-Si:H films were irradiated by an LPX*pro*210(F) KrF excimer laser at a wavelength of 248 nm and 20 ns pulse duration. *Figure 19* illustrates the layout of the laser optical system.

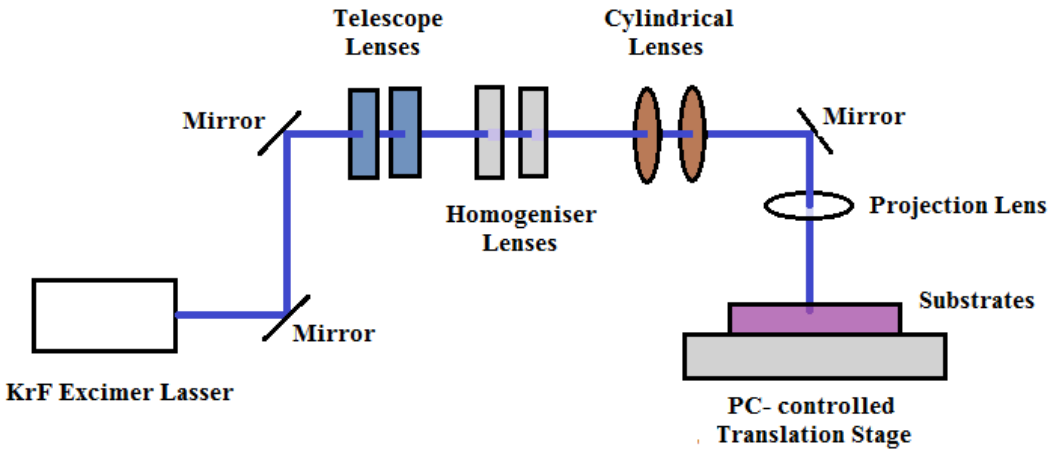

Figure 19: Schematic Diagram of KrF Excimer Laser System Layout.

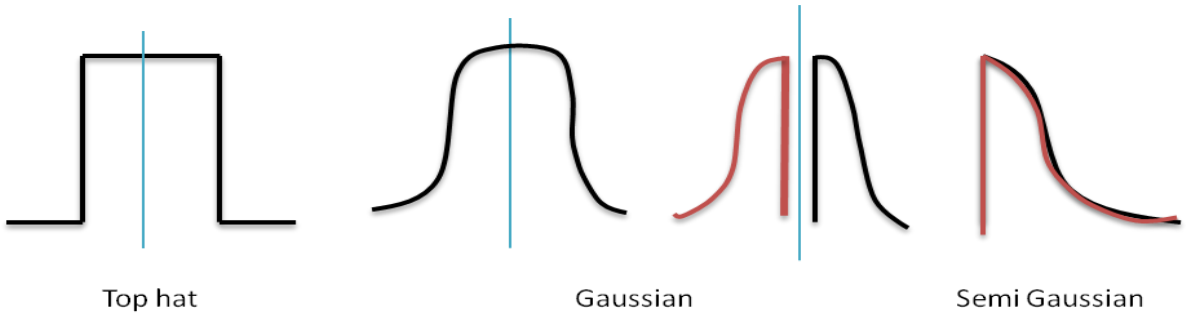

Figure 20: Beam profile of excimer laser.

To obtain the desired energy and beam profile, a dedicated optical system is adopted. The laser beam that is produced from the main laser is controlled by an electronic shutter connected to the PC. The beam then is firstly reflected by the 1st mirror and passes through an attenuator which reduces the initial power. The 2nd mirror reflects the beam to the main optical setup which consists of a series of lenses for directing and shaping the laser beam. The telescope lenses expand the beam so that it can fill the homogeniser lenses, which break the input beam into many tiny beams towards the cylindrical lenses. The cylindrical lenses modify the beam into a pre-set shape by software, and then the beam is reflected by the 3rd mirror to pass through the projection lens and reach the substrate stage. Here, the projection lens focuses the beam at a specific distance so that a range of beam sizes can be selected for the substrate treatment. In *figure 20*, the beam of the excimer laser is illustrated and in this study, the semi Gaussian profile is utilized in the excimer laser processing. The semi Gaussian profile was modified through the Gaussian profile as shown in *figure 20* so that to create a sharp increasing of the laser energy and drops gradually when scanning from left to right while increasing the laser energy gradually and drops dramatically when scanning the substrates from right to left, as called high energy as the leading edge scanning and low energy as the leading edge scanning, respectively.

Table 4 circulates the parameters of the excimer laser processing in fabricating the black silicon films as well as field and thermionic emitters.

Applications	Black Silicon	Field/Thermionic Emitters
Scanning Profiles	Low power as scanning leading edge	High power as scanning leading edge
Scanning Speed	0.5 mm/second	2 mm/second
Beam Energy	160-220 mJ/cm^2	70-110 mJ mJ/cm^2
Laser Pulse on unit area	400, 800	100, 200
Laser Beam Pattern	4 mm × 8 mm	4 mm × 8 mm

Table 4: KrF (248nm) excimer laser processing parameters.

3.3 Thin Film Characterization Techniques

3.3.1 Scanning Electron Microscopy (SEM) & Energy- Dispersive X- Ray Spectroscopy (EDX)

A SEM is a powerful imaging instrument to observe and study the surface morphology of materials such as the laser processed a-Si:H films and CNTs. In an SEM system, an electron gun provides high energy electron beams which are micro and nano on the surface of the substrate through a series of lenses. Scan coils establish the images by letting beam scan across, and the secondary electrons emitted from the surface of the substrate are collected by the detector which build up an image on the display. The whole process takes place in a vacuum chamber and *figure 21* shows a typical SEM system.

SEM offers a few benefits including large depth of field, high resolution and high magnification. It is also common to coat a thin gold (7-10nm, Au) film on the top of the substrate to reduce the accumulation of charge on the objective to obtain clear SEM images.

In our study, a JEOL JSM- 7400F Field Emission SEM (FESEM) was used to analysis the surface morphology of the laser processed a-Si:H film emitters.

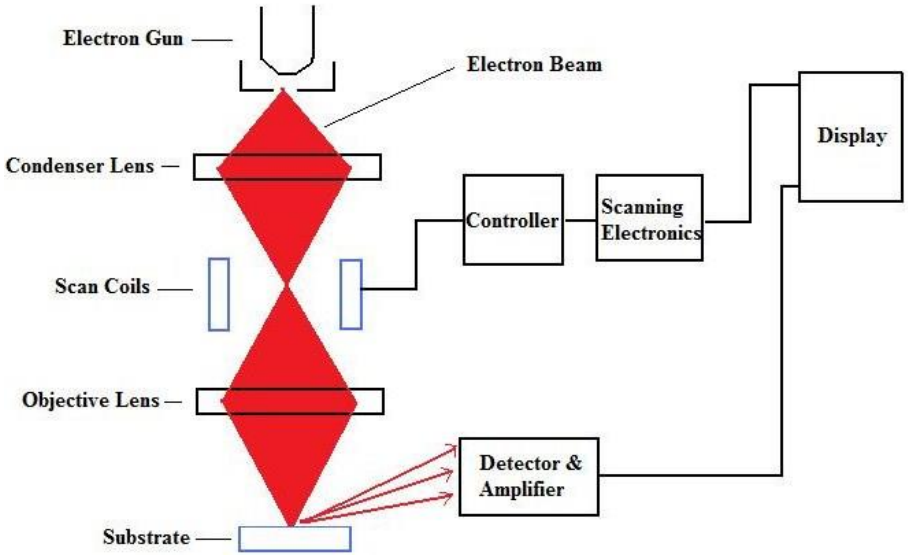

Figure 21: Schematic representation of a SEM system.

The EDX instrument normally equiped together with the SEM system. The EDX system is a powerful analytical technique used for obtaining a localized elemental or composition analysis of a solid sample by bombarding with a focused beam of electrons emitting from the X-ray spectrum. By detecting the atomic energy level, the compositional result can be directly observed via the PC [142].

3.3.2 Transmission Electron Microscopy (TEM)

TEM is a valuable image processing tool in both bioscience and materials research. A TEM system has the same basic principles as the light microscope. However, TEM uses electrons as the light source. The much lower de Broglie wavelength of the electrons allows

a significantly higher resolution TEM images, a thousand times better than with a light microscope. The electrons are emitted from the top electron source, and travel through vacuum in the column of the microscope. The TEM uses electromagnetic lenses instead of conventional glass lenses focusing the lights in the light microscope, to focus the electrons into a very thin beam. The electron beam then travels through the loaded substrates. At the bottom of the microscope, the unscattered electrons hit a fluorescent screen, which gives rise to a "shadow image" of the loaded substrate with its different parts displayed in varied darkness according to their density. So, with TEM, atomic levels of materials could be observed and studied directly. In our experiments, the high resolution TEM (HRTEM) was used to observe the nano-components of our excimer laser crystallized a-Si:H films and black silicon spikes. The schematic of a TEM system is shown in *figure 22*.

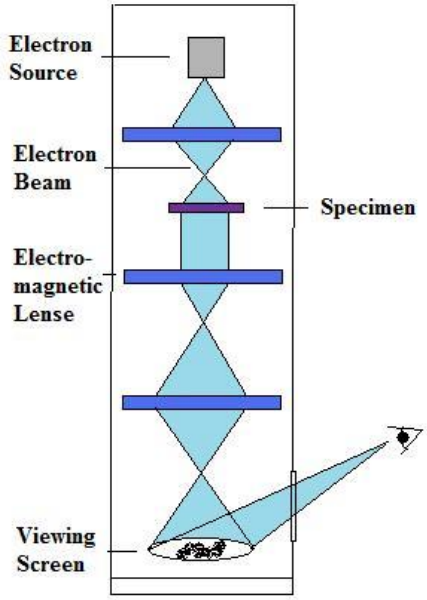

Figure 22: Schematic of a TEM system.

In this study, the TEM samples were prepared by firstly polishing the substrate by the machanical dimpler, which can reach 1 μm thich of the sample, and following by etching the film by using ion beam that can obtain a 100 nm thick film, which is a standard thickenss of the TEM sample.

The current popluar method of preparing TEM speicmen is known as using ‘lift-out’ technique and focused ion beam (FIB) milling method that uses the focused ion beam to etch two gaps with the sepeartion within 100 nm. And then using the lift out technique to adapt the film between two ion etched gap can be used in TEM measurements.

3.3.3 Fourier Transform Infra- Red Spectroscopy (FT-IR)

FTIR is a powerful instrument which can be used to identify unknown materials, assess the quality and measure the components of a mixture specimen. In a FTIR system, the Infrared radiations cross through a substrate. Some IR radiation is absorbed by the substrate and rest of it transmits through the substrate, the working principle is shown on *figure 23*. This resulting spectrum represents the molecular transmission and absorption, also building the molecular fingerprint of the specimen.

In our research, Matton 7000 Galaxy FT-IR system is adopted to measure the content of bonded H and O in laser processed thin silicon films. All films to be measured by FTIR system were deposited on n type silicon wafer. Glass substrates and metal substrates should not be used here since they are not transparent to the infrared radiation. N_2 flushed the whole chamber, necessary to remove all the water wafers inside the chamber to obtain more precise results. A background spectra was taken with a bare silicon wafer in order to obtain the true spectra of the a-Si:H films only by subtraction.

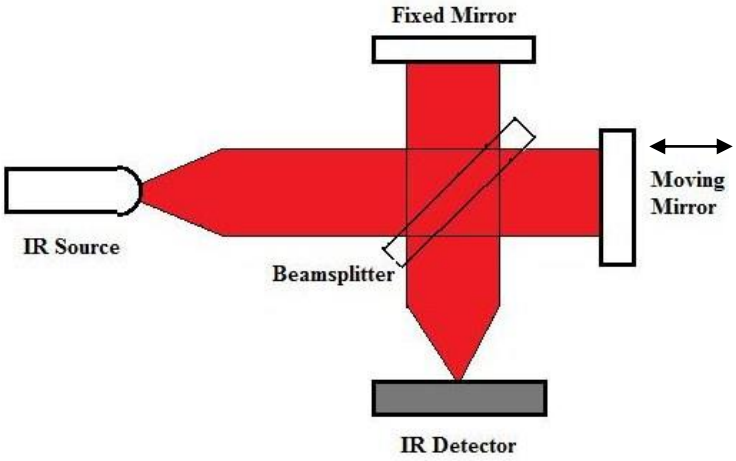

Figure 23: Working principle of a FT-IR system

3.3.4 UV-VIS-NIR Spectroscopy

The UV-VIS-NIR spectroscopy just as its name implies that can measure the optical transmission and absorption in the wavelength range of UV (100 – 400 nm), visible spectrum (380 – 750 nm) and near Infrared (750 - 1400 nm) of a solid or liquid objective. *Figure 24* shows a schematic of a typical UV-VIS-NIR Spectroscopy.

This technique is widely used in PV research on analysis of lights reflection by various bulk materials or thin films.

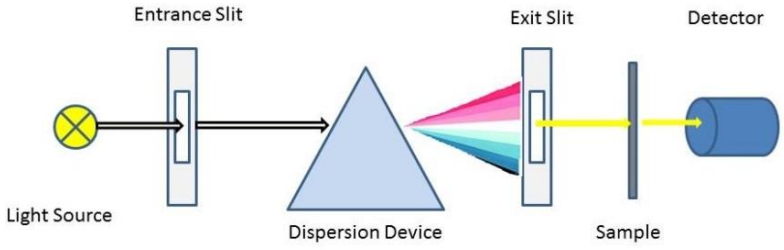

Figure 24: Schematic of UV-VIS-NIR Spectroscopy system.

In this study, Cary 500 spectroscopy is used to carry out the optical transmittance of substrates. This system offers the measurement range from 170 nm to 3300 nm. And absorbance can be calculated through transmission by Eq. (3.1) according to Beer-Lambert Law [143].

$$A = -\log(\%T/100\%) \quad (3.1)$$

where T is transmittance of the sample, which measures the intensity of light passing through a sample, and compares it to the intensity of light before it passes through the sample.

For an accurate measurement, a test of the substrate without coating precursor film was used as the reference sample.

3.3.5 Thermoelectric Power (Thermopower) Measurement

As mentioned in Chapter 2.3, thermoelectric power is a key parameter in the study of the thermoelectric effect for solar thermal devices and can help to uncover the thermoelectric properties of laser processed a-Si samples. Thermoelectric power is also called thermopower or Seebeck coefficient, and it is represented as S. To measure thermopower of the laser processed a-Si:H, a homemade chamber was developed (see *figure 25 (a)).* Two soldering heaters (maximum temperature is 350^{o}C), which a driven by the voltage supply were equipped both in the ends of the Cu sample holder. Thermocouples were attached above on the both ends of the substrate to measure the temperature difference (ΔT) through voltage reading feedbacks, and a Keithley 610C electrometer was connected to the first Cr contact to measure the thermoelectric voltage (in μV scale) in response to the difference of the temperature across the a-Si:H film. Meanwhile, the second Cr contact connected to the earth. This chamber was also alternative to measure the electrical conductivity (σ) just with connecting a 100V power supply to the second contact. On the external Cu rod, a tape heater or a jar of liquid N_2 was attached to control the mean temperature in the chamber. The chamber connected to a sorption pump system, offering

around 10^{-4} Torr measurement surrounding, which will prevent the heat loss and thermal diffusion. *Figure 26* shows the house – made thermoelectric measurement system.

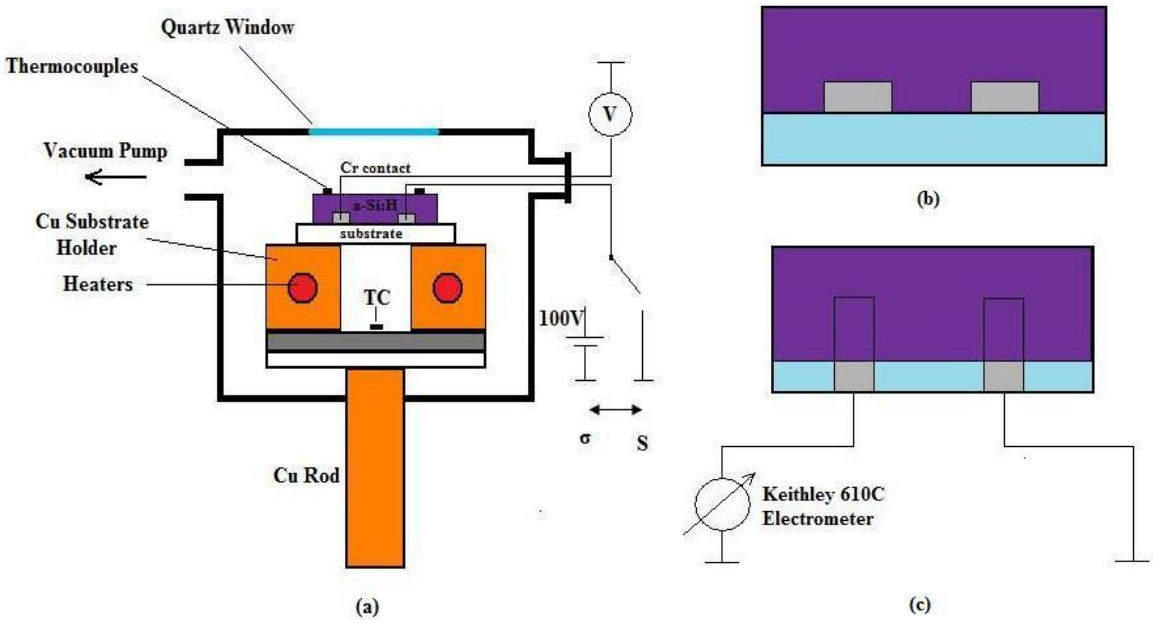

Figure 25: (a) Schematic of thermoelectric power measurement chamber. (b) Side view of the measurement substrate. (c) Top view of the measurement substrate.

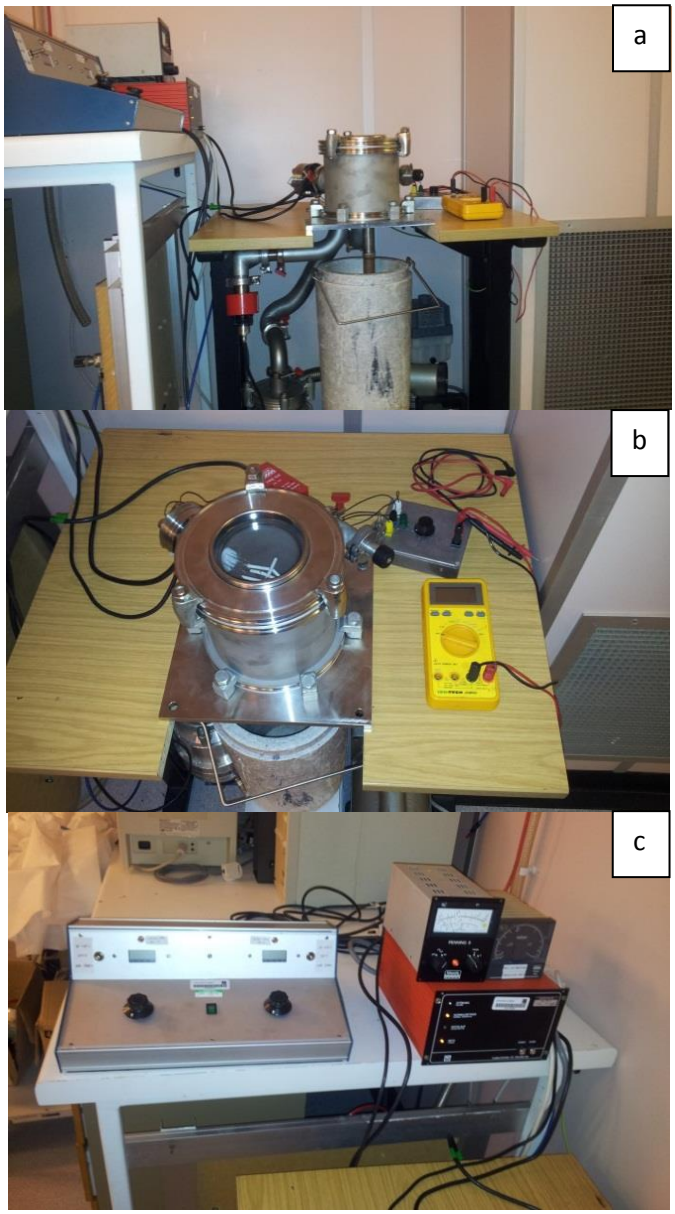

Figure 26: Home- made thermo-power measurement system a) chamber overview, b) chamber top view, and c) heating and pumping controller.

In a commercial bismuth telluride based alloy thermoelectric device, the typical thermopower of bulk n - type Bi_2Te_3 is around – 2200 V/K while the electrical conductivity of 1.1×10^5 S·m/m^2 with a thermal conductivity of 1.20 W/(mK). According to the equation 2.11 in Chapter 2.3.5, the ZT of the n-Bi_2Te_3 is equal to 0.45. When couple with the p-type

material, the total ZT of a commercial bismuth telluride based alloy thermoelectric device can reach 1 of ZT. The current research of thermoelectric materials are focus on thin film, nanocomposie- material, nano-sturcutre and other high thermopower with low electrical and thermal conductivity materials.

3.3.6 Solar Cell Efficiency Measurement

The efficiency of a solar cell is the parameter to determine how much sunlight that the device can convert into electricity, and it is also the most fundamental of the PV characterization techniques. The solar cell efficiency test is the standard that all the PV devices manufactured at different laboratories and companies with various development techniques to be compared. It is agreed that the standard solar cell device efficiency testing are:

1) Air mass (AM) 1.5 spectrum for terrestrial cells while AM0 for the space cells.
2) The light intensity of one-sun illumination of 1 kW/m^2 (100 mW/cm^2)
3) PV cell temperature of 293 K.

In our department, a Newport PV characterization system is used to identify the performance of the solar cell. The system is connected to a PC controlled current voltage source meter that can supply bias voltage to the device, and the PC will transfer the photocurrent response through the software, in this case, Labview was used. The schematic of the PV efficiency measurement kit is demonstrated in *figure 27*.

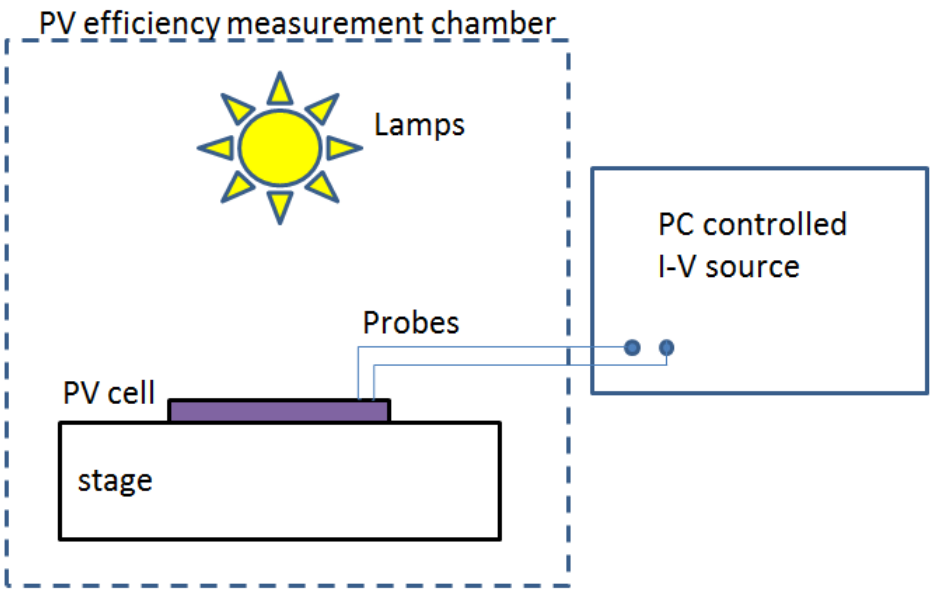

Figure 27: Schematic of solar cell efficiency testing chamber.

3.4 Electron Field Emission and Thermionic Emission Measurement Techniques

Electron emission measurements were carried out in a high vacuum chamber. The anode detects the electrons emitted from the cathode emitters on high applied voltage. In this research, for the field emission tests, the emitted electrons were detected and measured as current via the electrometer. And for thermionic emission test, an eagle glass based, planar Cr anode and a high vacuum compatible heater underneath the substrate was developed. For both experiments, we defined the field emission threshold as the applied field required to produce 1nA current.

3.4.1 Probe Type Electron Field Emission Measurement

The probe field emission measurement operated at pressures as low as 10^{-7} mbar. It adopts a hemispherical probe (1cm in diameter) anode which can be up or down positioned with as inch motor by the Burleigh motor controller. This results in a vacuum gap between the probe and the substrate (cathode) could be set in the range of 30- 500 μm. In *figure 28*, and a variable high voltage (range from 0-5000 V) applied to offer the voltage between anode and cathode via a Keithley 248 High Voltage Supply, and increase the voltage every 30- 120 seconds. Current readings were taken from the electrometer every 30- 120 seconds intervals.

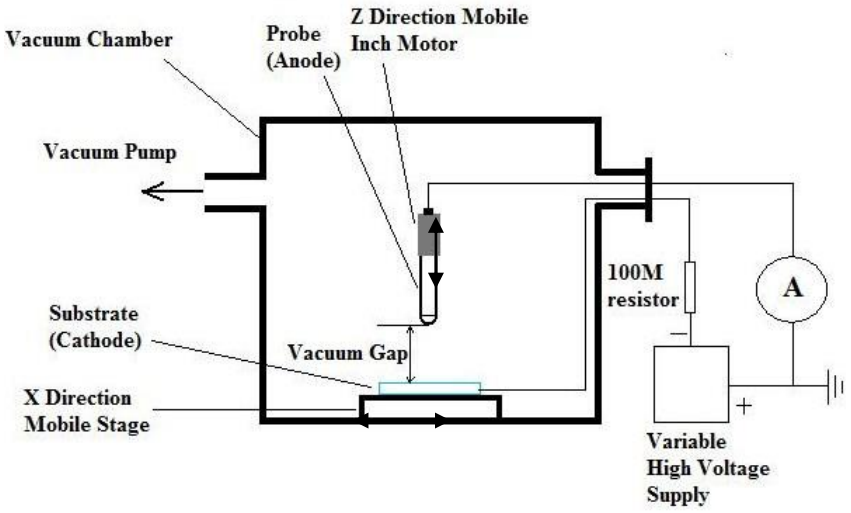

Figure 28: Schematic of probe type field emission measurement.

3.4.2 Thermionic Emission Measurement

The probe field emission measurement chamber was modified to measure the thermionic emission in this project. However, in order not to damage the inch motor (maximum working temperature is 250^{o}C), a patterned Cr flat anode was utilized (see *figure 29(a)*) to replace the probe, and this also allowed the electrometer to measure the

anode current due to the stable and robust electrical properties of Cr. Pure mica films (170 μm of original thick) were introduced to be the spacers to separate anode and cathode plates. A specially designed clip properly fixed the anode, spacers and cathode, and mount onto the vacuum compatible heater which was also well electrical and thermal insulated by mica films. A thermocouple was attached to monitor the cathode temperature. In our experiments, the measurement procedure was the same as the probe field emission one. *Figure 29(b) and 30* present the measurement chamber.

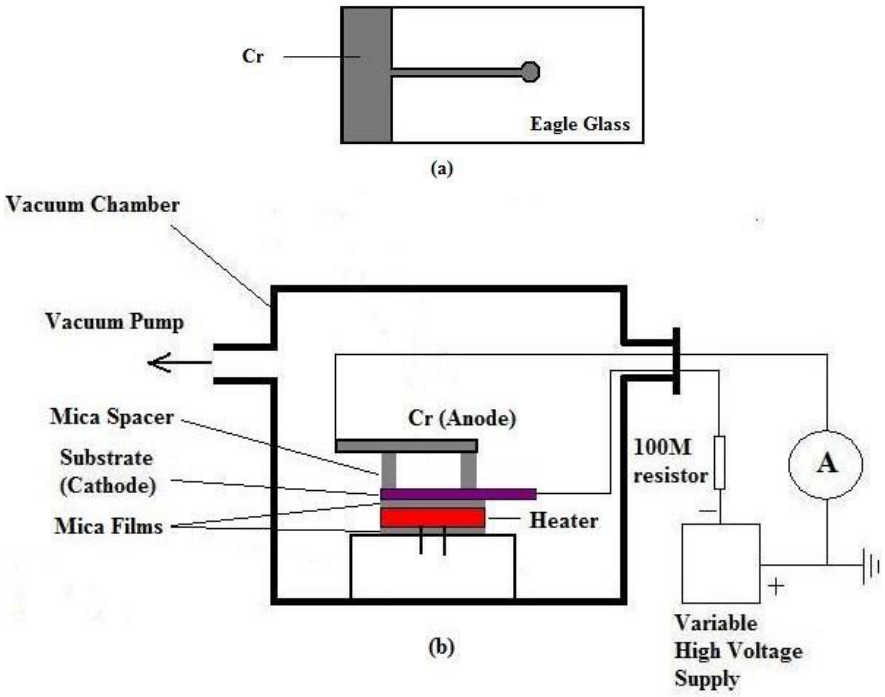

Figure 29: (a) Cr anode based on glass substrate. (b) Schematic of thermionic emission system.

Figure 30: Sample in substrate holder (upper) and TE measurement system (lower).

3.5 Summary

In this chapter, we have briefly introduced the operation principle of the three thin film deposition techniques used in this work: DC sputtering, PECVD and HWCVD. PECVD and HWCVD are particular for depositing a-Si:H film on silicon wafer or pre-sputtered metal substrates.

This is followed by introducing the excimer laser process, the technology used modify the surface and internal structure of the a-Si:H film by crystallization with high temperature and high power, allowing study of the surface morphology, electrical and optical properties of novel laser processed a-Si:H films.

Finally, we have briefly discussed the various thin film characterisation techniques which have been used in this research. SEM and AFM can help analyse and study the surface morphology of the laser processed or intrinsic films. With these microscopy technologies, we can also measure the height of the features responsible for geometric field enhancement during the field emission measurements. FTIR was used to investigate the H_2 and O_2 content in the silicon films before or after laser process. The UV-VIS-NIR spectroscopy allows us to study the optical absorption, transmission and reflection of different films, which is a useful tool in investigating the light trapping property of films used in solar absorber layers.

The last part of this chapter introduces two electron emission measurement systems. The probe type field emission measurement can efficiently measure the I-E curves from the silicon film emitters with various vacuum gap distances and different spot of the entire sample without opening the chamber and re- pumping. The thermionic emission system inherits the previous field emission chamber with a few of slight modifications. The planar Cr anode replaced the probe for high temperature compatible and equipped a heater for heating the cathode (monitored by the thermocouples). This study is the basis of the solar thermal device, and help us to understand the modified a-Si:H material.

4 Results and Discussion: Fabrication, Surface Morphology and Optical Properties of Large Area 'Black Silicon' Films

The black silicon (bSi) films in this work were developed by the KrF excimer laser processing of thick layers of a-Si:H films on various metal coated glass substrates or high purity cupper (Cu) plates. The homogeneous, high density and high aspect ratio sharp poly-Si spikes had been deposited on Si wafer by the different methods described in Chapter 2.4. However, fabricating bSi on metal coated glass substrate by excimer laser irradiation is an innovative developing method [99]. In this chapter, the fabrication process of the bSi film is discussed, and optical measurements had been done to investigate the optical properties of bSi to develop it as an absorber and give insight to the internal structure for the nanocomposite emitter. Moreover, a comparison among Moth-eye nanostructure antireflection layer, laser processed 'black copper' and 'black silicon' is also discussed. The fabrication of 'bSi' offers a manufacturing process with less steps and it is proved to be a material of near unity optical absorption and low cost, making it a perfect candidate for a sunlight absorber in a solar thermal device.

4.1 Fabrication of Black Silicon (bSi) Film with Excimer Laser Technology

To develop bSi films, firstly, a 400 nm thick layer of a-Si:H film was deposited on 100nm Al coated Corning 7039 glass substrates by the PECVD technique. During the deposition process, the RF power was set at10 Watts with the precursor gas SiH_4 at flow rate of 75 sccm. The substrate was kept at 220 ^{o}C. The process time of growing 400 nm thick a-Si:H is roughly 50 minutes with the deposition chamber pressure maintained at 100 mTorr.

Secondly, excimer processing was carried on the surface of the a-Si:H films in ambient atmosphere at room temperature. The laser system used in this study was an LPX*pro*210(F) KrF excimer laser with 248 nm wavelength and 20 ns pulse duration. The laser fluence has an asymmetrical slope-beam profile as shown in *figure 31*. And *figure 32* demonstrates the excimer laser beam profile. The substrates can be laser processed from the X direction or –X direction, which are defined as low laser energy as the leading edge and high laser energy as the leading edge, respectively. With X laser scanning, the substrates are to subject to a laser anneal with the energy andante and gradually increasing to a maximum, and then rapidly dropping off to zero. In contrast, with -X laser scanning, a sudden increase of the laser energy arrives to the substrates and quickly reach the maximum laser fluence and then gradually and slowly decrease to the zero.

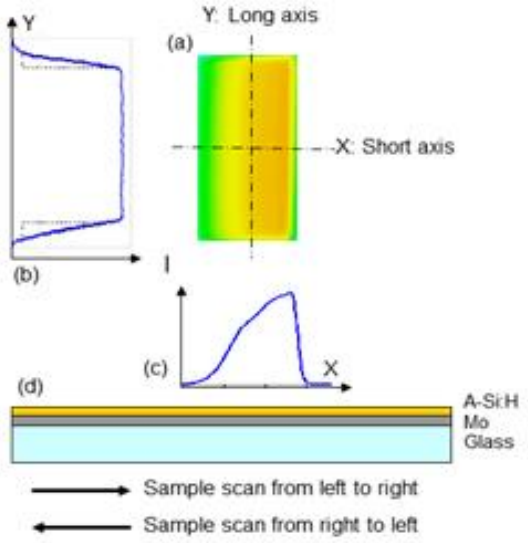

Figure 31: Schematic diagram of excimer laser microstructuring a-Si:H films using a slope beam profile, (a) top view laser beam pattern (4 mm × 8 mm), (b) top- flat beam profile along the long axis Y, (c) slope beam profile along the short axis X, (d) cross section view of the sample and the sample scan direction in ±X relative to the laser beam.

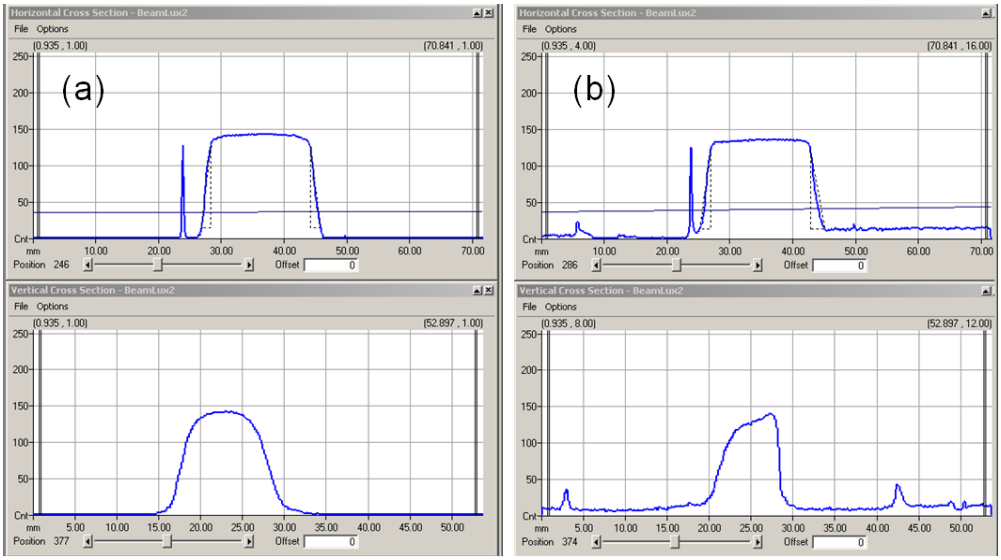

Figure 32: Live images of laser beam profiles both in horizental and vertical axis (a) Gaussian, and (b) Semi-Gaussian.

A computer controlled substrate stage allowed the movement of samples in two dimensions (X and Y directions) and the scanning speed was also handled by this. The detailed parameters of the excimer laser are given below.

The KrF Excimer Laser processing parameters are shown below:

Pulse profile	:	Top hat, Gaussian, and Semi-Gaussian
Laser Pulse area	:	4×8 mm^2
Wavelength	:	248 nm
Excimer Laser beam energy	:	100-400 mJ/cm^2
Pulse length	:	10-25 nano-second
Sample scan speed	:	0.5-5 mm/second

From previous study, it was found that the conical features, which are developed by laser irradiation with the high energy as the leading edge, possesses remarkable field emission properties than that irradiated by the low energy as the leading edge [98]. However, in this work, when the a-Si:H film is annealed by excimer laser with the low energy as the leading edge with the same laser energy, from the SEM images in *figure 35*, pillar-shaped micro spikes are formed, and also, the darker film surface can be observed directly by the eyes in *figure 33*. This presumes that the micro pillars poly-Si can absorb and trap much more lights, and optical measurements were taken to identify or prove this assume in the next section. To correlate the surface morphology of the irradiated films with the excimer laser processing parameters, the irradiated a-Si:H film surfaces were observed by SEM.

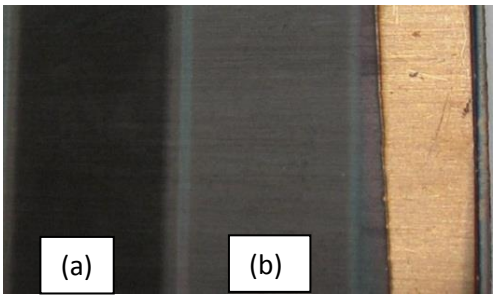

Figure 33: Images of black silicon on Cu plate. (a) Excimer laser processed strip with substrate on X scanning direction. (b) Excimer laser processed strip with substrate on –X scanning direction.

The laser dosage can be validate through adjusting the laser processing parameters, such as scanning speed, laser pulses on unit and pulse energy. When the number of laser pulses on unit was increased from 100 to 800 (100, 200, 400 and 800), the amorphous silicon melting process goes deeper and more films are involved in the melting and resoliding process. Equation 4.1 explains the calculation of the laser pulse power.

$$Laser\ Pulse\ Power = Pulse\ Energy/Pulse\ Duration \qquad (4.1)$$

During the resoliding process, due to the capillary action, the direction of molten silicon is toward the nucleation site which was at a lower temperature. The molten silicon then re-solidifies as it combines with the pre-existing nucleation growth as well as contributing to the spike height increment s. This results in the nucleation site evolving from a hillock and bumpy structure into a shaper feature. The repetition of this laser process finally leads to the formation of the sharp micro-structures. In *figure 34*, the mechanism formation of the silicon spikes are illustrated. However, if the laser processing carries on, the entire silicon film will be used up so that the underlying substrates (metal coated glass or metal foil) and will cause the metal crack or damage as well.

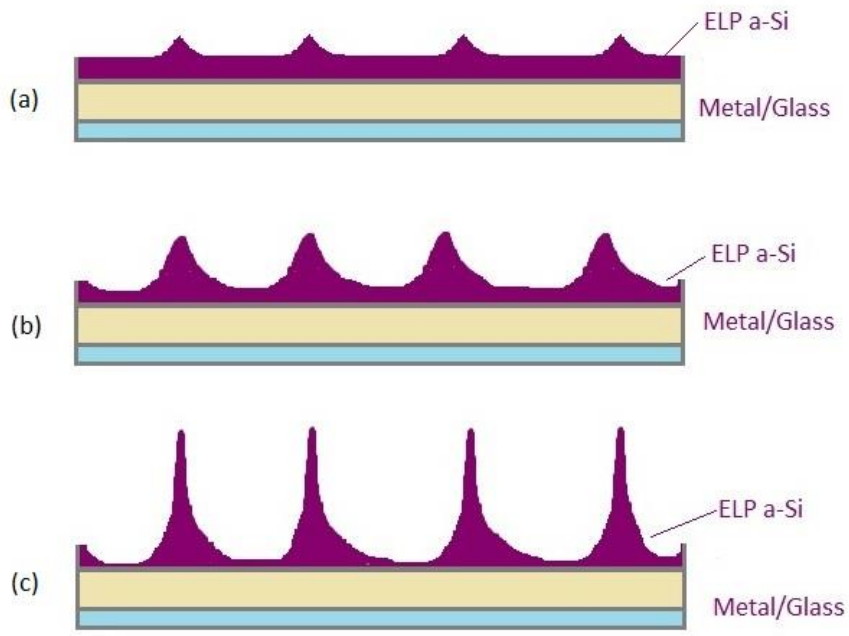

Figure 34: The mechanism for the silicon spikes array formation by ELP of a-Si. (a) Bump micro-features of the a-Si film. (b) Flow of molten liquid toward the peaks contributes to the increase in height. (c) Sharp pillar micro-features at the finish stage.

4.2 Growing Conditions of Black Silicon Films

In order to confirm the growing environments of bSi films and optimise the films as absorbers and nanocomposite emitters, more experiments were carried out as described below:

- Excimer laser process 400 nm a-Si:H on mainly used glass coated metal: Mo/ Cr/ Al
- Repeated also on ITO/ Si Wafer/ Cu plate.
- Excimer laser processing 400 nm a-Si:H in SF_6/N_2/Vacuum environment.

In order to investigate the growing environments of bSi film, all the a-Si:H substrates were laser processed under the same conditions, scanning in the –X direction with same laser frequency, energy and scanning speed.

In *figure 35*, excimer laser processing a-Si film was performed on Mo coated Corning glass substrate in room temperature. 4 different laser energies: 160 mJ, 180 mJ, 200 mJ and 220 mJ were used to irradiate the PECVD as-grown a-Si:H films with same other scanning conditions. 160 mJ laser beam energy was set on the PC controller and then carried out on the 400 nm a-Si substrate. In *figure 35 (a) and (b)*, the SEM image showed an uniform silicon array and the height of the spikes are in the range of 1.5 μm to 2 μm with the separation of 700 nm to 1 μm. With increasing the laser energy to 180 mJ, in *figure 35 (c) and (d)*, black silicon array with same structure was observed.

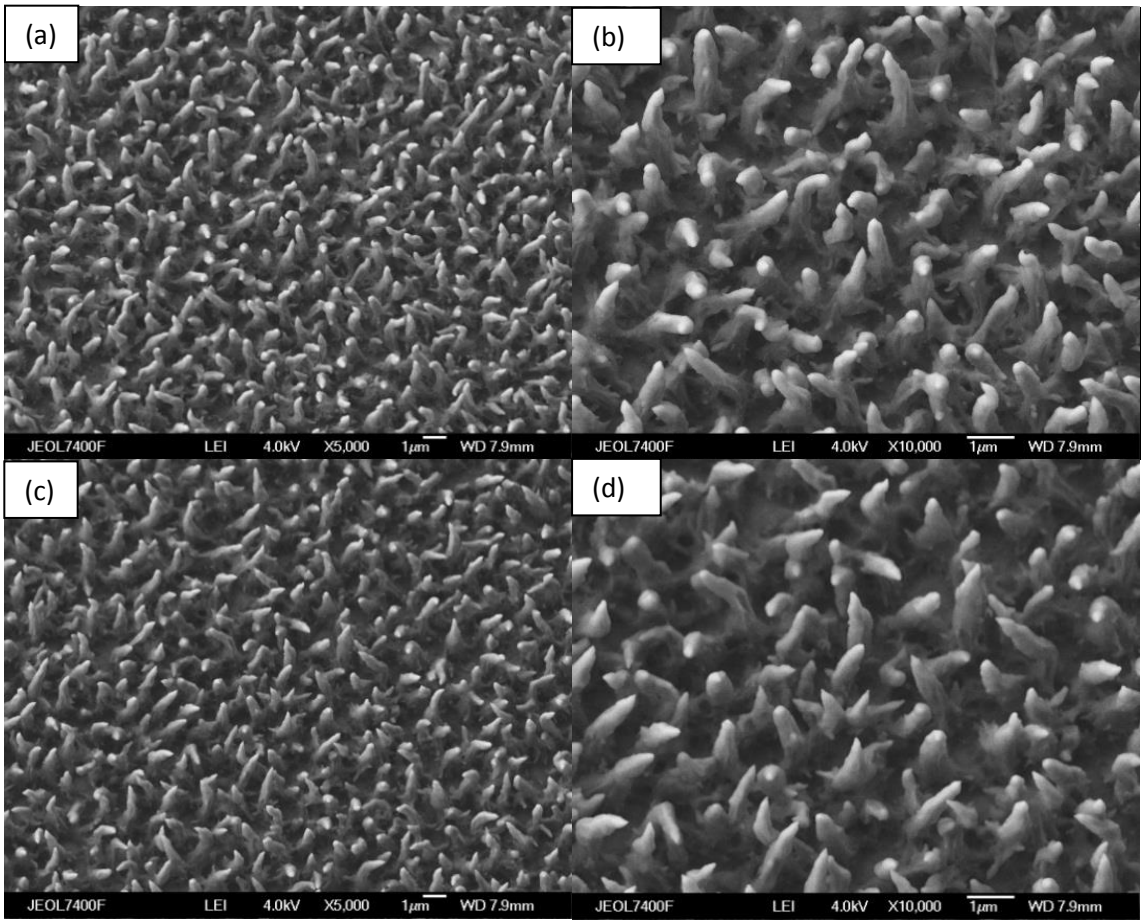
(a)
JEOL7400F LEI 4.0kV X5,000 1μm WD 7.9mm
(b)
JEOL7400F LEI 4.0kV X10,000 1μm WD 7.9mm
(c)
JEOL7400F LEI 4.0kV X5,000 1μm WD 7.9mm
(d)
JEOL7400F LEI 4.0kV X10,000 1μm WD 7.9mm

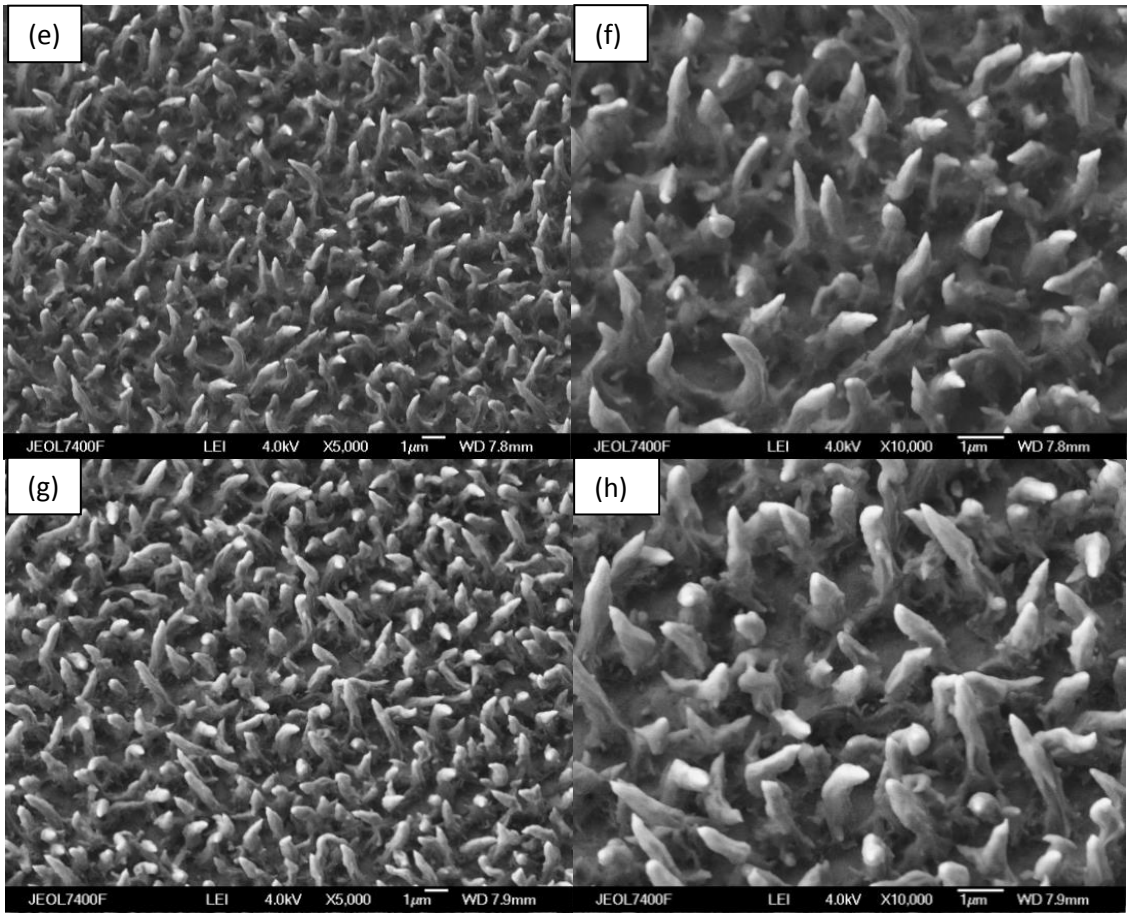

Figure 35: SEM images of excimer laser microstructuring a-Si:H film on Mo substrate with different laser energy. (a,b) 160 mJ, (c,d) 180 mJ, (e,f) 200 mJ, (g,h) 220 mJ. With an overall viewing angle of 20^{o} to the surface normal.

To understand the growth condition of the bSi film, the excimer laser beam energy was further increased to 200 mJ and 220 mJ. The SEM images in *figure 35 (e), (f), (g) and (h)* presented the surface morphology of the microstructures of the laser irradiated a-Si films with higher energy. However, no obvious changes were shown in the SEM images that the height and the separations between spikes are nearly same as using 160 mJ laser energy. This indicates that the black silicon can be developed on the Mo coated glass substrate in a broad range of the excimer laser energy. From our experience, in this study, the laser energy below 160 mJ is too low to melt and resolid the a-Si:H film to form the

high aperture silicon spikes while the energy higher 220 mJ is too powerful to damage the as-grown a-Si film.

To validate and understand the growth condition of the black silicon film, different conductive base materials were studied: Cr, Al and ITO. The excimer laser parameters were kept the same except the beam energies, which were the same as in the previous study with Mo back contacts. *Figure 36, 37 and 38* are the SEM images of Cr, Al and ITO back contacts, respectively. In *figure 36*, it is observed that the black silicon grown on Cr thin film as the back contact has same structure as Mo back contact. It is also calculated through the SEM image that the height of the silicon spike is in the same range, 1.5 µm to 2 µm, with the separation of 700 nm to 1 µm. The silicon spikes were well grown and without any damage in the laser energy from 160 mJ to 220 mJ.

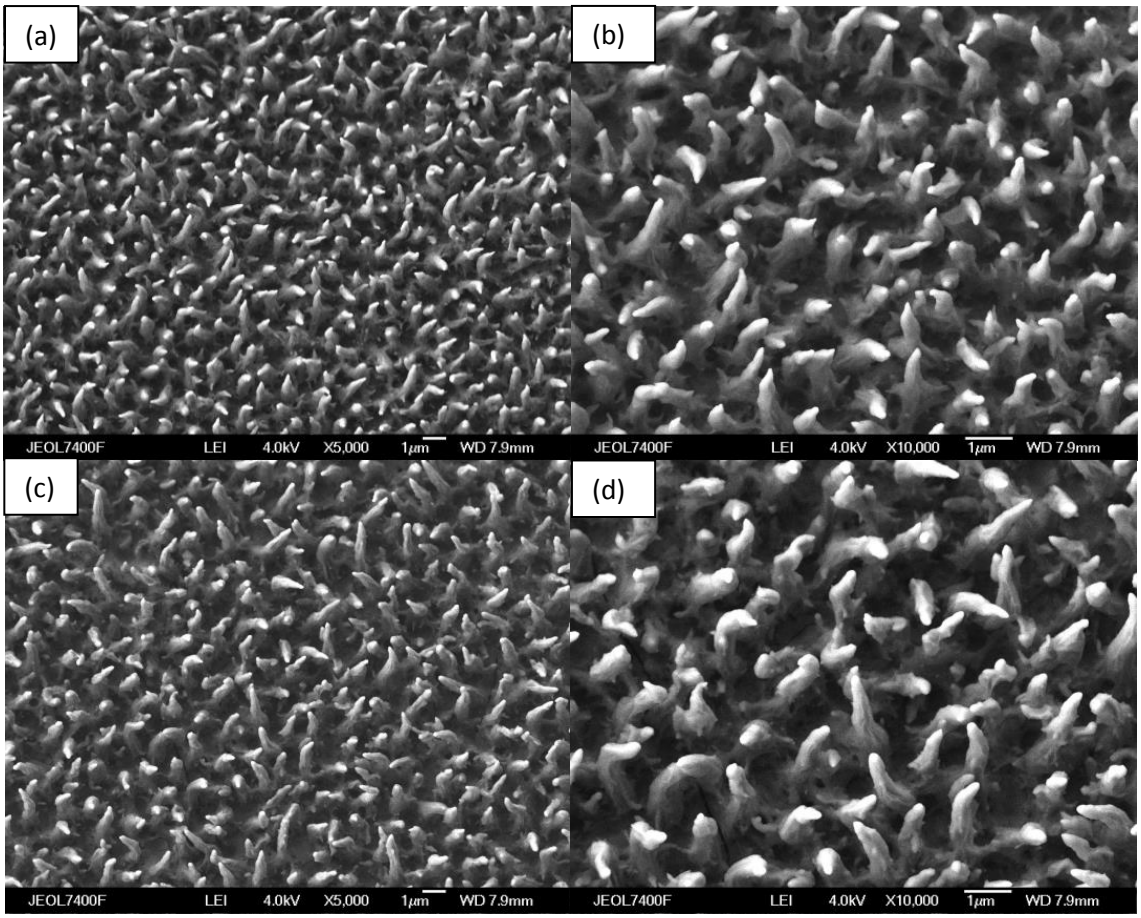

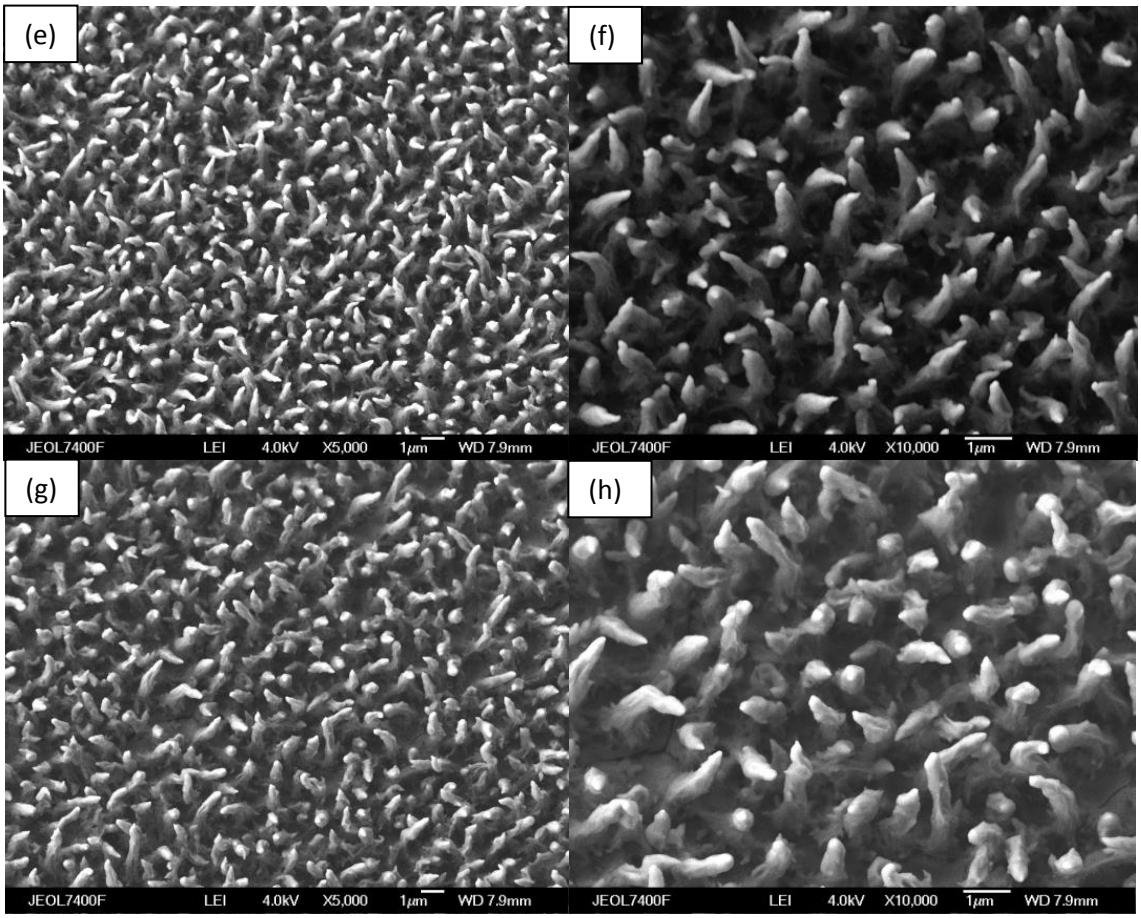

Figure 36: SEM images of excimer laser microstructuring a-Si:H film on Cr substrate with different laser energy. (a,b) 160 mJ, (c,d) 180 mJ, (e,f) 200 mJ, (g,h) 220 mJ. With an overall viewing angle of 20^{o} to the surface normal.

The further study of the black silicon with thin Al film as the back contact is valuable to this study as Al is a potential element that we can use the excimer laser to dope it into the a-Si layer while microsturcturing. When the a-Si film was irradiated by 160 mJ laser energy, a similar structure to Mo and Cr contacts was obtained. However, when further increased the energy to 180 mJ, 200 mJ and 220 mJ, a blunt, unsharp structure was noticed through the SEM images in *figure 37.* And also, in the lower magnitude image in *figure 37 (c), (e) and (f),* some damages and cracks were observed.

As the laser irradiation conditions were kept the same, that indicates that the back contacts influence the growth of the bSi as well as the damage and cracks. *Table 5* lists the thermal conductivity of these three metal elements, ITO and air as the reference. The thermal conductivity is known as the property of a material to conduct the heat, so the heat transportation of Al is nearly double than that of Mo and Cr and much higher than ITO.

In our case, the laser pulse power generates heats when scanning the substrate, which will melt the a-Si film and re-solid after. Due to the high thermal conductivity of the Al substrate, the a-Si can melt and re-solid under relatively lower laser power than Cr, Mo and ITO substrates. However, on raising the laser power, with the temperature increased, the Al substrate was then cracked while the Mo, Cr and ITO were still continuous. This indicated that black silicon by excimer laser processing requires higher laser energy on the lower thermal conductivity back material as the substrate and is not easily damaged.

Nevertheless, the study of excimer laser processing a-Si on an Al base substrate is valuable because with suitable laser energy, the laser processing has the potential to dope the bottom Al into a-Si film by melting and re-soilding to form a p-type film. This will be explained in detail in the next chapter on a silicon nanowire solar cell.

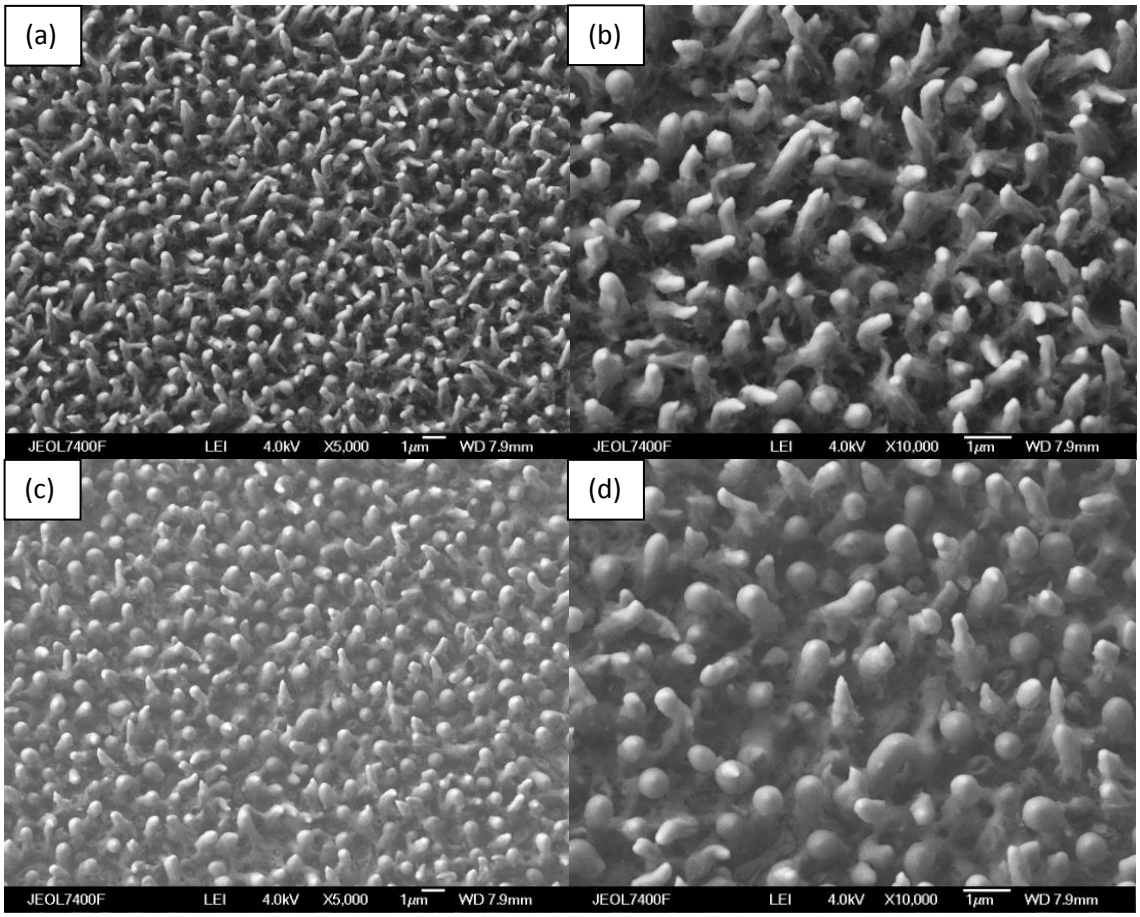
(a)
(b)
(c)
(d)
JEOL7400F LEI 4.0kV X5,000 1μm WD 7.9mm
JEOL7400F LEI 4.0kV X10,000 1μm WD 7.9mm
JEOL7400F LEI 4.0kV X5,000 1μm WD 7.9mm
JEOL7400F LEI 4.0kV X10,000 1μm WD 7.9mm

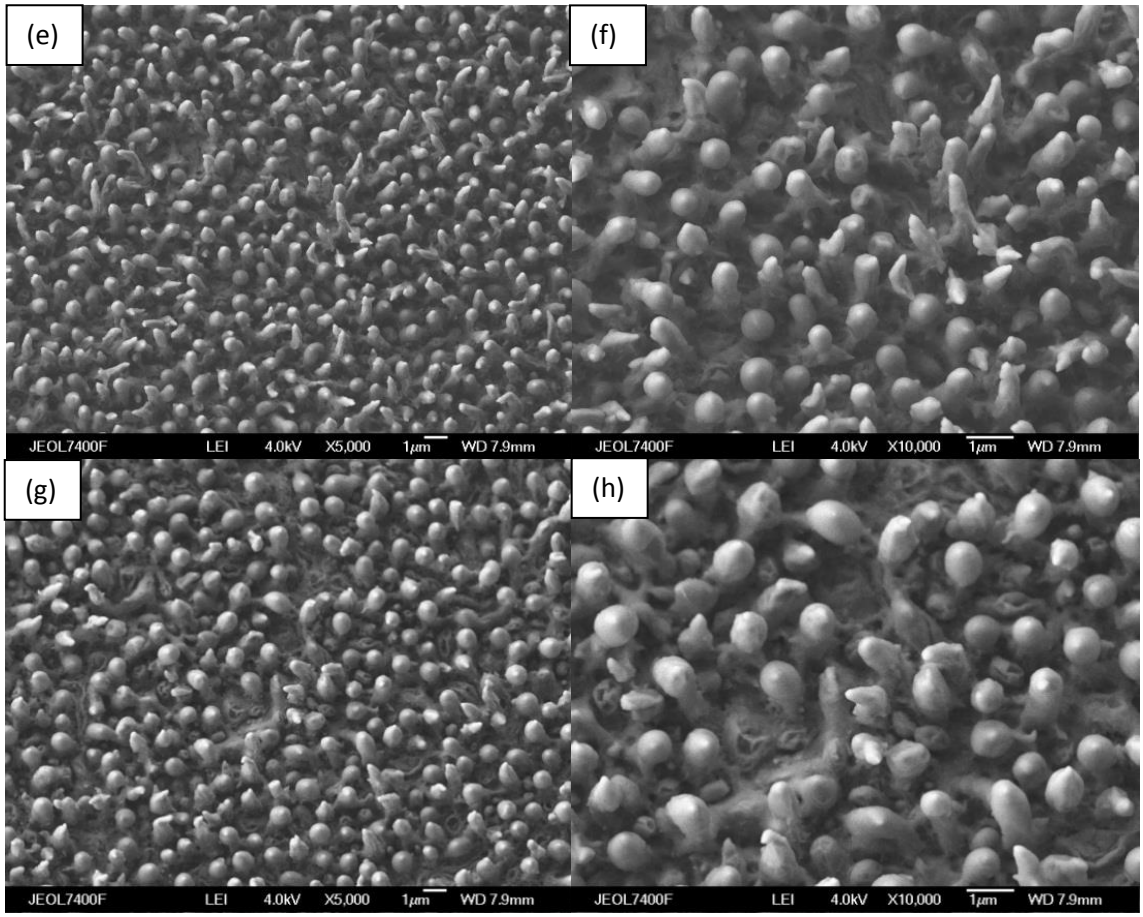

Figure 37: SEM images of excimer laser microstructuring a-Si:H film on Al substrate with different laser energy. (a,b) 160 mJ, (c,d) 180 mJ, (e,f) 200 mJ, (g,h) 220 mJ. With an overall viewing angle of 20^{o} to the surface normal.

Elements	Thermal Conductivity (W/mK)
Molybdenum	138
Chromium	94
Aluminium	205
Copper	401
Indium Tin Oxide (ITO)	10-11 [144]
Air (as reference)	0.024

Table 5: The thermal conductivity of Mo, Cr and Al [145].

Indium Tin Oxide (ITO) is an important material in semiconductor research because it is mostly transparent in the visible spectrum with low electrical conductivity, which is popular used in various optical coating applications, such as solar cell, LED etc.

In this research, commercial Corning ITO (100 nm thick) on glass substrates were also used as the base substrates to develop black silicon films. 160 mJ and 220 mJ laser energy were used to investigate the laser processing, and the SEM images in *figure 38* states the microstructure of the black silicon films on ITO.

From the SEM images, it was observed that the features of the excimer laser developed black silicon on ITO films are similar to those on the Cr and Mo substrates. This work also proved that the lower thermal conductivity materials can be used as the back substrate in developing black silicon film by excimer laser processing with higher laser energy as well as being robust to thermal shock.

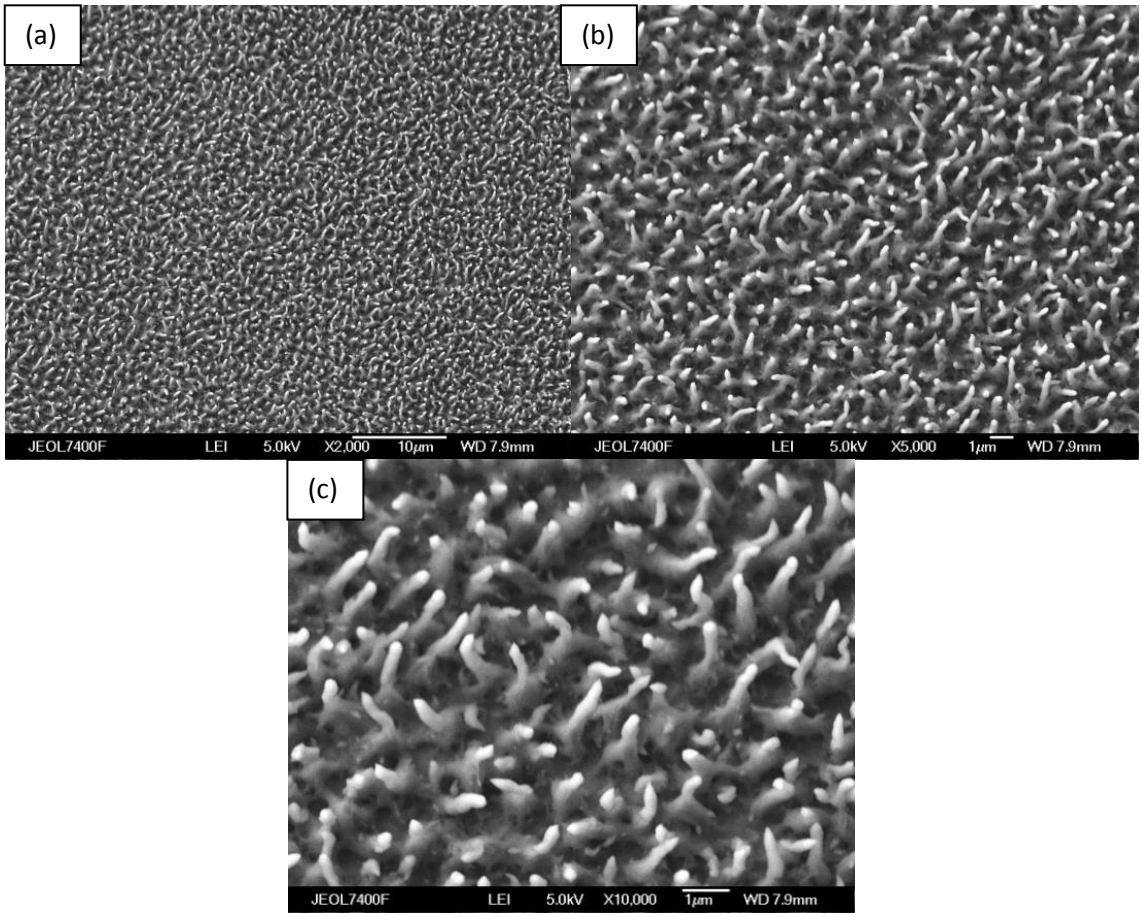
(a)
(b)
(c)
JEOL7400F LEI 5.0kV X2,000 10μm WD 7.9mm
JEOL7400F LEI 5.0kV X5,000 1μm WD 7.9mm
JEOL7400F LEI 5.0kV X10,000 1μm WD 7.9mm

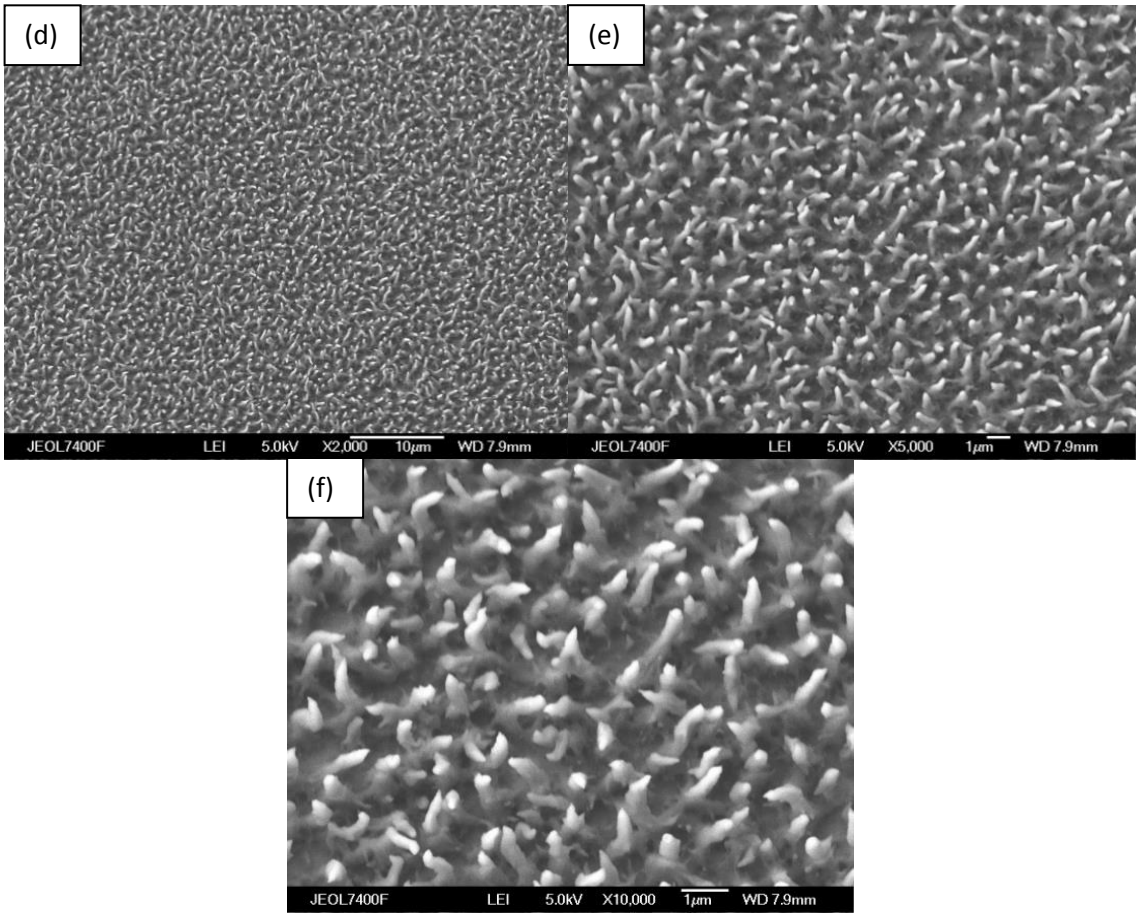

Figure 38: SEM images of excimer laser microstructuring a-Si:H film on ITO coated glass substrate with different laser energy. (a,b,c) 160 mJ, (d,e,f) 220 mJ. With an overall viewing angle of 20^{o} to the surface normal.

The excimer laser condition of the growth of bSi film on various base substrates have been studied. The micro-pillar shape silicon arrays have been fabricated with lower laser energy on Al, a high thermal conductivity material, while similar micro structures were obtained on the lower thermal conductivity Cr, Mo and ITO substrates with higher laser energy.

To further study the black silicon growth condition in different gaseous elements, fixed laser parameters were adapted on Al substrates in Air, N_2, SF_6 and in vacuum. The

results showed that during the bSi process, oxygen plays an important role and affects the micro structure considerably.

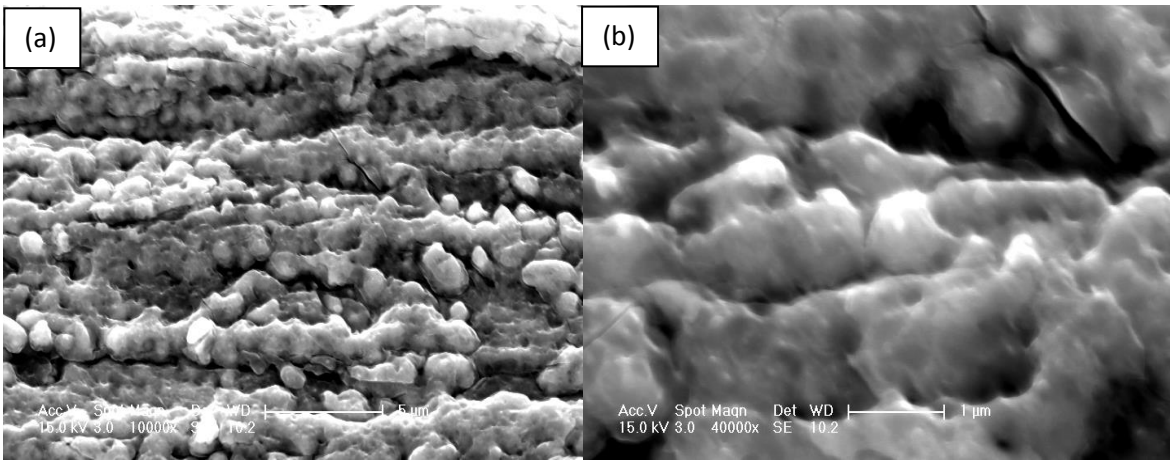

Figure 39: SEM images of excimer laser processed 400 nm a-Si:H films with low energy as the leading edge in SF_6 with the titled angle of 30^o.

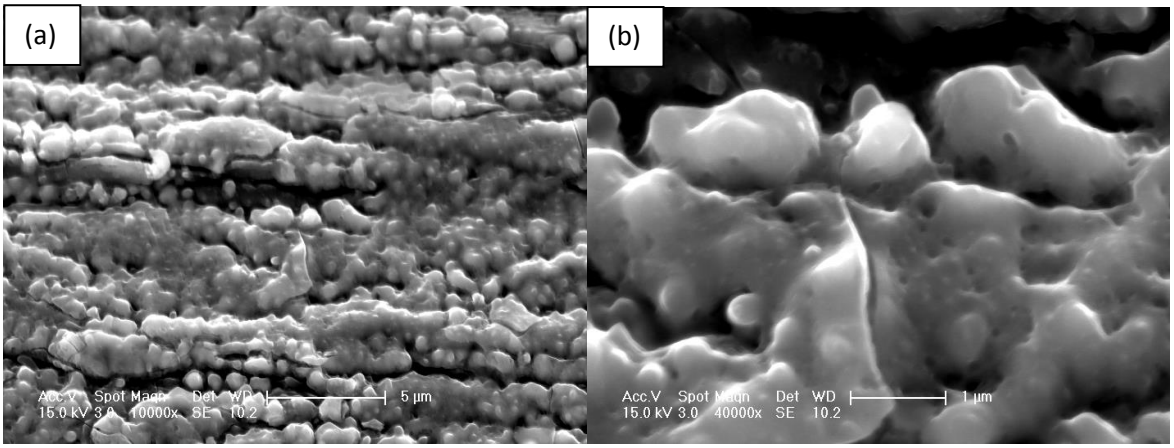

Figure 40: SEM images of excimer laser processed 400 nm a-Si:H films with low energy as the leading edge in vacuum with the titled angle of 30^o.

In *figures 39 and 40*, the substrates used in this study were 100 nm Al coated corning glass slides. Compared to *figure 36*, the excimer laser processing in air, there were no obvious nano - conical or pillar structure spikes observed, while just the rough surfaces were obtained. The laser energy used in this fabrication is 160 mJ and frequency is 50 HZ with the substrate scanning speed of 0.5 mm/s. In previous section, this laser parameter was able to develop a 1.5 μm height with 800 nm separations silicon nano - pillar array.

SF_6 is utilized by Mazur's group to fabricate black silicon arrays on crystalline silicon. However, they use a high- fluence femtosecond (fs) laser to irradiate n type silicon wafers [92, 93, 146]. In our work, with SF_6 as the processing gas, no microstructures were found. The difference between their work and ours are 1) laser type: fs laser and excimer laser, and 2) substrate material: n type silicon wafer and a-Si:H on metal, and this results a rapid thermal transportation. Regarding the experimental results of excimer laser crystallization of a-Si in SF_6, vacuum and in air, the morphology of resultant bSi film is related to the oxygen so that the material is likely to contain oxygen. The EDX (Energy-dispersive X-ray spectroscopy) measurements below show the observation of oxygen in the bSi films. The EDX provides an elemental analysis or chemical characterization of the samples.

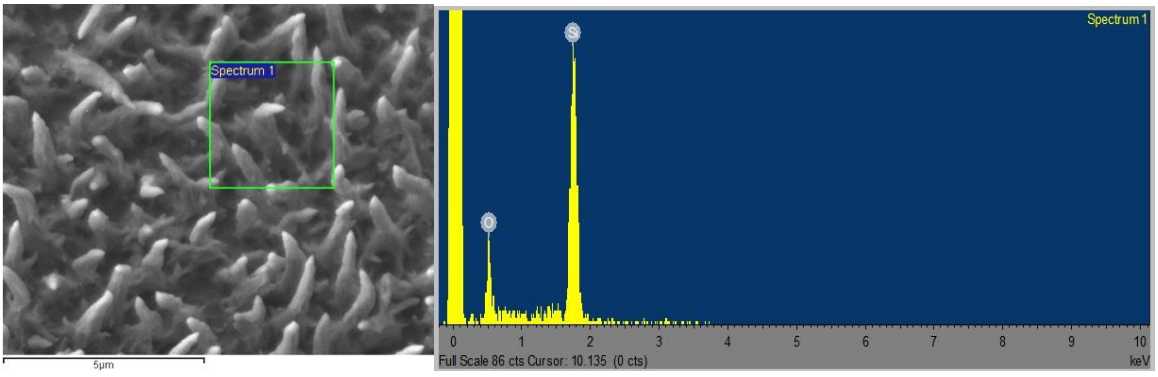

Figure 41: EDX measurement of 3μm × 3μm area of bSi film.

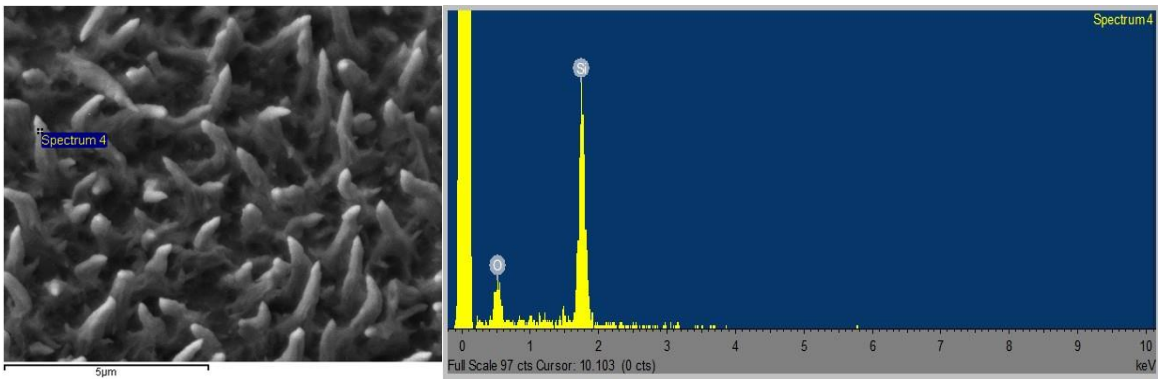

Figure 42: EDX measurement on the tip of bSi micro spike.

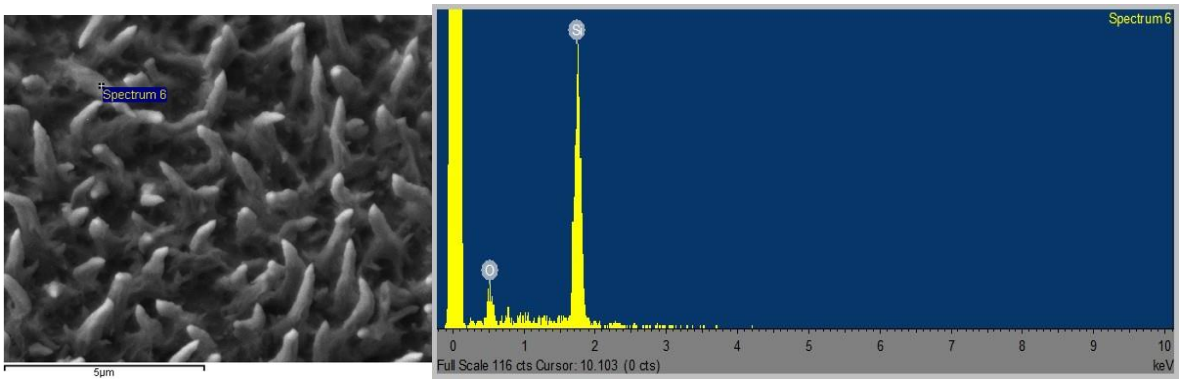

Figure 43: EDX measurement on the middle of the bSi spike.

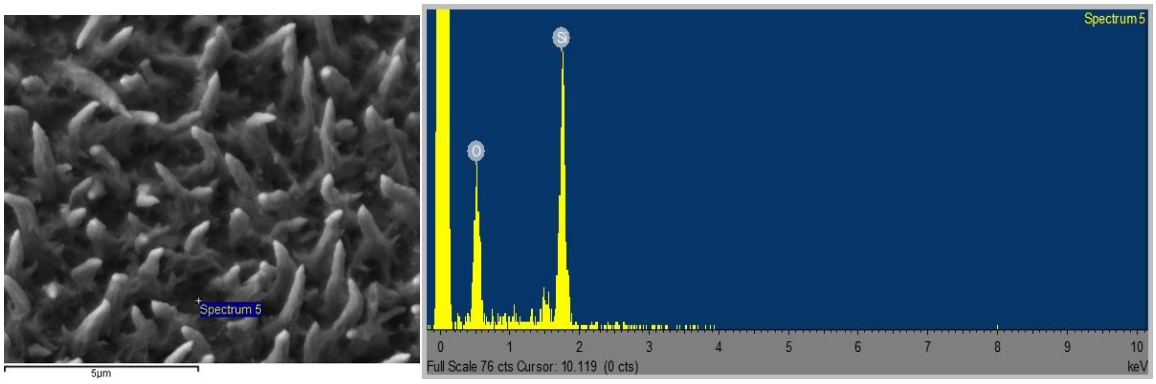

Figure 44: EDX measurement on the bottom of bSi film.

The X-ray analyses confirm the presence of silicon and oxygen in the bSi film as shown in *figure 41* to *figure 44*. This structure enhances the sun lights trapping and can also efficient in transport heat in a sunlight absorber application. We will see in Chapter 4.3 that the material is an oxynitride that contains discrete nanostructures that dominates the electron transport and renders it an efficient field and thermionic emitter. This is the essence of the cathode in the solar thermal device. The nanocomposite nature of the material is explored by further analysis of the internal structure. However, we have seen that the material is also an efficient absorber, and this element of operation is also explored below.

4.3 Electrical and Optical Properties of Black Silicon Films

In order to study the optical properties of the black silicon, Fourier Transform Infrared Spectrometry (FT-IR) measurement was carried out. In this measurement, a single beam Mattson 7000 FT-IR spectrometer was used, and the wave numbers are scanned from 400 to 4000 cm^{-1} (2.5 μm to 25 μm) at a scan speed of 0.4 cm per second in air. To study the optical properties of laser processed amorphous silicon under different atmosphere conditions in the region of the middle of the IR spectra, substrates were prepared with 400 nm laser processed a-Si:H on n type silicon wafer instead of copper plate due to the measurement equipment requirement. The FT-IR is a method which can simply measure the oxide of silicon in infra-red spectrum [147]. In *figure 45*, the infrared spectra of excimer laser irradiated a-Si:H film is shown. The Si-H vibration absorption peaks are roughly at 630 cm^{-1} (0.076 to 0.11 of laser process with high energy as the leading edge and 0.011 to 0.03 of laser process with low energy as the leading edge) and 2000 cm^{-1} (0.076 to 0.083 of laser process with high energy as the leading edge and 0.012 to 0.015 of laser process with low energy as the leading edge). Si-O and Si-N bonding are in the range of 1000-1300 cm^{-1} (0.076 to 0.08 of laser process with high energy as the leading edge and 0.011 to 0.02 of laser process with low energy as the leading edge).

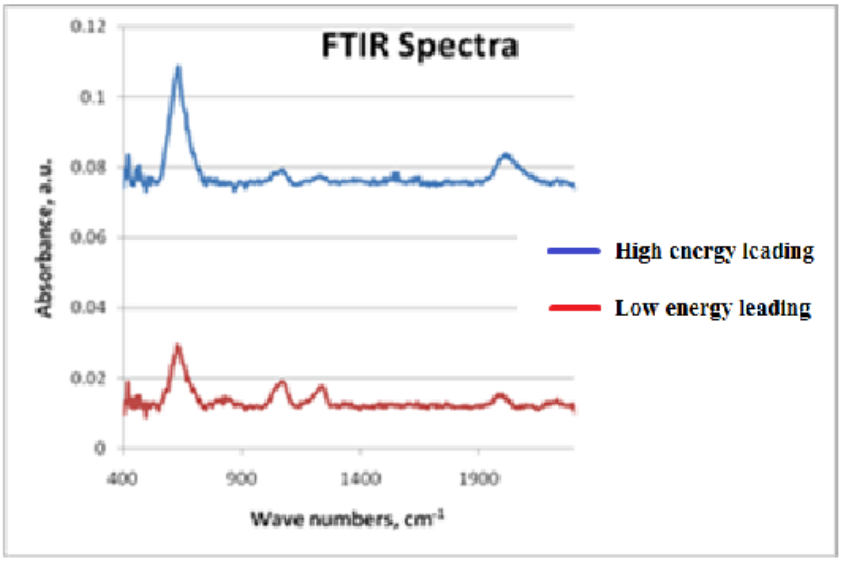

Figure 45: FT-IR spectra of high energy leading and low energy leading laser processed amorphous silicon films

With two simple steps, the novel bSi films can be rapidly grown with relatively low cost, feasible to produce in large scale and on variety of low melting point substrates including silicon wafer as well as flexible substrates such as PET and PEN plastic sheets. This gives the possibilities to develop bSi into a number of applications, such as large size sunlight absorber.

To be the light absorber in a solar thermal device, the bSi should absorb photons as much as possible in the region of visible lights (wavelength of 380nm to 740nm) while reflecting as little as possible.

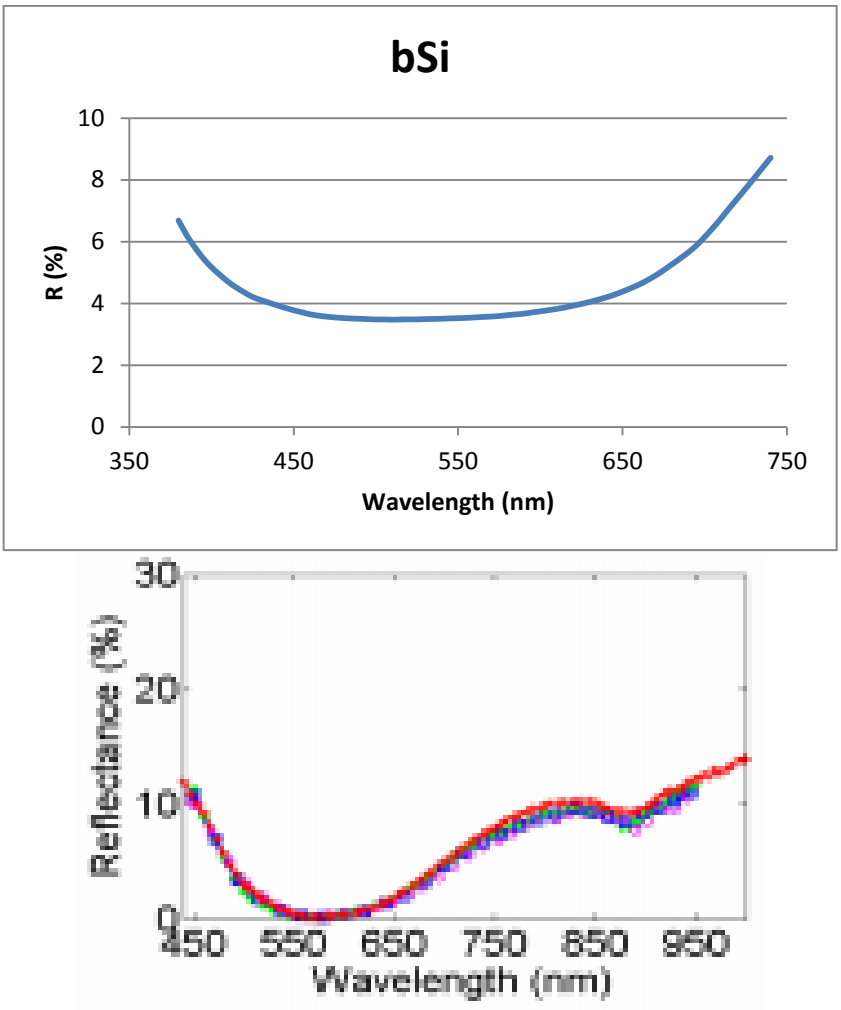

Figure 46: Reflectance of (a) black silicon (from excimer laser processing 400 nm a-Si:H film on Cu) and (b) Moth-eye structure [148] between wavelength range of 380- 740nm.

From *figure 46*, in the region of 380 – 740 nm, an average around 5% of reflection can be calculated. The lowest reflection of 3.2% is at the wavelength of 500 nm, while highest of reflection 8.4% occurs at 740 nm. Thus, the bSi film exhibits excellent properties in absorbing visible light with minimum reflection, which is a positive and important factor to the application of acting as the sunlight absorber. It is also comparable than novel Moth-eye structure anti-reflection layer fabricated by University of Southampton [148].

In order to study the crystalline fraction of the bSi films, Raman spectroscopy of the optical phonon modes of the system is performed with a Renishaw 2000 Raman microscopy system with an excitation wavelength of 782 nm [149]. The Raman shift spectra of the bSi substrates with X and -X scanning directions are displayed in *figure 47*, results were obtained (kindness of S. Silva) at the Advanced Technology Institute (ATI), University of Surrey.

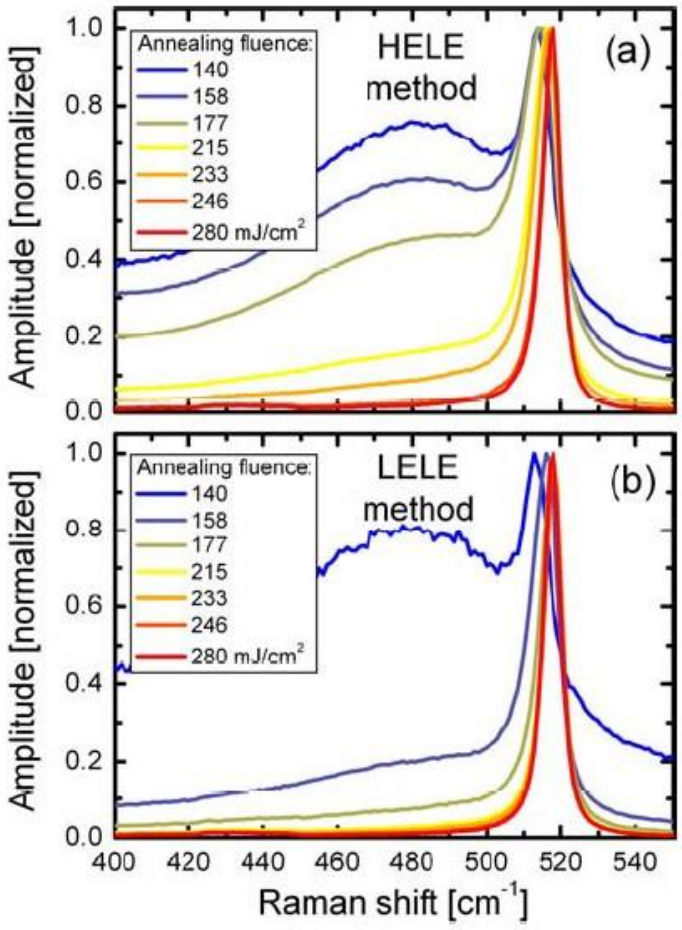

Figure 47: Raman – Spectra for the substrates produced with (a) the high energy as leading edge (HELE, -X direction) scanning method and (b) with the low energy as leading edge (LELE, X direction) method, with annealing fluences in the laser power range of 140-280 mJ/cm^2 [149].

In *figure 47,* the normalized Raman spectra in the range of the wavenumber from 400 to 540 of the substrates, which were laser annealed by X and –X direction, respectively. The annealing fluence in this study was from 140 to 280 mJ per cm^2 as displayed in the legend in *figure 47*. The broad peak roughly on 480 cm^{-1} due to the vibrations of Si-Si bonds in a-Si:H films, red-shifted and broadened attributed to the structural disorder compared to the vibration of the Si-Si bonds in c-Si film which was observed as a sharp peak on the wave number of 518 cm^{-1}. This was because that the larger variations in bond orientations and lengths c-Si films. From this Raman study, it confirmed that when higher laser annealing fluences were used more of the material will melt and subsequently recrystallize. The substrates with X laser scanning direction showed a higher degree of crystallinity than the substrates with –X laser scanning direction for a fixed laser annealing fluence.

The crystalline quality of the interior of the ELP a-Si:H samples were investigated by a high- resolution transmission electron microscope (HR-TEM), which is displayed in *figure 48* at a 285,000 × magnification of a bump on the surface of a excimer laser processed substrate. At this resolution the crystal planes of crystalline silicon were visible within the domain of the Si bump in the lower left corner. The 2D Fourier transforms of the images in the regions marked '1', '2' and '3' are presented in *figure 47* as well, with contrast strength to illustrate the obvious peaks corresponding to the first order diffraction from the crystalline planes. The separations of the peaks correspond to a lattice period of (3.3±0.2) angstrom, in good agreement with the lattice periodicity of the Si (111) plane of 3.14 Å. All regions displayed the same orientation of the Fourier transform pattern, indicative of a single-crystalline interior of the Si domain [150].

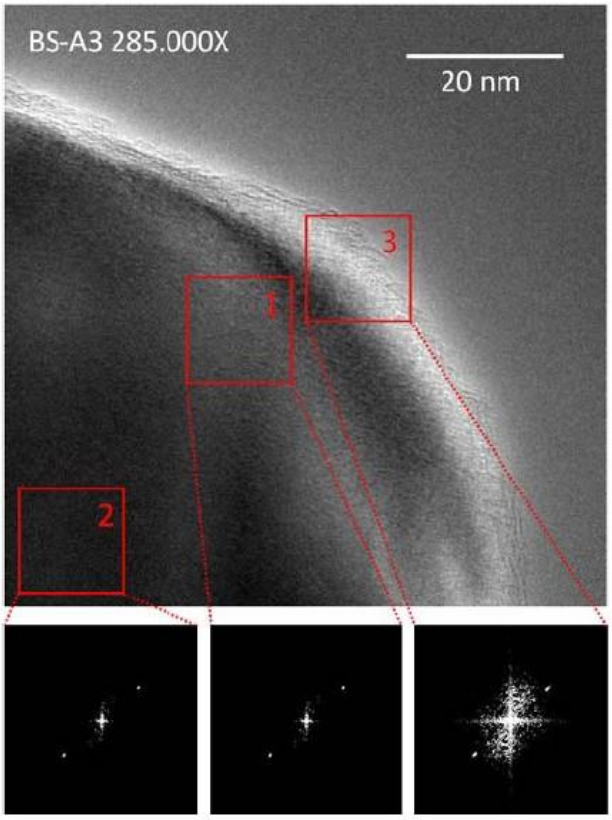

Figure 48: High resolution TEM (HR-TEM) image at 285,000 X magnification of a representative silicon structure on the surface of a bSi substrate. 2D Fourier transforms of the areas 1, 2 and 3, indicative of the crystallinity within these areas, are shown below the main panel [149].

As a conventional and well developed technique normally used for anti-reflection in solar cells, moth-eye structure can dramatically absorb the sun light to maximize the solar performance. The idea initially was hinted by the surface of the cornea of some night-flying moths, and this sub-wavelength nature structure exhibit an effective refractive index which can minimize the reflection of the lights [150]. Boden and Bagnall have simulated the moth-eye structure as the ARC in silicon solar cells [127, 151] and can reach an ultralow average reflection of 1% in the spectral range between 400 nm to 1000 nm [152]. The SEM image in *figure 49* showed a nanostructure of the moth-eye with pillar height of 250 nm and separation of ~100 nm.

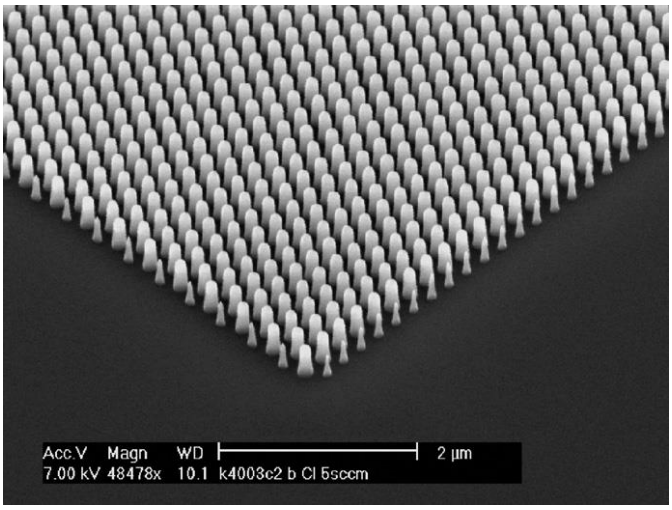

Figure 49: SEM micrograph of a silicon 'moth-eye' antireflection surface [151].

According to their results, this single nanostructure layer can increase 18% of the reflection of the total number of photons incident on the surface.

The functional moth-eye has a similar micro-structure as the bSi shown in *figure 35 to 39*. However, regarding the fabrication methods, moth-eye nanostructure requires acid solution [153], multi-steps [154] or slow but expensive facilities [155]. Both these techniques make the moth-eye structure to experience a bottleneck as a cost- effective antireflection layer in the commercial solar cells market. The homogenous black silicon developed by excimer laser processing, as emphasised above, can be rapidly produced in large scale with high uniformity, which meets the requirements of modern solar cell industry. In chapter 7, black silicon has been introduced as the sunlight absorber in a novel solar thermal device, which is developed totally by cost effective amorphous silicon materials and rapid excimer laser processing. The structure also hints at the formation of p-i-n pillars, allowing a conventional thin film solar cell to benefit from the advantage of this absorbing structure.

4.4 Comparison with Black Copper (bCu)

In the Physics Department of the University of Dundee, Tang and Abdolvand have reported the laser micro-structuring of high purity Copper substrates, and the results showed that the surface is black, and comprises highly organized, periodic microstructures on the Cu target [156]. The laser system utilized in their work was a nanosecond pulsed Nd:YVO_4 with wavelength of 532 nm, average power of 10W, pulse length of 10 ns, repetition rage of 30 kHz and the laser energy fluence of ~2.5 J/cm^2. In the standard atmospheric environment, the Cu substrate was laser scanned with a laser beam of a Gaussian intensity profile, and a flat field scanning lens system was employed to focus on the target. The scanning technique adopted here is called cross hatching that scan over the surface of the Cu by both horizontal (x) and vertical (y) directions to form a grid pattern as shown in *figure 50*.

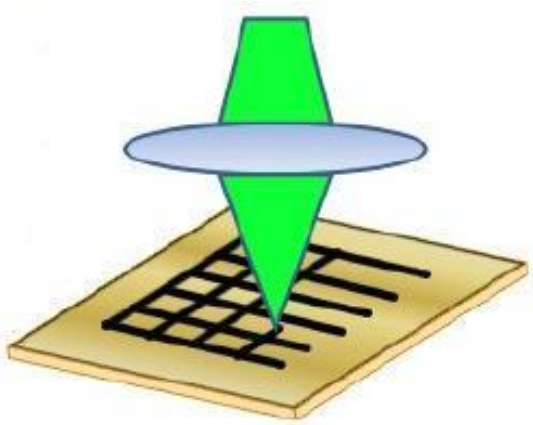

Figure 50: The cross-hatching regime where laser beam was scanned in both x and y directions, to form a grid pattern on Cu [156].

In *figure 50*, the images show the surface features of laser processed Cu, and from *figure 51 (a)*, black surface can be observed directly from different angles. The micro

pyramidal feature is formed, and the size of these micro pyramids depends on the laser fluence energy.

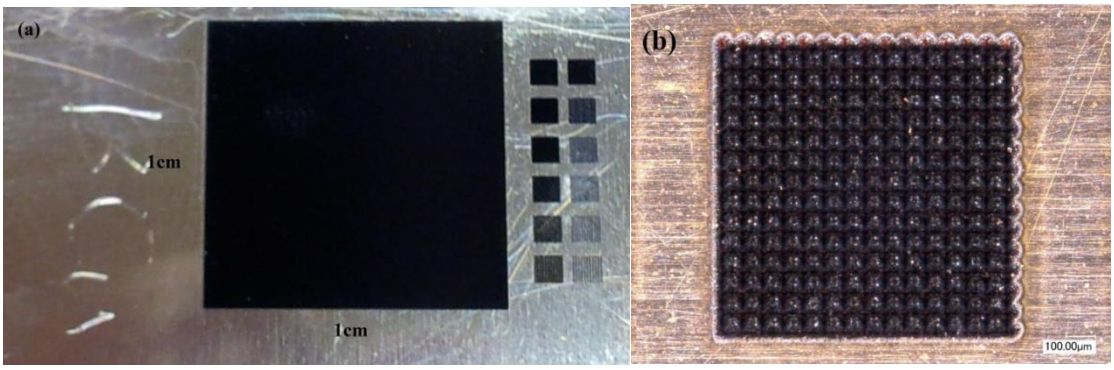

Figure 51: (a) Image of laser processed 1cm × 1cm black Cu. (b) Top close view of the surface of the Cu target after irradiation with laser fluence of 2.5 J/cm^2.

These excellent properties make bCu as an alternative candidate to replace bSi film for light absorber in a PV device. However, the cost for fabricating bCu is much higher than excimer laser fabricated bSi, and this is the premier consideration of industrial and commercial processes. For instance, growth of a 1 cm^2 bCu by the Nd:YVO_4 laser system costs around 40 minutes, which is much longer than 200 seconds of fabricating the same size of bSi by KrF excimer laser system.

Another advantage of the excimer laser technology in growing bSi film is the various choices of the base substrates, which includes cheap and flexible plastic substrate, which might attract attention in future.

4.5 Summary

In this chapter, the growth method of novel large area black silicon films were grown, and investigated the growth environment, condition, morphology and optical properties of the film. The bSi film was developed by the excimer laser processing technique which is fast and able to produce the film by large size.

The bSi film can be obtained by laser processing of thick a-Si:H on various substrates including metals, glass, silicon wafer or flexible ones such as polymer materials. The KrF excimer laser processing was employed in this work, and with shaping the beam to provide scanning methods called low energy as the leading edge, micro pillar-shape features were obtained. The optical measurement indicates that this homogeneous and high density material is highly absorbing with low reflecting. Furthermore, bSi is also relatively low cost, large scalable and simple to fabricate, which meet the requirements of modern industry. With these merits, bSi could be used in numbers of applications, and one of them is to be used for the sunlight absorber in our new solar thermal device. The cost effective and high purity thin copper foil substrate was selected as the finial device base as it has high thermal and electrical conductivity, which can transfer the trapped heat from one side black silicon film to the emitting layer on the other side. And also during the excimer laser processing, the Cu atom are diffused into the emitting material and created a tunnel for the electron transportation, resulting in enhancing the field and thermionic emission threshold field.

The bSi film with a structure of micro pillars will dramatically decrease the lights reflection, which has been noticed since discovery. As an anti-reflection material, moth-eye has a similar micro-structure as black silicon. As discussed previously, the moth-eye structure was designed via nature, and this structure can be obtained by using acid solution or multi-steps manufacturing only on silicon substrates, which is more expensive and complex than excimer laser processing technique, and this is also the main reason that the moth-eye structure has not been accepted by the modern solar cell industries.

At the end of this chapter, the laser processed Cu was also introduced, which was reported by the Physics Department of the University of Dundee, which could be an alternative candidate for sunlight absorber in the solar thermal device. The bCu material was developed by Nd:YVO_4 laser irradiating directly on high purity Cu sheets, and the optical measurements show that this black material is significant in absorbing visible light. A comparison between bCu and bSi was made, both of these materials have low reflectance to be great candidates for the light absorber applications. However, the cost and fabrication process of bCu is also much higher and more complicated than bSi, and difficult to be made in large scale applications. This disadvantage indicates that bCu still needs further investigation and improvements.

Overall, black silicon film fabricated by excimer laser processing is a relative rapid, cost-effective, able to develop on large size as well as on various cheap base substrates. These advantages make bSi as a promising material in light trapping applications, especially in sun lights absorbing. In this study, bSi film was adapted as the light absorber in the novel solar thermal device to enhance the heat absorbing and transferring.

5 Results and Discussion: Single Junction a-Si:H Nanowire Solar Cell

The previous Chapter described the formation of material across large area that has a surface morphology that allows near unity absorption of lights. The internal structure of the material will be exploited together with this absorber to make a solar thermal device and this is to be described in Chapter 8. However, this structure and absorption can be exploited to prepare nanowire or pillar solar devices, and this Chapter examines the possibility of exploiting the absorber nature of the material to prepare p-i-n pillar devices. This can easily be done by further deposition of p-i-n layers by conformal coating PECVD process. It would be commercially more attractive if doping could be carried out during the laser process itself. The amorphous silicon nanowire solar device is fabricated using the techniques of Excimer Laser Processing (ELP) as well as excimer laser doping technique.

The nanowire structure device is an alternative approval to the laser-fabricated solar thermionic energy device as it is demonstrated in the previous chapter that the excimer laser processing of certain thick a-Si can fabricate nano-wire (NW) or nano-rod (NR) structure which can be used as an efficient light absorber as well as give us an opportunity to develop a nanowire solar device. In this SC application, nanowires-array poly-Si are formed on the surface of a-Si:H films, using the same fabrication technique as the Black Silicon fabrication in the previous study. The advantage of this nanowire- array is to make it possible to greatly reduce reflection while increasing transmission and absorption. So, with this micro structure, an anti- reflection coating or textured surface materials normally coated on the top of the PV cells may be avoided. In the following chapter, two development methods of a-Si:H nanowire solar cells are discussed.

5.1 Fabrication of the n-i-p Substrate-type Device

In an a-Si:H solar cell, from the literature, the best thickness of i-type is 250nm and 10-15nm for p or n-type layer. However, in this research, the 250 nm thickness of the amorphous silicon is too thin to fabricate micro pillar structure by excimer laser process, so a thickness of 300nm of a-Si:H is then preferred to use. A schematic of n-i-p a-Si:H nanowire substrate-type solar cell is shown in *figure 52*. A 300nm a-Si:H layer was deposited on Al (150nm) sputtered Corning 2000 glass by conventional plasma- enhanced chemical vapour deposition (PECVD) technique at 220 ^{o}C with the 10W RF power, and the precursor gas SiH_4 was introduced to the chamber with flow rate of 75 sccm. For growth of 300 nm a-Si:H films, the operation time was set to 40 minutes with the chamber pressure maintained at 100 mTorr.

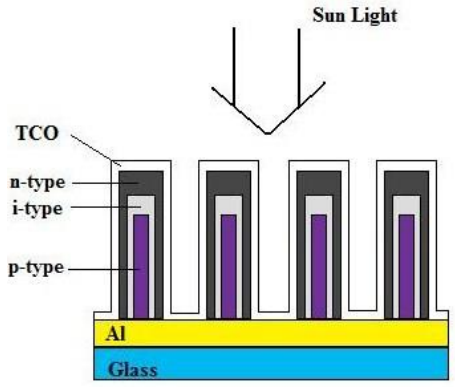

Figure 52: Schematic n-i-p structure a-Si:H nanowire cell.

To obtain a micro-pillar shape poly-Si bottom p-type layer, high frequency excimer laser was carried out on the surface of the a-Si:H film. The multi- pulse laser crystallization was carried out in air with the frequency of 50HZ, substrate scanning speed of 0.5mm/s with 160 mJ laser pulse energy at room temperature. Excimer laser annealing doped the bottom Al to Si to form p-type silicon while fabricates the Si nanowire array. To efficiently absorb sun light, a 300nm intrinsic a-Si:H film was then directly deposited on the previous laser treated a-Si:H film with deposition time of 60 minutes by PECVD. Then low

frequency excimer laser was then adopted to irradiate and dope the surface of the intrinsic a-Si:H with N_2 (pressure > 0.76 mTorr) to form a thin layer of n-type silicon. The multi-pulse excimer laser scan the a-Si:H with the frequency of 25HZ, substrate scanning speed of 2mm/s and the laser pulse energy of 120 mJ at room temperature in this case.

After developing the n-i-p structure, a layer of 300 nm transparent electrode - Indium Tin Oxide (ITO) film was deposited with the mask of area of 1cm × 1cm on the top of the p-i-n junction by conventional and well-developed RF sputtering technique in the Electrical and Electronic Engineering Department of the University of Cambridge. The ITO electrode also performs as the anti-reflection layer in PV devices that allows the minimum reflection of the sun lights.

5.2 Surface Morphology and Micro Structure of the n-i-p Suberstrate Junction

The laser pulse energy was varied from 120 to 180 mJ to irradiate the a-Si:H film. The laser energy density should be high enough to melt the a-Si:H film while granulating the surface but without damaging the films and underneath metal electrode. In our experiment, 160 mJ was finally adopted as the bottom Al back electrode cracked under the laser energy of 180 mJ while no sharp features observed under 140mJ.

The Si nanowires were fabricated by high frequency laser irradiation as shown in *figure 53*, the uniform poly-Si micro- pillars typically have about 1μm height and 150 nm in diameter with the average separation of 0.5- 0.8 μm.

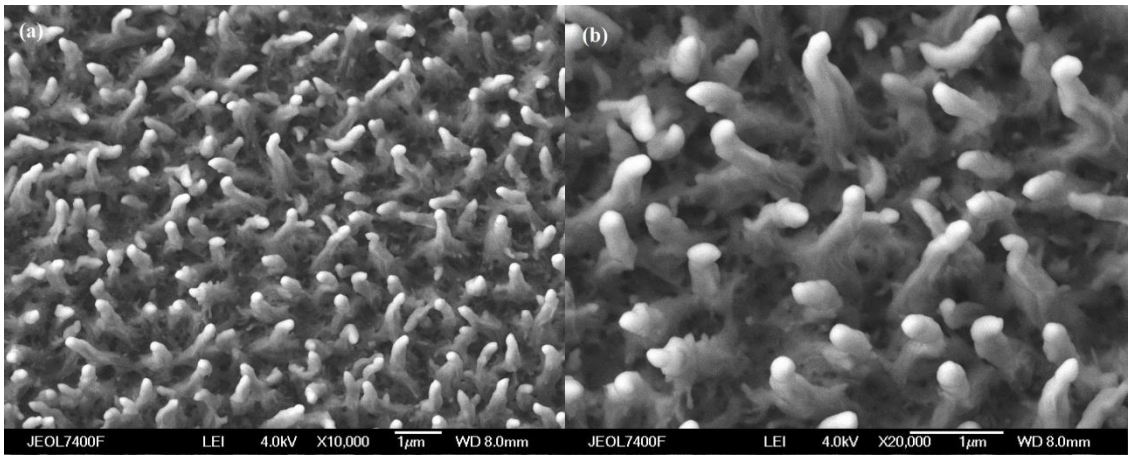

Figure 53: Scanning electron micrographs of high frequency and high energy excimer laser processed 300nm a-Si:H film. (a) overall view at an angle of 20^{o} to the surface normal, (b) close up view of the micro pillars.

In order to obtain a thin top layer of n- type Si, excimer laser treatment was carried on 400nm a-Si:H film (deposited on these poly-Si nanowires) in N_2 atmosphere. The low frequency laser processing doped the surface of the intrinsic a-Si:H film with N_2 to form a thin layer of n-type, as shown in *figure 54*. The laser treated a-Si:H film shows a different surface morphology from underlying micro pillar- shape. This is because an intrinsic a-Si:H film was coated on the p-type poly-Si by 400 nm, according to the gaps between pillars are just 500-800 nm from *figure 53*, so the overlapping is not avoidable. Another possible consideration is that during the second round deposition a-Si:H by PECVD, due to the deposition is alone the surface of 1μm- hight micro-pillar, the surface temperature is lower than the bottom substrate heater (220^{o}C). So, the uniformity is difficult to control so far.

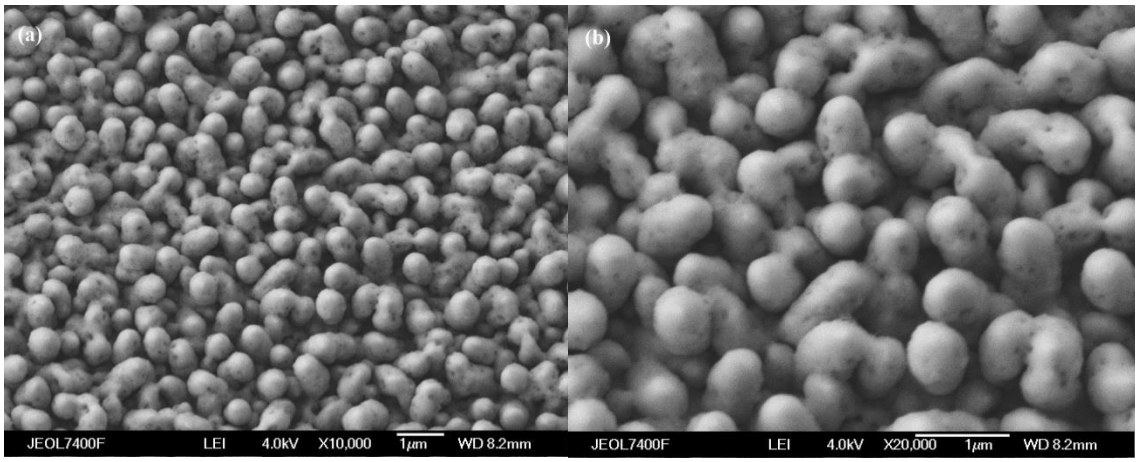

Figure 54: Scanning electron micrographs of low frequency and low energy excimer laser processed 400nm a-Si:H film in N_2. (b) overall view at an angle of 20^o to the surface normal, (b) close up view of the micro pillars

5.3 Optical and Electrical Measurements

Optical reflection measurements were done with JASCO V-670 Spectrophotometer. Current- Voltage (I-V) measurement of the cell was measured with Keithley 4200 semiconductor characterization system.

The goal of the optical reflection measurements is to identify how many photons the nano- pillar Si nanowire structure could absorb. In *figure 55*, the optical measurements were taken after the first and second excimer laser irradiation respectively by Cary 500 spectrometer. In the visible light region, wavelength 380- 740nm, the reflection of the first laser processed Si nanowire is averagely around 10%, with minimum 7% on 450nm and maximum 17.5% on 740 nm. The Si nanowire has a similar structure as the excimer laser processed black silicon (bSi, see Chapter 4.2). However, the reflection of the Si nanowire is higher than bSi. This is because of the thickness of the original a-Si:H films on metal coated corning glass, for Si nanowire structure is 300nm and for bSi application is 450nm. Another possible reason is the back metal, in this case, we adopted Al because of p-type doping requirement, and in the bSi fabrication, we mainly used Cu plate which could

transport heat faster than Al due to the nature of the metal's thermal conductivity. *Figure 54* also indicates the 2nd laser processed a-Si:H in an N_2 environment that in the visible light region, the reflection improved compared to the 1st laser processed for fabricating Si nanowire. The average reflection is around 6%, maximum 10% on 740nm and minimum 5.6% on 570nm.

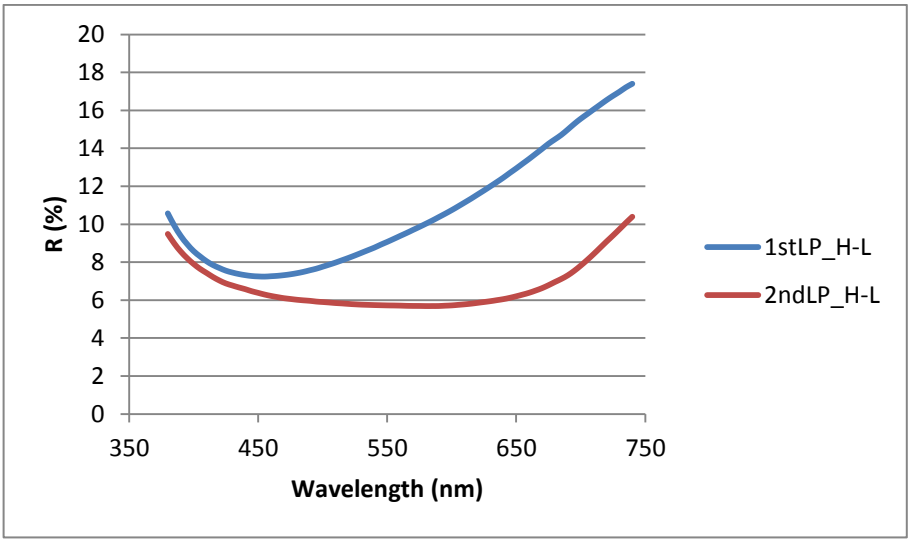

Figure 55: Reflection of the excimer laser processed a-Si:H film (including 1st and 2nd Laser processed) between wavelength 380- 740nm.

In this research, we also examined an alternative method of the semi-transparent top conductive electrode, ultrathin Chromium (Cr) layer, which has already been reported by Ghosh's group of its excellent electrical and optical properties [157]. The ultrathin Cr film of 2 nm is deposited by DC Sputtering on Corning Glass substrate, and according to Rajani et al., Cr films of thickness of 2nm should have an average transmittance of above 90% on the wavelength region of 350- 1000 nm [158]. The transmittance of the ultrathin Cr film obtained by DC sputtering was measured by UV-VIS spectrometer, and showed an average of 80% in the wavelength region of 350-1000 nm, shown in *figure 56.* The ultrathin Cr film

also showed a sheet resistance of 9.3×10^3 Ω/□ when it was deposited on planar substrate. However, in this case, the nanowire device with ultrathin Cr laser on the top did not show any light responses as well as the electrical connection, this is because that the 2 nm Cr is too thin to perform as the continues (semi)transparent conductive layer on a 2 μm nanowire feature.

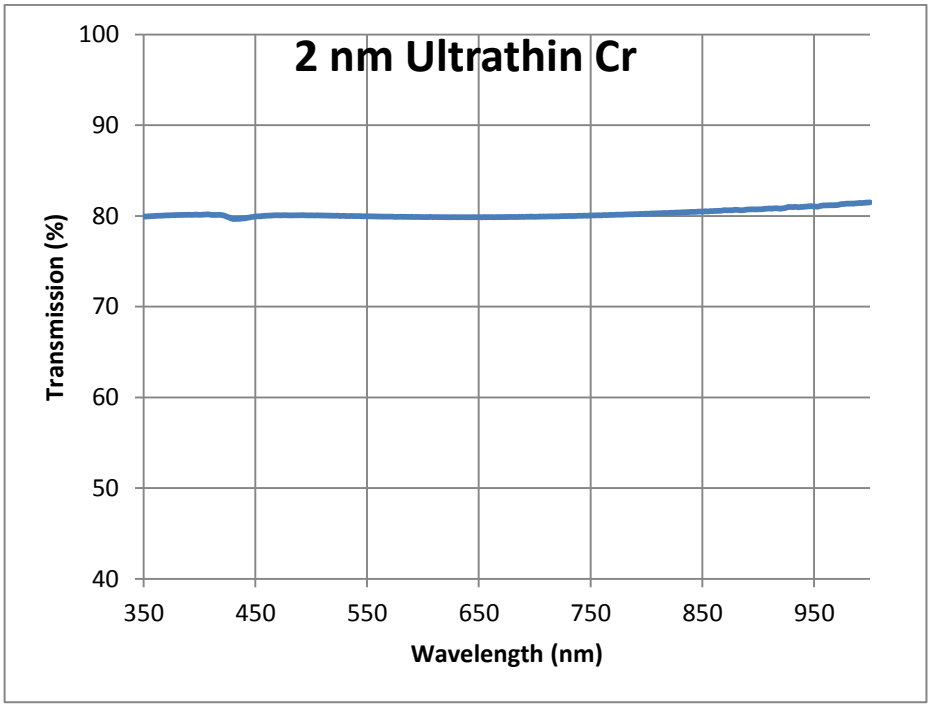

Figure 56: Transmission in the range of the wavelength of 350 nm to 1000 nm of ultrathin Cr film by DC sputtering.

With the top electrode – robust ITO film, the device was then examined under a Newport Solar Simulator, which can provide an AM 1.5 standard solar cell test and a total efficiency of 0.1 was calculated when we count the measurement area of 1 cm^2 (patterned ITO area). *Figure 57* is the plot of the original measurement data, followed by analysis (*figure 58*) the solar cell efficiency and fill factor calculations.

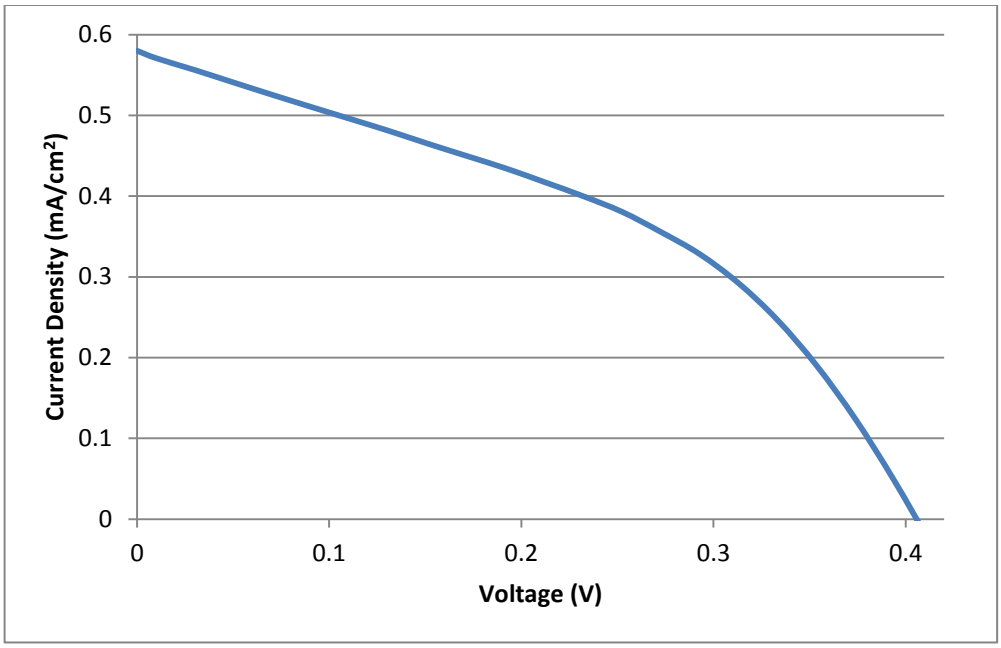

Figure 57: Solar cell performance by Newport solar simulator

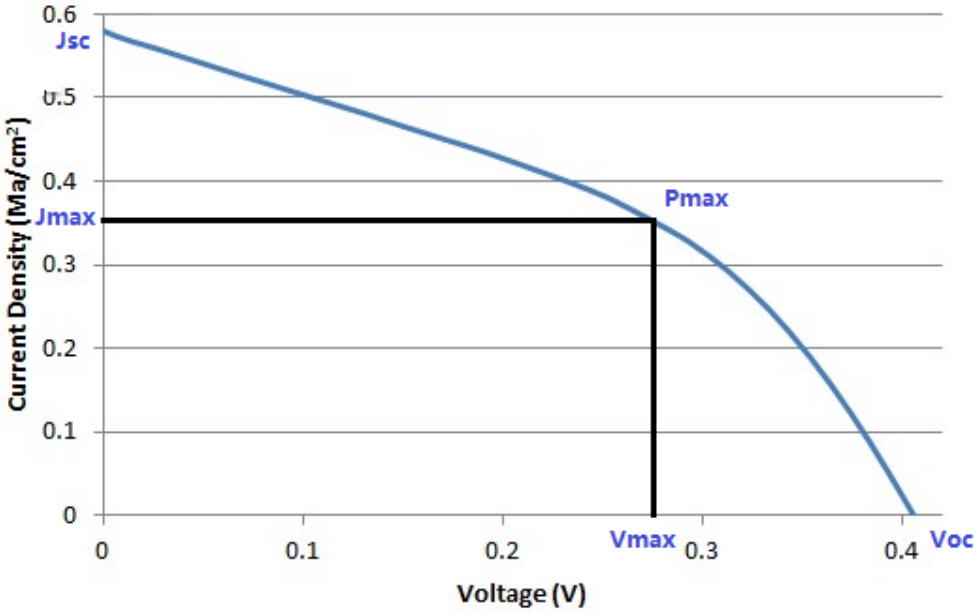

Figure 58: Jsc, Jmax, Pmax, Vmax and Voc marked in the original data for efficiency and fill factor calculation.

In figure 57, to calculate the fill factor and solar cell efficiency, several marks were added onto the original curve. In solar cell standard test conditions (STC, 298K with AM=1.5), P_{in} = 1000 W/m^2 = 100 mW/cm^2. The solar cell device fill factor and efficiency calculations were shown below:

$P_{max} = J_{max} \cdot V_{max}$ = 2.66 × 0.038 = 0.1011 mW/cm^2

Fill Factor (FF) = $\frac{P_{max}}{V_{oc} \cdot J_{sc}}$ = 0.1011 / (0.41 × 0.58) = 0.425 = 42.5%

$\eta = P_{max}/P_{in}$ = 0.1011 / 100 = 0.1%

This solar device did not give us a great on solar efficiency due to several reasons that the first is the thickness of the p and n type layers. In a classical p-i-n junction a-Si solar device, as introduced in Chapter 2.5, the p and n layers are around 10 – 15 nm. However, in this case the p type is difficult to be this thickness as a-Si layer has to be at least 250 nm to form a ~ 2 μm spike array during the excimer laser processing. The second reason can be the excimer laser doping both in p and n type layers. To examine whether the intrinsic as-deposited a-Si was doped with nitrogen and aluminium, a thermopower study was carried out.

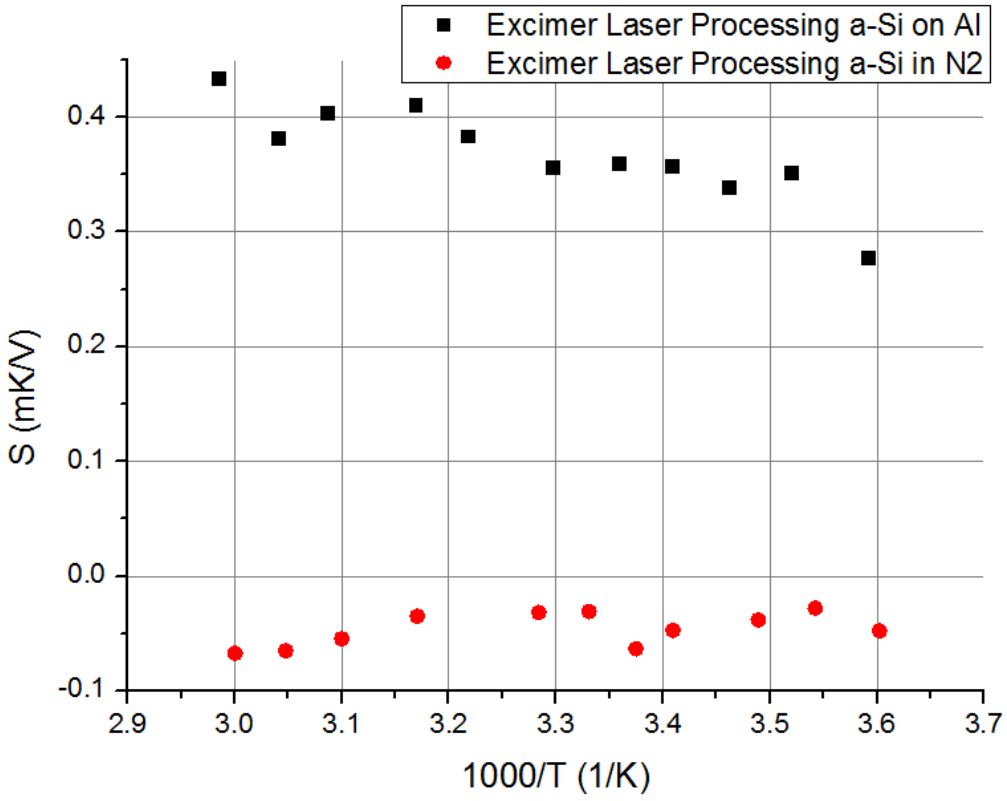

Figure 59: Thermopower measurements of a-Si film excimer laser processing on Al and in N_2.

It is obvious from *figure 59* that the excimer laser processed a-Si on Al film presents a p-type behaviour as the thermopower value is positive while a negative value was obtained on the excimer laser processed a-Si in nitrogen surrounding. However, the average value of -0.05 mV/K of the excimer laser processing in N_2 indicated that the dosage of N is weak in the a-Si film so that could not form a good p-i-n junction. In our experiment, the excimer laser processed a-Si using relative low energy so that not to damage the features from the previous formed nanowires, and the laser process was carried in a N_2 filled chamber with continuous introducing N_2 with the gas out valve open. There is still a chance that other gases or elements can go back to the processing chamber. Other methods of excimer laser doping in the future are worth to try, such as ELP in ammonia (NH_3) solution, etc.

5.4 Summary

In this chapter, we presented the work of fabricating a novel Si nanowire solar device with excimer laser technique both in n-i-p and p-i-n structure. During the previous chapter, we have introduced the original method to fabricate high aperture nanowires array with 1μm height and diameter of 150-200 nm by KrF excimer laser processed a-Si:H film as the light absorber in thermal PV device. This technique is adopted in this work to form the Si nanowire array, and we also employed the excimer laser process to dope with Al and N_2 to form p and n type layers. With the nanowire structure, an anti-reflection layer can be avoided so that the cost can be controlled and the development process is simplified. With these techniques, we fabricated both substrate-type and superstrate-type solar devices, and measure the reflection in the regime of visible lights.

The efficiency of the n-i-p substrate type device was measured as 0.1%, which was not a remarkable result in solar cell industries. However, it was demonstrated that the excimer laser processing can be used in fabricating silicon nanowires and be adapted in PV cells. Improvements such as controlling of thickness of p and n layers, interface optimizing and device structure design can enhance the device performance. In the chapter of future work, these will be introduced.

6 Field Emission and Thermionic Emission Properties of ELP Amorphous Silicon and Carbon Nanotubes (CNTs)

In this chapter, the field emission and thermionic emission properties of excimer laser processed a-Si:H thin film are investigated. They were compared to carbon nanotube materials. Different from the 'black silicon' in Chapter 4, the a-Si:H based field/thermionic emitters were prepared under low energy and low scanning speed conditions of the excimer laser as well as using thinner a-Si precursor film. Two growth methods of CNTs, Electrophoretic Deposition method (EPD) and Chemical Vapor Deposition (CVD) are studied, as well as research on the surface morphology and microstructure of CNTs and a-Si:H thin film by laser irradiation are discussed.

6.1 Excimer Laser Processed Amorphous Silicon as Field/Thermionic Emission Cathode Material

In the previous chapter, silicon nanowire solar devices developed by excimer laser processing were introduced. As a parallel study of the renewable energy by the promising excimer laser processing, a novel solar thermal device is investigated which has a similar concept to the PETE device that was introduced in Chapter 2.5.4, however with different emitting materials. From a commercial consideration, the candidate cathode materials should be cost effective, fast develop and easy for scaling up.

In theory, the TE emitters should have excellent ability to emit electrons when the cathode temperature increases. Furthermore, the higher the temperature goes the much more electrons are emitted. In our study, we have investigated the amorphous silicon based material on various metal coated glass substrates with our core technique – excimer laser processing as the cathode candidate. The ELP a-Si array has been reported with good results on field emission by our group, and in this chapter, a study of thermionic emission property will be presented.

The field and thermionic emission of bSi films were also examined initially, however, due to the geometry and oxygen level in the bSi film, the threshold field are quite high, upto 35 V/μm. This made bSi film not to be a proper candidate as the emitting material.

This study on field emission and thermionic emission is the foundation of the novel photon enhanced solar thermal device which will be discussed in Chapter 7. And the development procedure of the cathode layer was kept same between field emission and thermionic emission.

6.1.1 Substrate Preparation

The whole fabrication processes took place in Class 1000 semiconductor cleanroom. Prior to the coating of back metals, base **Corning** 7039 glass substrates are cleaned through standard semiconductor cleanroom procedure as shown in *figure 60*.

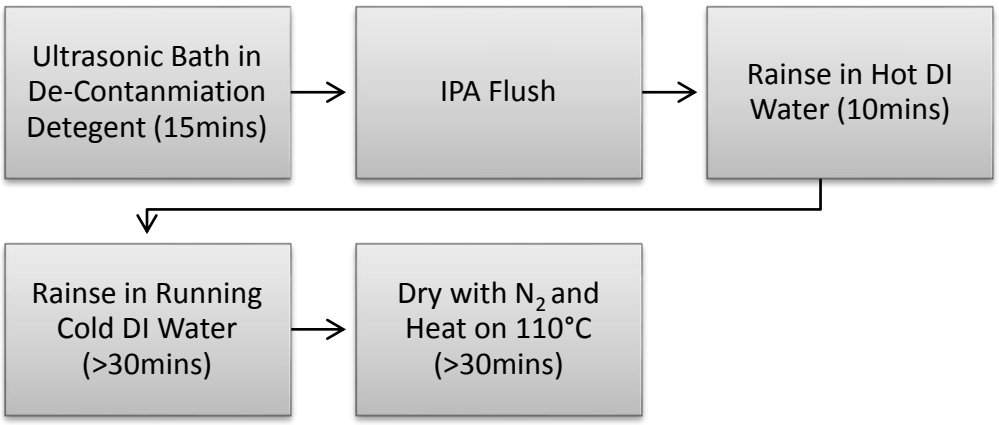

Figure 60: Flow chart of cleanroom standard of cleaning glass based substrates.

The glass substrates were then mounted on the rotatable sample holder of the DC Sputtering system for back contact deposition after cooling down the glass substrates across the cleaning procedure. The metal target was selected and mounted as shown in the system configuration in *figure 60*. Common targets, such as Al, Cu, Cr and Mo used in the PhD study are listed below.

Layer	Target Material	Density	Z-Value
1	Aluminum (Al)	2.70	8.17
2	Copper (Cu)	8.93	20.20
3	Chromium (Cr)	7.20	28.95
4	Molybdenum (Mo)	10.20	34.34

Table 6: Frequently-used targets of DC Sputtering System

The Z-Value listed in *Table 6* is also known as acoustic impedance, which is density × longitudinal velocity of sound (with a numerical factor). When the Z value is compared

to that of quartz (the piezoelectric material used as basis of deposition rate monitoring) it is quoted as 'Z-ratio'. Z-ratio of the material is used to correct the signal when the quartz crystal sensor is used to detect deposition rate and film thickness [159].

When pumping down to ~10^{-6} mbar, the deposition was to start. The whole deposition process under the flow rate of 10 sccm of Argon gas, and after applying the voltage and current, the positive Ar ions which have high enough energy are accelerated to bombard the sputtering targets on the cathode side (sputtering target), and to free the atoms or molecules from the target to the all directions. 100 nm thickness of the back contact was pre-set in the system, and the Sputtering will stop automatically when the thickness of the film reaches the pre-set value through the thickness sensor. One 100 nm thick Al layer will take around 8 minutes and 20 second as the deposition rate is steady at 0.2 nm per second with the typical working pressure of ~ 3×10^{-3} mbar. After venting the chamber with introducing N_2 and reach the atmosphere, metal coated glass substrates are collected and ready to be used for next step.

The deposition process of the a-Si layer is exactly the same as the sample preparation of precursor film for growing ‘black silicon’ discussed in Chapter 4.1 except that processing time was different due to purposed the thickness. To fabricate a 100 nm thick a-Si layer, the processing time was around 12 and half minutes through the PECVD system setting an RF power of 10 Watts with the precursor gas SiH_4 at flow rate of 75 sccm. The substrates were kept at 220 ^{o}C and the deposition chamber pressure which was maintained at 100 mTorr. The thickness of the film can be easily confirmed by the *Delta* stylus profilemeter.

To develop a microstructured a-Si based emitter array, the excimer laser crystallization was applied to the surface of the a-Si:H film under normal atmospheric conditions at room temperature. The laser system used in this study was an LPX*pro*210(F) KrF excimer laser with 248 nm wavelength and 20 ns pulse duration. *Figure 29 and 30* illustrated the laser beam slope which differs from the fabrication of black silicon, in the fabrication of field emission and thermionic emission emitters, low frequency, low laser energy and faster sample scanning speed were applied with a scanning –X direction, which

is also known as high laser energy as the leading edge, and it is different from the excimer laser fabricating in bSi film. When the sample was scanned in the low energy as the leading edge in relative to the laser beam profile, the a-Si:H thin film will subject to an irradiation with the laser fluence slowly and gradually increases until it reaches the maximum power, and then the fluence rapidly reduces to zero. In contrast, if the sample was scanned by high energy as the leading edge, the irradiated area on the a-Si:H thin film surface will see an abrupt increase in laser fluence and the fluence quickly arrives at its maximum and then gradually and slowly reduces to the zero [136]. As discussed previously, the high laser energy as the leading edge processing profile can bring a shaper micro conical shape which is benefit for the field emission application and this was confirmed by the previous experience of Fan et al [97].

6.1.2 Surface Morphology of ELP a-Si Films

The SEM images in *figure 61* illuminated the surface morphology of the excimer laser processed thin a-Si film on Al coated Corning eagle 2000 glass. With the laser pulse energy of 70 mJ, scanning speed of 2 mm/s with laser pulse of 400 per unit area on the sample, the micro conical structure of the a-Si was observed. Different from the black silicon micro spikes or pillars, the heights of the a-Si features in this case are just around 200 nm, this is because of the thickness of the precursor film and excimer laser processing parameters. In this study, the focus is on the geometric enhanced field emitters by excimer laser crystallization [35] and not damages the amorphous silicon film as well as the bottom substrates.

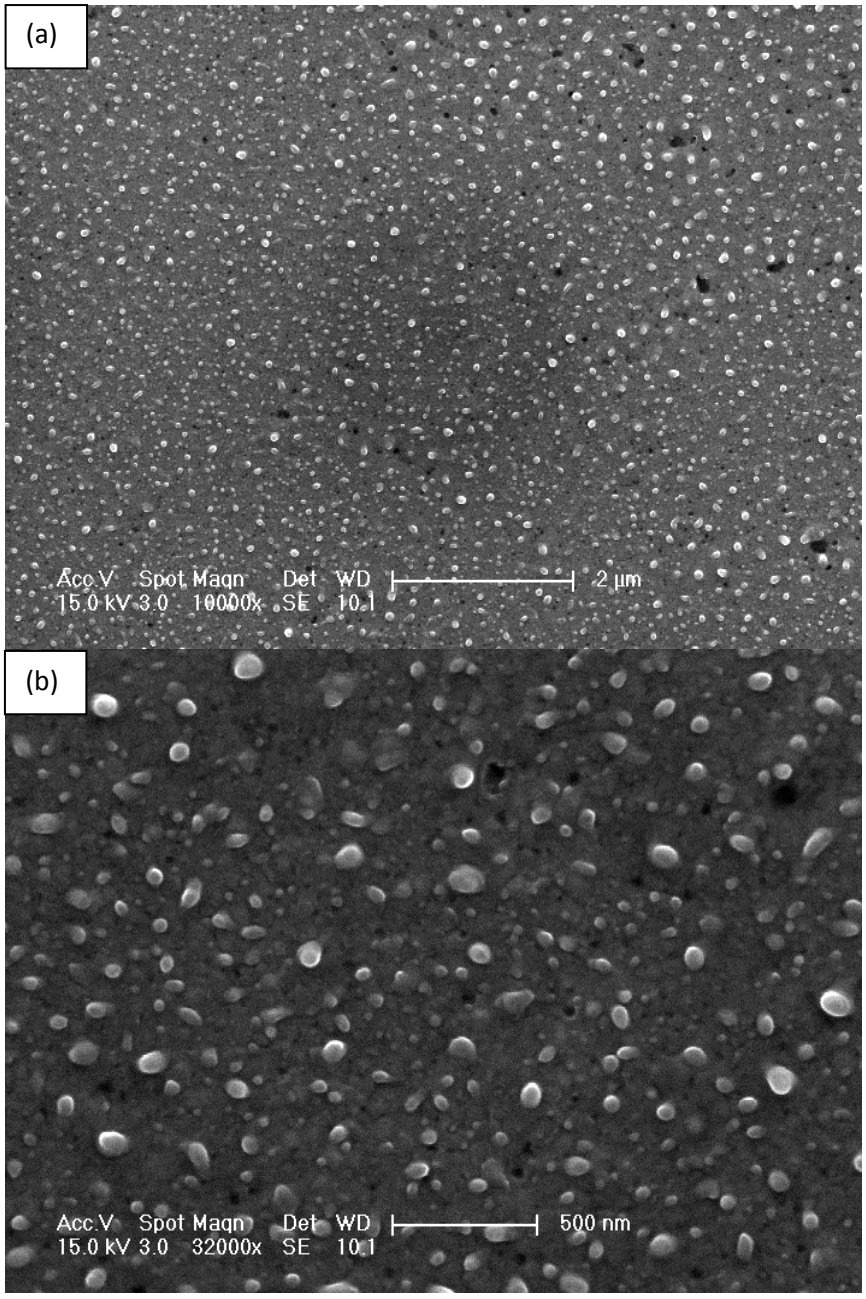
(a)
Acc.V Spot Magn Det WD 2 µm
15.0 kV 3.0 10000x SE 10.1
(b)
Acc.V Spot Magn Det WD 500 nm
15.0 kV 3.0 32000x SE 10.1

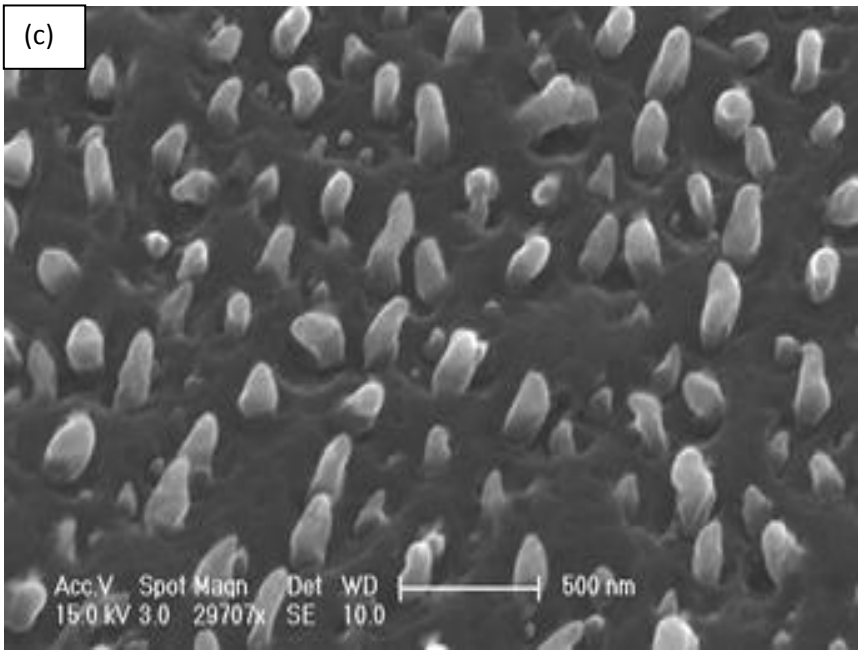

Figure 61: SEM image of (a) and (b) top view of ELP a-Si thin film on Al substrate, and (c) 45 degree titled view of ELP a-Si as field emitters.

6.2 Synthesis of CNT thin-film as Field/Thermionic Emission Cathode Material

6.2.1 Electrophoretic Deposition Method (EPD) for the Growth of CNTs

As discussed in Chapter 2.4.2, CNTs are a promising candidate material for cold cathode electron field emitters since its identification. CNTs are capable of emitting high currents at low fields, and also with chemical inertness, tensile strength, high electrical stability and aspect ratio as well.

In this study, CNTs were firstly deposited by the EPD method, which is considered a cost effective, quick, simple and efficient way to produce large CNT films with high homogeneity and proper surface roughness [160]. In the experimental equipment shown in

figure 62, the cathode is conductive ITO coated glass while the anode was a piece of Cu plate. A DC power resource connects the cathode and anode, and can supply electrical fields to support the CNTs deposition. The container in these experiments was a beaker, which is cheap and common, moreover, it is transparent that allow the users to observe the progress during the deposition of CNTs. The precursor liquid used in this application was CNT powders (purchased) in acetone, and the beaker placed onto a magnetic stirrer, which keeps the solvent uniformity during the deposition.

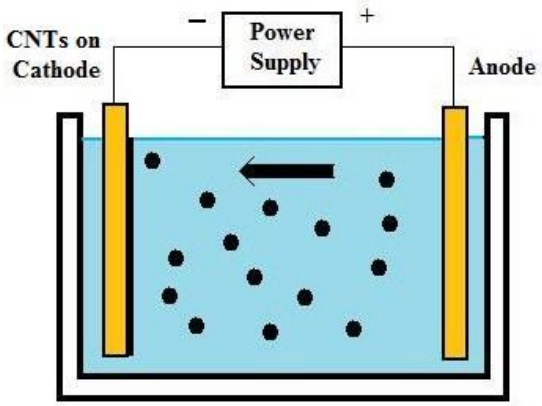

Fig 62: Schematic of EPD method for deposition of CNTs.

Applying a DC voltage of 60 V with a processing time of 10 minutes, a thickness of 2 μm CNTs film was obtained. After that, the substrate is rinsed by IsoPhthalic (IPA), and then placed onto a heater at 50 ^{o}C for 30 minutes to remove the water wafer properly.

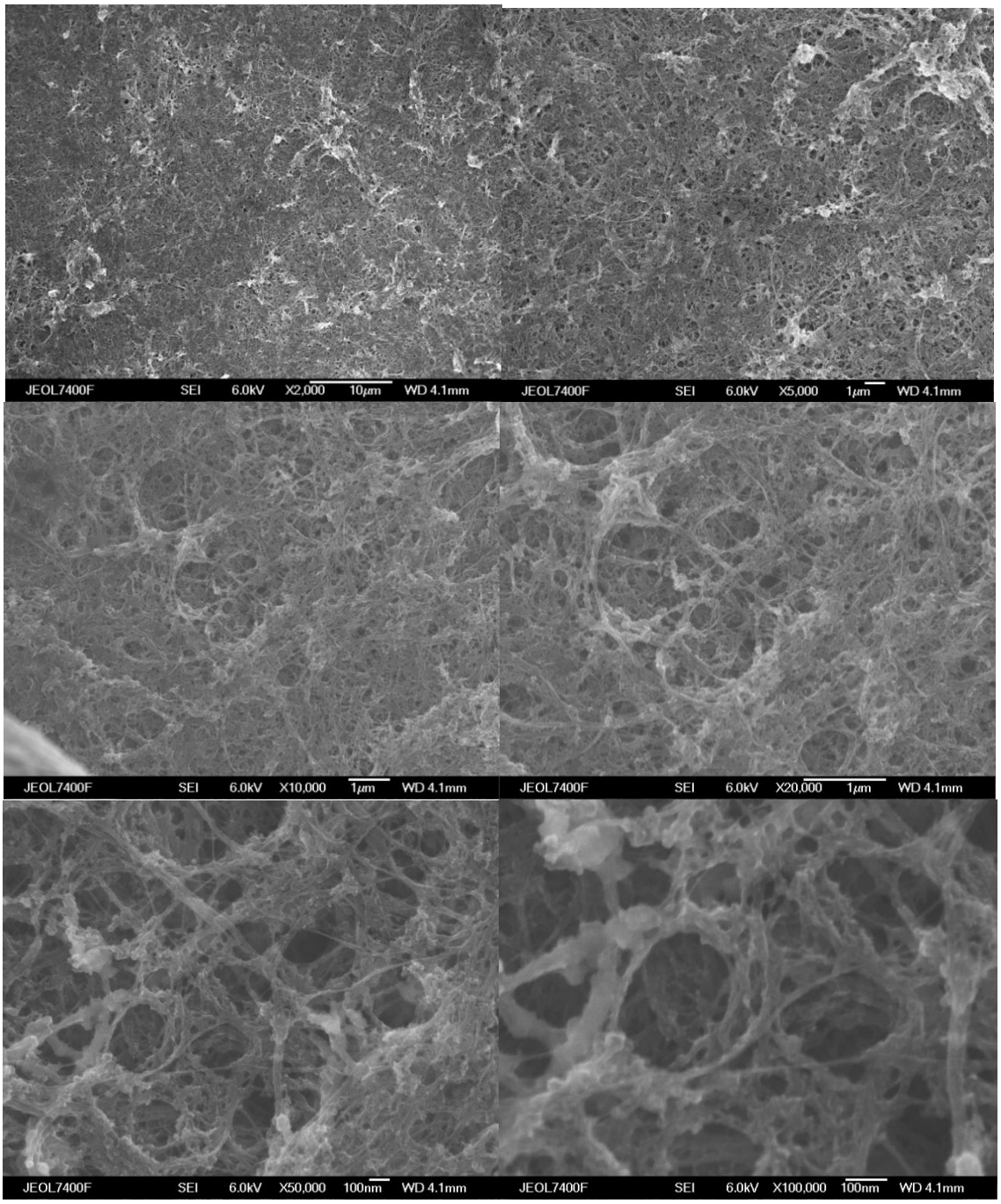

Figure 63: SEM images of CNTs on ITO coated substrate by EPD growing method.

In *figure 63*, diameter of ~10 nm and length of ~300 nm nanotubes can be observed. The film was very dense due to a 10 minutes processing time with a growing rate of 200

nm per minute. During our research, in order to develop a uniform CNTs layer as the field emission emitters and obtain an accurate field and thermionic emission test, longer processing time was selected to make sure the CNTs were covered on the substrate with no pin holes.

6.2.2 PECVD System for the Growth of CNTs

The PECVD system has basically four units such as the temperature control unit, gas flow control unit, vacuum and pressure control unit and plasma control unit (in *figure 16*). Carbon nanotube films in this research were also developed by PECVD system, which uses a relatively low temperature and has a similar principle and structure to the system for growing a-Si:H thin film (discussed in Chapter 3.1.2) except for the plasma control unit. The purification rate of PECVD is better than other growth systems but the only problem associated with using this technique is that mostly the nanotubes grown are multi-walled carbon nanotube (MWCNT).

The new PECVD system used for the growth of CNTs in this research was designed and developed by Q. Goher and S. Antony in Advanced Material Group, and this system was optimized for growth of CNTs and modified for graphene. The goal of the system was also to develop novel integrated carbon and silicon structures for renewable energy applications. This required careful design and optimization of the system for carbon nanotube growth.

To grow CNTs by the modified PECVD system, a thin catalyst layer is essential to coat on metal coated glass or silicon wafer substrates. The metal layer performs as the electrode in field or thermionic emission as well as the support layer in CNTs growth. The metal used here is tantalum (Ta). Different metal catalysts were selected, and they were: nickel (Ni), iron (Fe), Ni-chrome and nickel-iron (Ni-Fe) alloy. In the substrate preparation, DC sputtering was adapted to deposit a very thin of Ni catalyst layer (~4 nm) at a base pressure of 3.0×10^{-5} torr and the other three catalysts layers were deposited by thermal evaporation technique. In this study, we focused on using the most successful CNTs

growing catalyst material – nickel. The study of growing CNTs with Ta, Fe and Ni- Fe alloy can be found in Q. Goher's PhD thesis [161].

Substrates were cleaned with decontaminate detegent, washed in de-ionized (DI) water and dried by N_2 gas, prior to loading the substrates into the sample holder of the PECVD chamber. After proper cleaning, the substrate was then mounted onto the ceramic heater, and allocated at the grounded electrode of the R.F power supply. In the first place, the substrate was heated to grow nanoparticles and after that the R.F plasma was then used to refine sphericity of the nanoparticles. The total reaction time was around five minutes in 180 watts plasma at a processing temperature of around 500°C.

The CNTs growing was examined by the Philips XL30 scanning electron microscope (SEM) with an accelerating voltage of 15 KeV. Further analysis and imaging was performed using a 5kV electron beam in a JEOL 7400F series high resolution SEM (HRSEM), with an Oxford EDX compositional analysis system. The features of interest were observed in both SEI (secondary electrons image) and BEI (back-scattering image) detector modes.

A 20 nm Ta was first deposited on the silicon wafer by thermal evaporation and followed by a sputtered 4 nm Ni thin film. The *figure 64* illustrates the surface of substrate after the CNTs growth of nanotubes. During this five minutes' growing process, straight and long nanotubes were grown on the Ta buffer layer. The diameter of a single tube was in the range of 25nm to 35nm with a height of about 8 μm.

In these CNTs growing experiments, it was observed that a support layer is very important and essential, and SiO_2 is not enough to prevent the interaction of amorphous carbon on the surface. It was also observed that the combination of a support layer of Ta and catalyst layer of Ti was very promising to grow a fine quality of nanotubes.

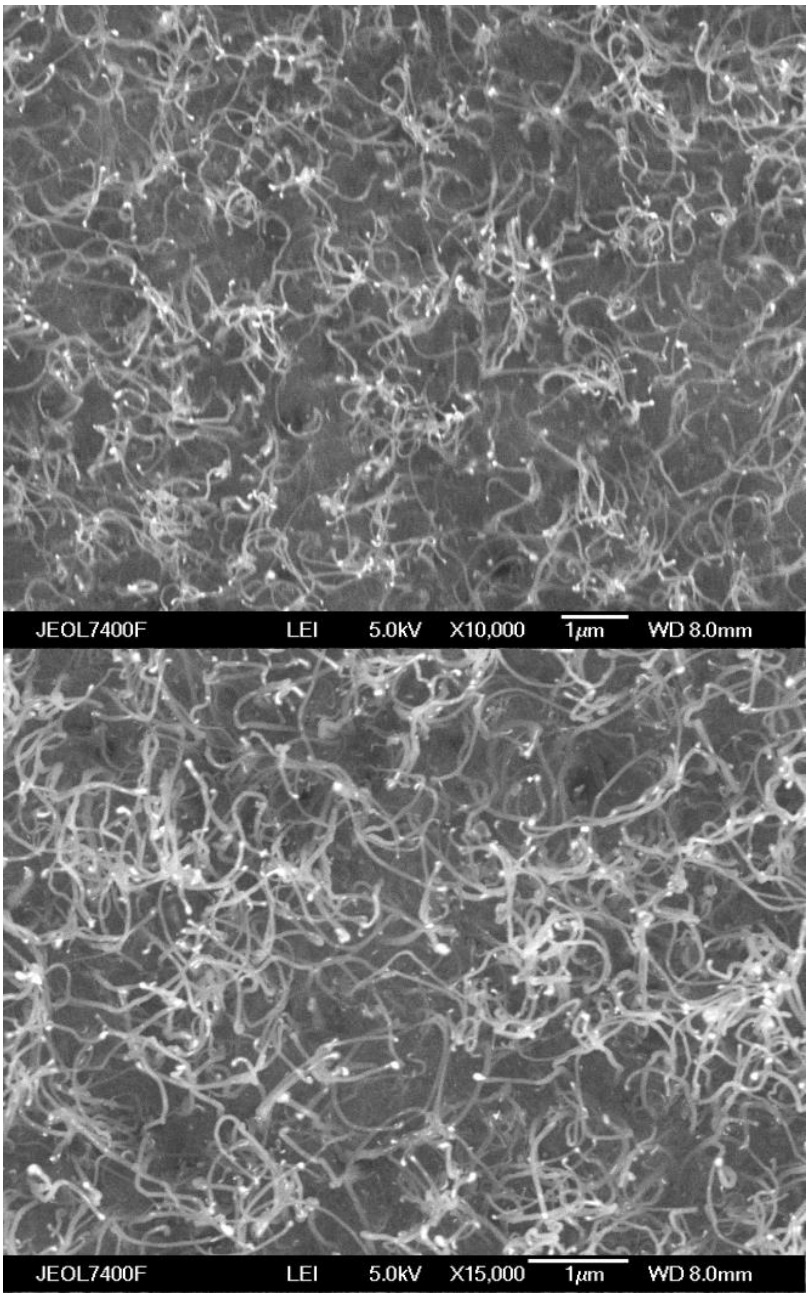

Figure 64: SEM images of carbon nanotubes grown by CVD method using Ni catalyst (upper image is at 10,000 X and lower one is at 15,000 X on right).

6.3 Electron Field Emission Measurements

This section presents the results of electron field emission characterizations of both ELP a-Si film and CNTs with using probe- type field emission measurement kit. The gap distance between cathode (substrates) and anode (probe) ranged from 0 to 5 cm, and for easy calculation, a reasonable 100 μm was set and used in these experiments and a maximum 3500 V could be applied to the cathode through a Keithley 248 High Voltage Supply. To examine the I-V curves, we concluded that the field emission threshold (E_{th}) will be counted when a 1 nA electron anode current was obtained.

The representative field emission characteristics of the laser microstructured a-Si:H films are presented in *figure 65*. The I-V curves shown in Fig.5a were obtained with an anode-cathode gap distance of 100 μm and the supplied anode voltage up to 3000 V. By examining the I-V curves, it is concluded that the field emission threshold E_{th} for 1 nA electron current emission was less than 12 V/μm and the saturation current up to 35 micro-amperes.

6.3.1 ELP a-Si Emitters

The field emission measurements were taken from ELP a-Si emitters on Mo back contacts. It showed a promising result as the threshold field is 11.5 V/μm with the maximum emission current at 0.04 mA when applying 1700 Volts.

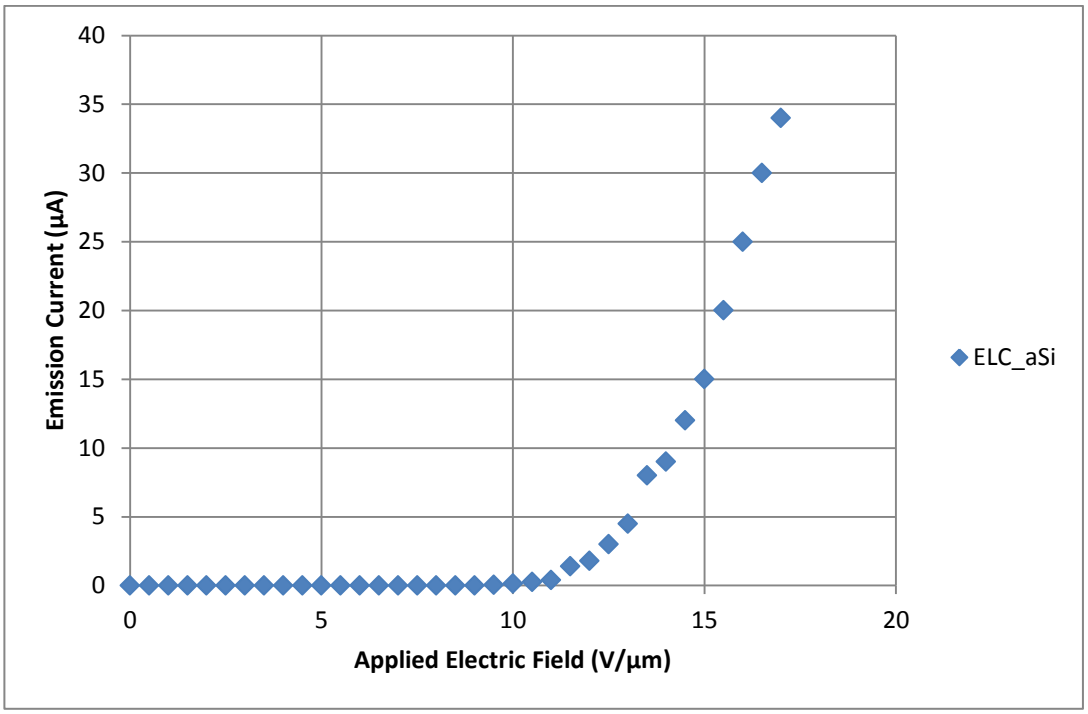

Figure 65: Emission current versus applied field of ELP aSi films

6.3.2 CNTs Emitters

As discussed in Chapter 2.4, CNTs possess excellent field emission property and have been considered as the most promising materials for field emission display technology. From *figure 65*, the field emission measurement of CNT film by EPD method is revealed. The turn- on field is 5 V/µm with maximum emission current of 0.08 mA when applying 770 Volts (*figure 66*). Compared to the results of a-Si, the CNT film show much lower threshold field and can generate greater anode currents, which follows the literature reviews [51, 52, 99, 162].

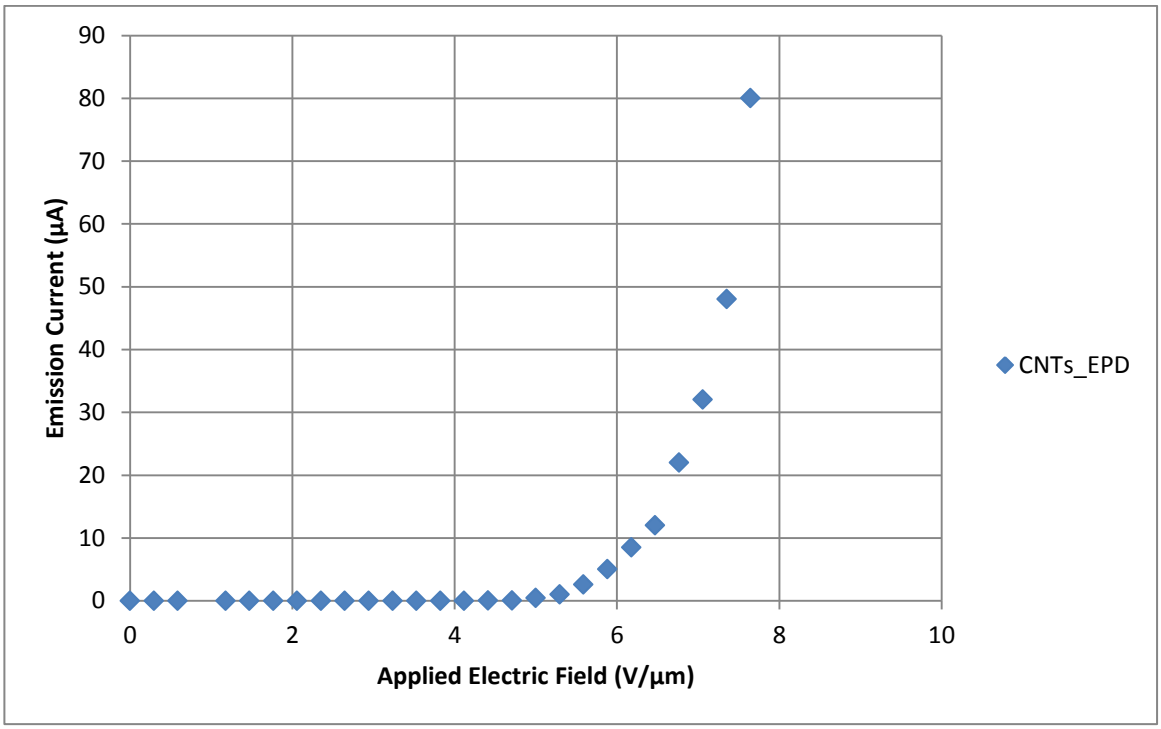

Figure 66: Emission current versus applied field of CNTs

The property of field emission from CNTs grown by CVD method was also investigated, and a comparison among ELP aSi, CNTs by CVD method and CNTs by EPD method is presented in *figure 67*.

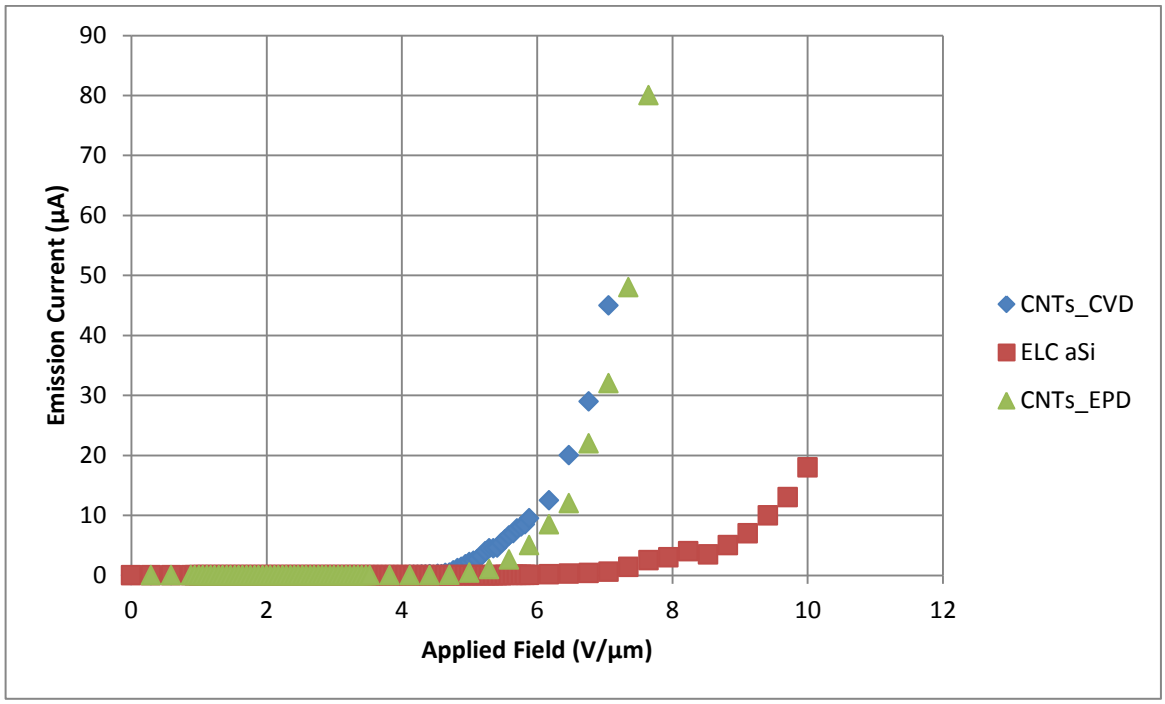

Figure 67: Emission current versus applied field of CNTs and ELP aSi films.

From the figure above, it is obvious that the field emission property of CNT films is better than that of ELP a-Si. Furthermore, CNTs by CVD method has a similar field emission performance as the CNTs by EPD method. The threshold field of CNTs by CVD is slightly lower than that of CNTs by EPD. However, the emission current of CNTs by EPD is double that of the CVD method when applying 770 Volts. This is probably because the CNTs by EPD are more uniform and dense than the film grown by CVD method, and the measurement area was around 0.8 cm^2 which is a relatively large area compared to the micro scale of the CNTs that cause the uneven nature of the electron emission and collection. Overall, from this measurement, it can be concluded that ELP a-Si material has a good prospect of field emission and can be improved by some techniques in the near future. CNTs have significant field emission ability and with benign growing conditions, it can reach the threshold field less than 2 V/µm.

6.4 Electron Thermionic Emission Measurements

This section explores the thermionic emission properties of CNTs and ELP a-Si films, as this measurement is the foundation of the photon enhanced solar thermal device. The measurement chamber, as introduced in Chapter 3.3.5, was modified from the field emission measurement chamber. A vacuum compatible heater was mounted in the chamber that allows applying maximum 700 K to the surface of samples. Peelable mica films (170 μm) act as the spacers between cathode and anode due to its high temperature resistance as well as acting as an electrical insulator.

A substrate holder was designed to mount onto the heater and also could fix the cathode, spacer and anode shown in *figure 68* below. To obtain measurement and prevent electrical short, mica films were also placed between the sample holder and anode as well as the sample holder and cathode (target sample). The design of the sample holder also embeds the thermocouples to measure the cathode temperature precisely.

Mica films in this project are p-type Mica which is an electrical insulator, and working temperature is up to 1000K. The color of p-type mica film is yellowish and shows a transparent behavior. In this case, the electrical and thermal insulating are the properties concerned.

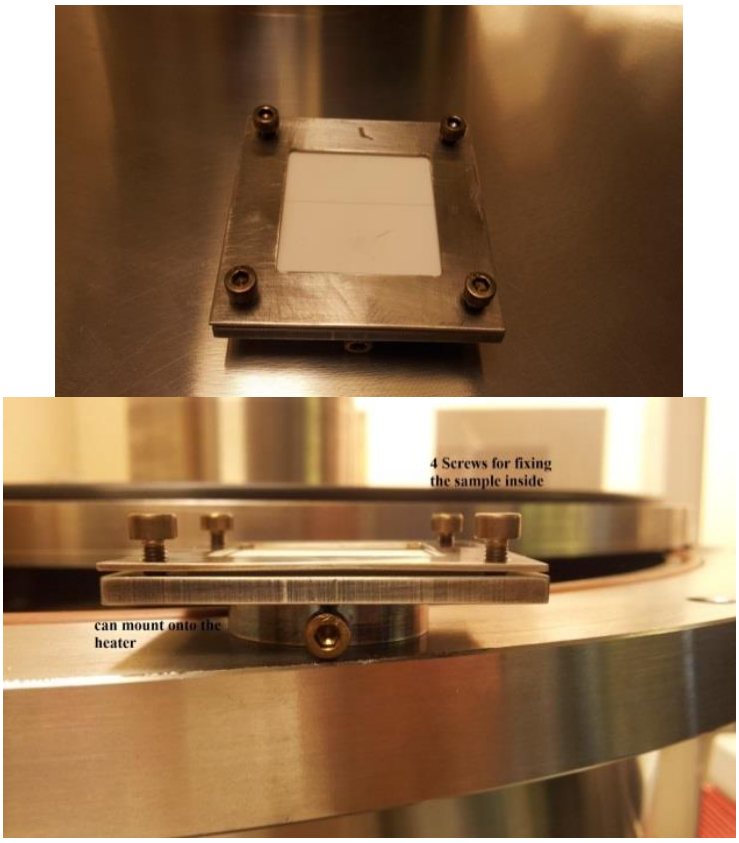

Figure 68: Top and side view of the stainless steel sample holder designed for thermionic emission measurement

As the measurement chamber was modified from the field emission measurement chamber, the power supply, temperature measurements (by thermocouples) and pumping system were kept. Different from the original field emission measurement, when achieving 10^{-6} Torr pressure, the heater was switched on at 100°C for half hour. An obvious decrease of the vacuum was observed due to the outgassing from the gaps inside of the sample holder. This action needed to be repeated a number of times to well degas the sample together with the sample holder, and help to obtain an accurate thermionic emission measurement.

6.4.1 ELP a-Si Emitters

Figure 69 below investigates the thermionic emission of ELP a-Si samples. Temperatures were recognized from the reading of the voltage meter and then converted from a thermocouple sensitivity chart. Having reached the desired temperature, an extra 30 minutes was taken to stabilize the temperature of the sample surface before the start of the thermionic emission measurements.

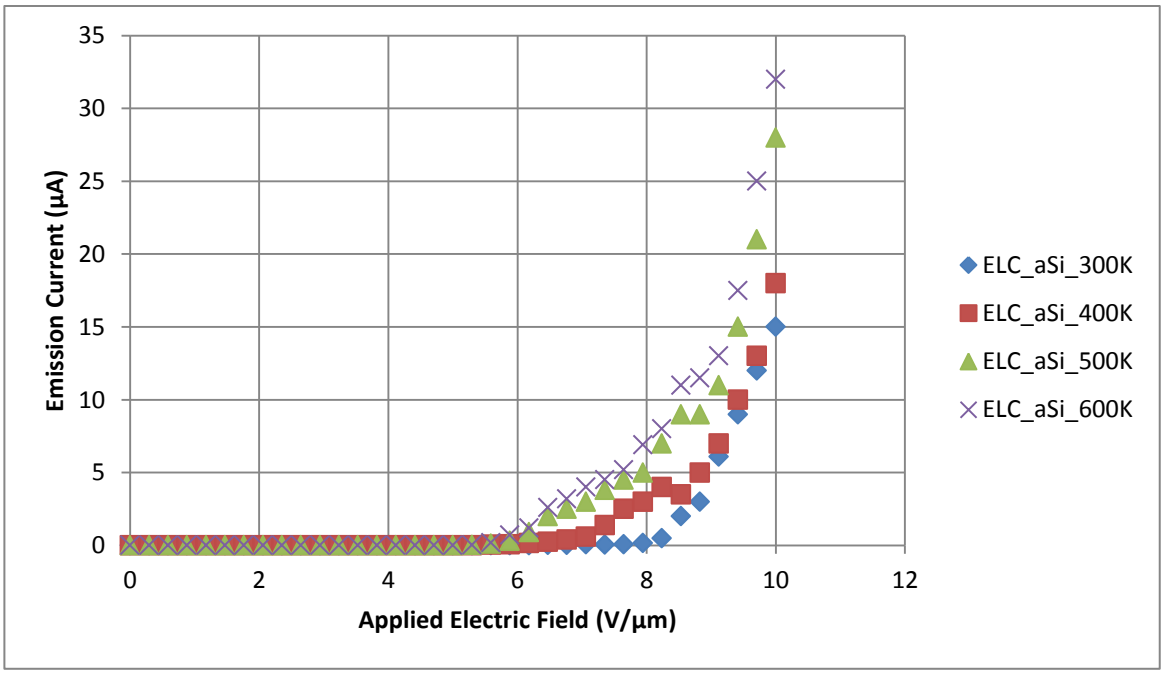

Figure 69: Thermionic emission curves of ELP a-Si films at 300K, 400K, 500K and 600K.

The threshold field of the measurement area became lower as the temperature increases while the emission current increases. Compare the curves of ELP_aSi_300K and EL_aSi_600K, the threshold field decreases from 8 V/μm to 5.7 V/μm while the emission current increases from 20 μA to 37 μA, nearly doubled. The ELP a-Si film shall reach much lower threshold voltage and higher emission current with increasing higher

temperature, however, due to the limit of the power supply of the heater, the temperature cannot go further higher. This will be the further work of the investigation of thermionic emission of ELP a-Si on high temperature (>600 K).

6.4.2 CNTs Emitters

From the previous section and literatures, CNTs act as a promising candidate of field emission emitters. In this part of the project, a study of thermionic emission of CNTs is presented and all the reference CNT samples in this experiment were deposited by the EPD technique on ITO coated glass.

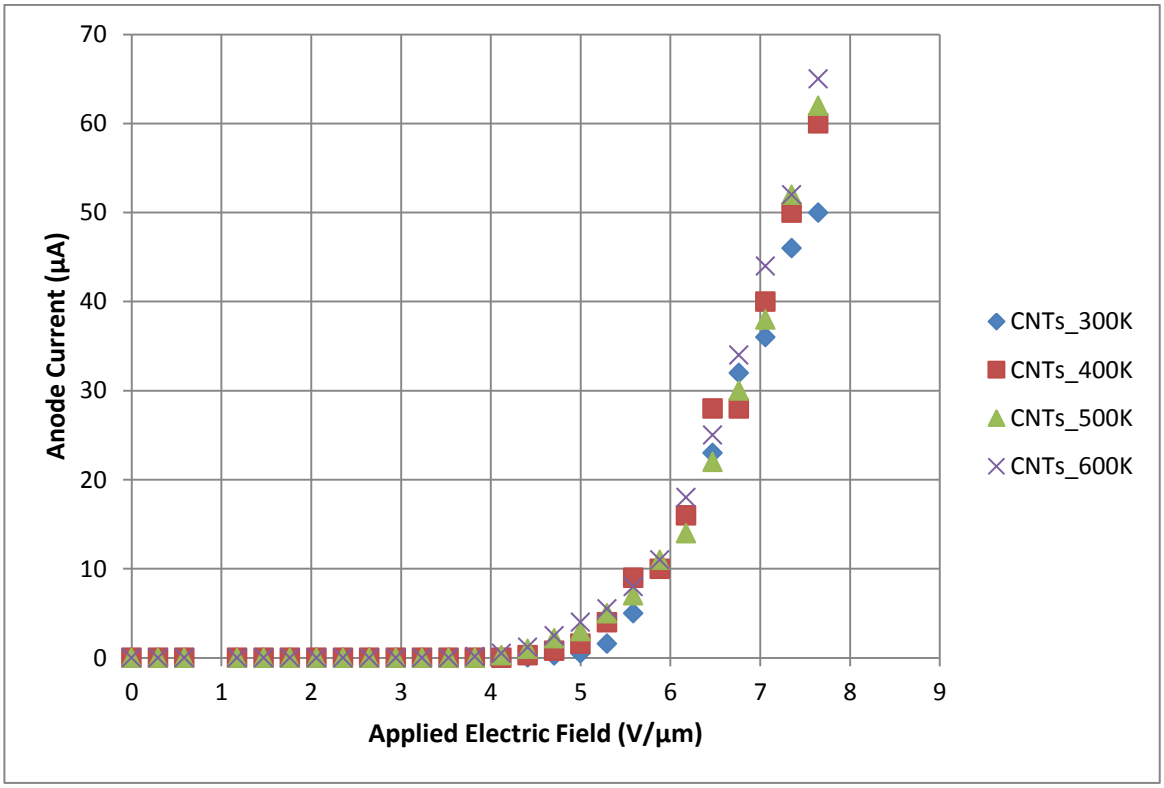

Figure 70: Thermionic emission curves of CNTs at 300K, 400K, 500K and 600K.

Figure 70 indicates the thermionic emission curves of EPD grown CNTs, and the CNTs are quite stable as the temperature increases. The threshold field stays at 4.5 V/μm and the emission current also does not show a big difference. It is noted that CNTs are thermally stable until 2000K [163] and also follows the thermionic emission measurement of CNTs by M. C. Kan's group [71]. It is valuable to study the thermionic emission property of CNTs at higher temperature, as the experimental results of J. M. Elich's group, CNTs show the thermionic emission starts at round 1100K [75].

6.5 Summary

In this chapter, firstly, the preparation of the field and thermionic emission test samples was circulated. With the excimer laser processing technique, a nanostructured amorphous silicon based emitters were prepared. The growing conditions and results of CNTs test substrates by both EPD and CVD method were introduced and discussed.

Secondly in this chapter, the field emission and thermionic emission properties of excimer laser processed thin amorphous silicon and EPD developed carbon nanotubes were investigated. The purpose of this study is to adapt the ELP a-Si material and CNTs to be the thermionic emitter array of the novel photon enhanced solar thermal device.

The field emission measurements were examined in a vacuum chamber (~2×10^{-7} Torr) using a X-Y movable probe current detector. The measurement results of laser irradiated a-Si agree with the previously reported by our group [97, 136, 146]. And the field emission of CNTs appeared a better threshold voltage due to its nanometre - size diameter, high mechanical strength, high chemical stability, high electrical and thermal conductivity and sputter resistance. However, these properties make CNTs to be not suitable for the thermionic emitters application under 1000K condition, which also suggested by the literatures. On the other side, the amorphous silicon with excimer laser processing had a higher threshold field than that of CNTs, however, the a-Si:H emitters showed interesting experimental results that when the cathode temperature increased up to 600K with the

emission threshold field improved from 8V/μm to around 5.5V/ μm. It is deduced that when the temperature further increased, an enhanced threshold field can be obtained. This should be studied as further experimental work.

Due to this promising property, the excimer laser processed thin amorphous silicon can be adopted into the novel photon enhanced solar thermal device as the thermionic emission emitters, which have several merits: relative cheap, can be developed rapidly and large scalable by excimer laser processing, can be grown on various substrates including glass, metal coated glass substrates and on metal itself. The solar thermal energy converting device with excimer laser irradiated a-Si:H will be explained and discussed in the next chapter.

7 Development of the Novel Solar Thermal Device

In this chapter, a novel solar thermal device will be described and principles, measurements and device fabrication are also discussed. This device follows similar principles and structure as the PETE device which has been developed by Melosh's group in Harvard University [73]. However, in this case we have utilized cost effective material – amorphous silicon, efficient photon collector – black silicon and one-step, scalable micro-fabrication technique – excimer laser processing, which will make this solar thermal device to be a low-cost while efficient candidate in the renewable energy market. The internal structure of the resulting nanocomposite could be the key to efficient tuning of the thermal and electrical conductivity of the films for efficient emission.

7.1 Device Structure

The device was designed through a field emission device with basically using ELP a-Si as the key technology. In this device, as introduced before, a sun light absorber layer was fabricated by ELP thick a-Si layer, known as black silicon (bSi) while ELP thin a-Si as the thermionic emission emitters on the other side of the copper foil as shown in *figure 70*. A SiO_2 gate structure was then sputtered and patterned on the top of the emitter array to enhance the field and thermionic emission. The spacers between cathode and anode are mica films, which can provide a gap for the travel of the electrons and insulate the thermal transportation from the cathode to anode in the vacuum. The electrons were excited from the emitters and accelerated through the patterned gate then collected by the anode copper

plate to form the electrical loop to light the light bulb. The electricity formed in this solar thermal device is highly depending on the materials of the thermionic emission emitters.

This device ideally should work together with a thermionic energy converter to heat the cold water etc. on the anode side to maximize the usage of the heat, like the application proposed in Bergeron's report [77] that can simply heat the cold water using the waste heat. However, in this project study, we focused on the thermionic emission enhanced solar device part only, and the heat sink or water heating system can be the future work to integrate with the thermal device.

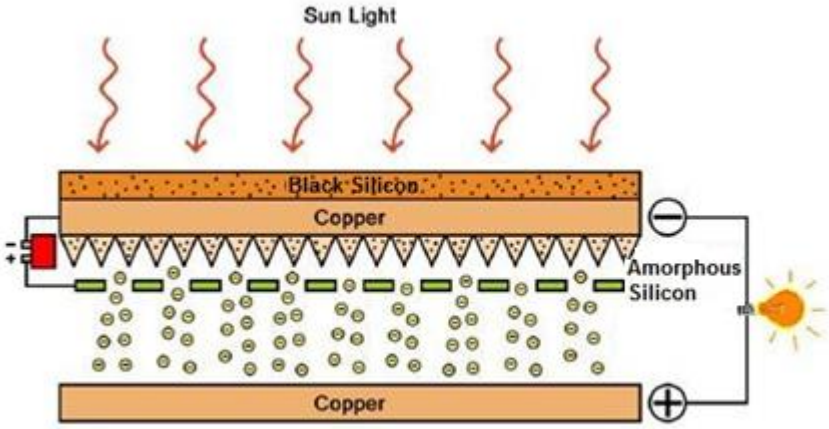

Figure 71: Schematic of a novel solar thermal device with black silicon as sun light absorber and ELP a-Si as emitters (reprint from [164]).

In *figure 71*, a bias supply was added in this case between the cathode and the gate to support the cathode material to reach the threshold field to start the emission. When the temperature on the cathode increases, the bias voltage could be reduced gradually. This is highly dependent on the cathode materials, for example, diamond material [165, 166] or graphene based materials [167]. The vacuum gap between cathode and anode is the path for the emitted electrons accelerate and travel, and the dimension of the vacuum gap is dependent on the emitting materials through equation

7.1 below. F is electric field and U is applied voltage with d is the dimension of the vacuum gap.

$$F = U/d \qquad (7.1)$$

The anode material in this study was a Cu plate, besides the following obvious merits, cost-effective, robust with good electrical conductivity, a high thermal conductivity 401 $Wm^{-1}K^{-1}$ [144] allows Cu to be a promising material of the heat sink, which allows rapid transfer of the waste heat to the integrated system, for example, solar water heating etc. as well as minimizing the electrons backflow. As this thermionic energy device works in a vacuum condition, the influence of the heat oxidization of Cu can be minimized. In fact, the anode should be a lower work function material to obtain higher activated electron and better device efficiency [168]. The work function of Cu is 4.5eV, and the 0.9eV of phosphorus-doped polycrystalline diamond films, which is the lowest work function material reported as the emitting material [71].

7.2 Device Working Principle

The solar thermal device purposed in this study, as described previously, adopted the black silicon film as the sun lights collector and the thermionic emission module to generate electrons to form the electrical loop.

Thermal testing of the excimer laser developed black silicon film on Cu foil illuminated the enhancement of the sun light absorption and transfer of heat to the other side of the Cu foil, on which the ELP a-Si thermionic emission emitter array located. *Figure 72* shows the real time thermal transportation experiment setup of the black silicon film on Cu foil. In this experiment, a Bentham (Air Mass = 1.5) light source was adapted as the sunlight source and K type thermocouples were used to monitor the real time temperatures on the both sides of the Cu foil.

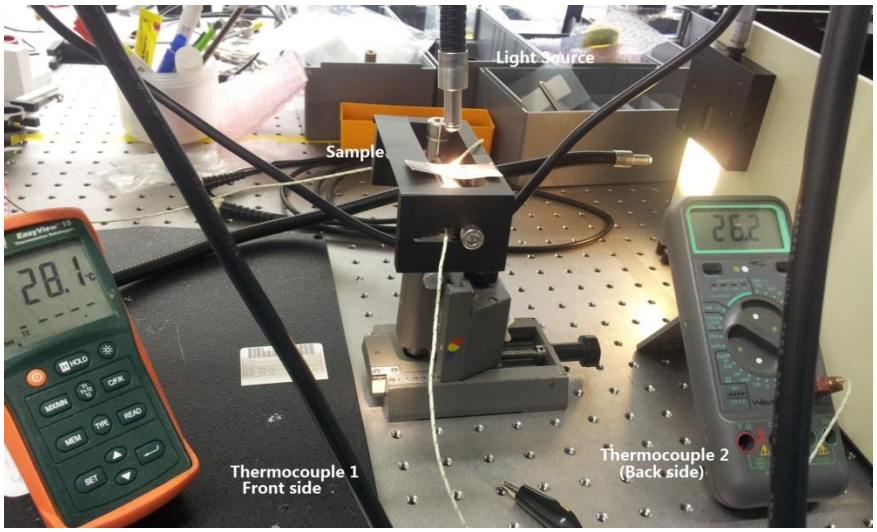

Figure 72: The experimental setup of the real time temperature with Bentham white light source (solar light simulator), thermocouples and thermal meter.

In *table 7* and *table 8* below, the real time temperature experiments were carried on a sample with bSi as the sun light absorber and thermionic emission array on the other side as well as the temperature on a pure Cu foil without any additional films. In *figure 73*, a plot of the real time temperature on both samples was revealed. It summarized a clear temperature difference from the samples with and without bSi absorber film. The distance between the light source and substrates was kept at 3 cm. It showed an average 30 K between the sides facing to the light source of the 2 substrates since shining the lights over 10 minutes. On the back side of the Cu, the temperature of the sample with black silicon layer increased steadily with the time while the temperature trended to be stable at 315 K on the back side of the pure Cu foil.

Time (minutes)	Temperature on bSi side (sun lights absorbing side, K)	Temperature on TE array side (K)
0	295	295
10	338.4	319.8
20	340.8	327.5
30	342.6	336.9
40	342.8	348.7
50	343.5	355.1
60	343.9	368.9

Table 7: Real time temperature on the bSi film and Thermionic emission array sides with time from 10, 20, 30, 40, 50 and 60 minutes under sun light simulator.

Time (minutes)	Temperature on the surface of Cu foil (facing to sunlight, K)	Temperature on the back side of the Cu foil (K)
0	295	295
10	308.1	300.1
20	312.8	303.1
30	320.6	309.9
40	324.8	314.5
50	327.9	316.0
60	329.2	317.8

Table 8: Real time temperature on the both sides of pure Cu foil without any additional films with time from 10, 20, 30, 40, 50 and 60 minutes under sun light simulator.

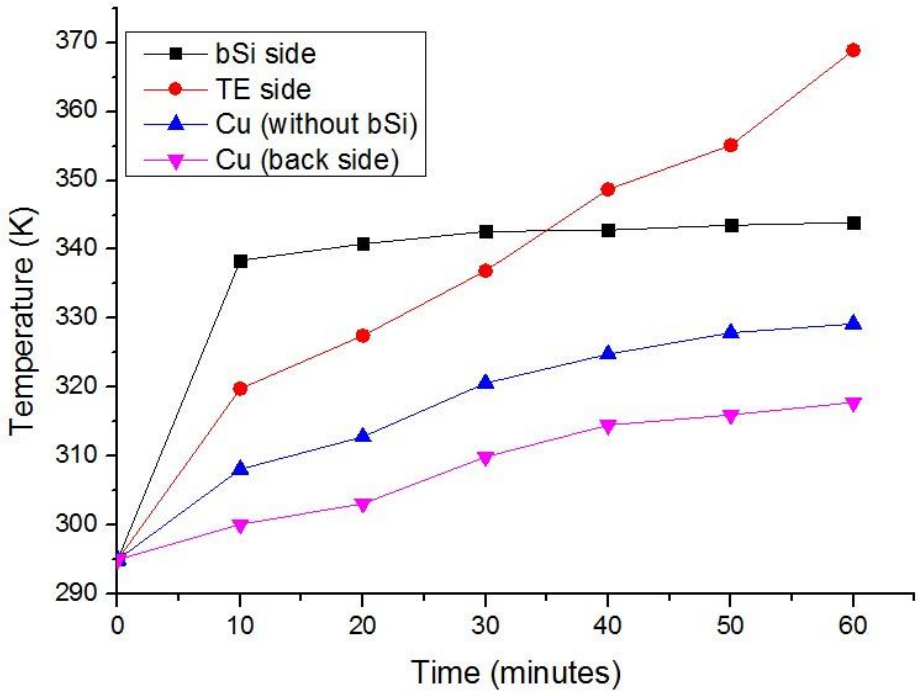

Figure 73: Real time temperature of the Cu foil with bSi absorber and thermionic emission arrays as well as the temperature on both sides of a pure Cu foil.

The above experiments displayed the light-trapping and temperature enhancement with/without the black silicon film and the temperature was transferred to the thermionic emitters via a good heat conduction media.

It was believed that with increasing the light shining time, the temperature of the TE array on the back side of the Cu foil will be further enhanced which results in offering a better emission temperature for the emitting materials.

The cathode emitting material – laser processed amorphous silicon was developed by the mature PECVD technique and excimer laser processing microstructuring method. The Cu foil was first cleaned in the DI water diluted Ammonia (aqueous NH_3:H_2O= 1:9) in ultrasonic bath for 30 minutes to remove the surface oxidization and contaminations. Then the Cu foil was rinsed by IPA and properly dried by the nitrogen flowing gas. The Cu foil was not placed on the heat, which was used in the normal glass cleaning procedure to

evaporate the water wafers. This was because the Cu will be easily thermal oxidized. The a-Si:H precursor film was then deposited by the PECVD chamber. During the deposition process, the RF power was set at10 Watts with the precursor gas silane at flow rate of 75 sccm with the substrate was kept at 230 ^{o}C. The process time of growing 120 nm thick a-Si:H is roughly 15 minutes (growing rate ~ 8 nm/min) with the deposition chamber pressure kept at 100 mTorr.

In order to develop the microstructured emitting material, the excimer laser processing was adapted. The as-deposited a-Si:H was mounted into the laser processing chamber. LPX*pro*210(F) KrF excimer laser with 248 nm wavelength and 20 ns pulse duration was utilized in this research. The laser was set at 20 HZ and the ELP laser pulse energy was 120 mJ/cm^2 with a sample moving speed (laser scanning speed) of 2 mm/s. The laser processing parameters in this case was different as the field emitters fabricated in the Chapter 6.1.2 by using higher laser energy. This was because of the substrate materials. In Chapter 6.1.2 was metal coated glass while in this study was Cu foil, which has a higher thermal conductivity that will conduct to a heat loss. The micro conical silicon emitters by the ELP were observed in the SEM image in *figure 74*. Compared to the SEM images in *figure 61* on Al coated substrate, more pin holes were found in study, this was attributed to the high thermal conductivity of the Cu substrate during the a-Si:H deposition, and also the laser melted the a-Si:H easily with a certain laser pulse energy.

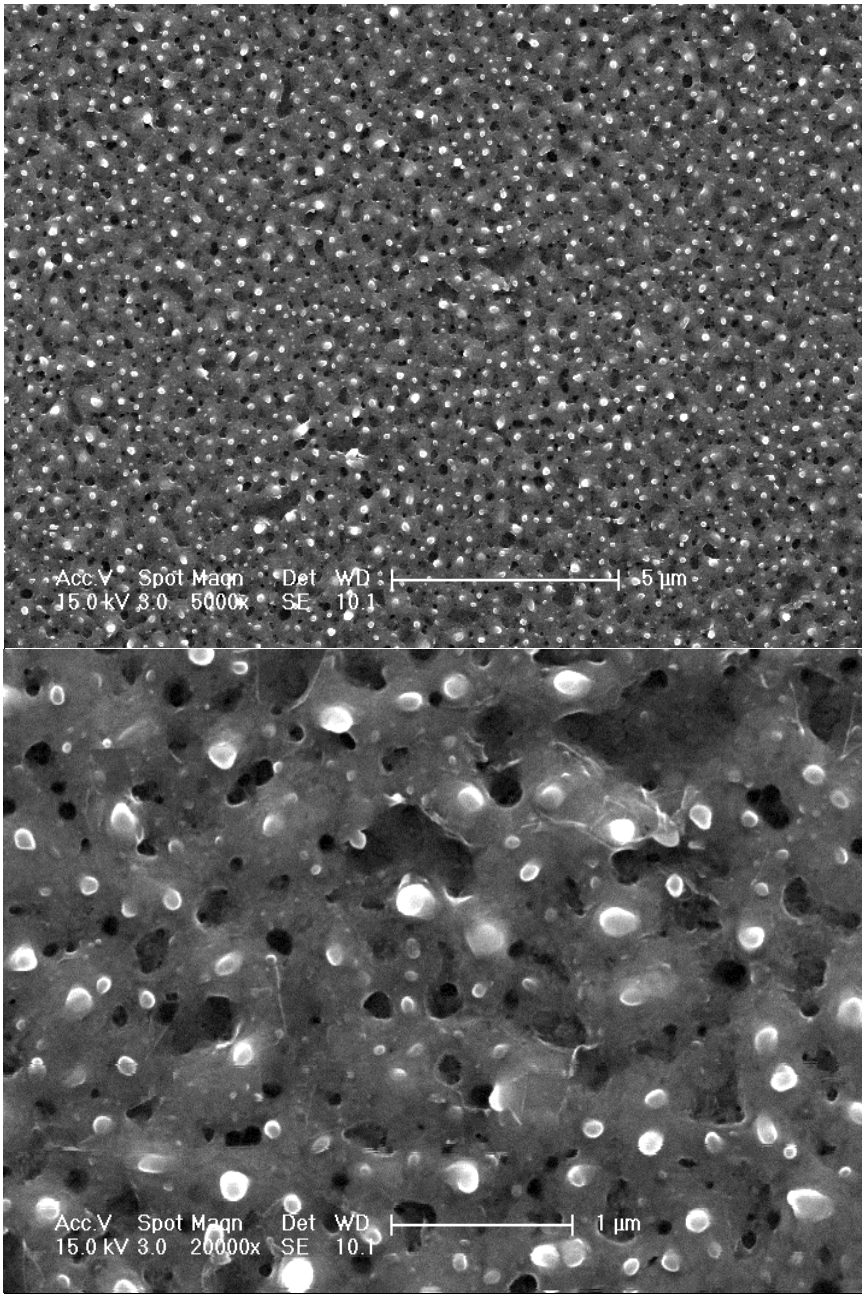

Figure 74: SEM images of ELP a-Si:H thermionic emitters.

In order to study the performance of the solar thermal device as well as investigating the carrier type, thermoelectric power (or thermopower / Seebeck coefficient) of the excimer laser fabricated thermionic emission emitters has been studied. The measurement chamber, detailed in Chapter 3.5.6, was established by the author. The measurement chamber was built with vacuum system in order to limit the heat transfer or heat loss as well as prevent the thermal oxidization of the substrates. The measurement can also be done in air atmosphere, however, with poor precision. This was useful for a quick check of the carrier type of the semiconductor materials.

The results of the Seebeck coefficient (S) can explore the majority carriers of the films that for pure n-type semiconductor materials which have only electrons (negative mobile charges), the electric field and temperature gradient should point in opposite directions in equilibrium that gives a negative S. Likewise, values for pure p-type semiconductor materials which have only holes (positive mobile charges), the electric field and temperature gradient should point in the same direction in equilibrium that gives a positive Seebeck coefficient value.

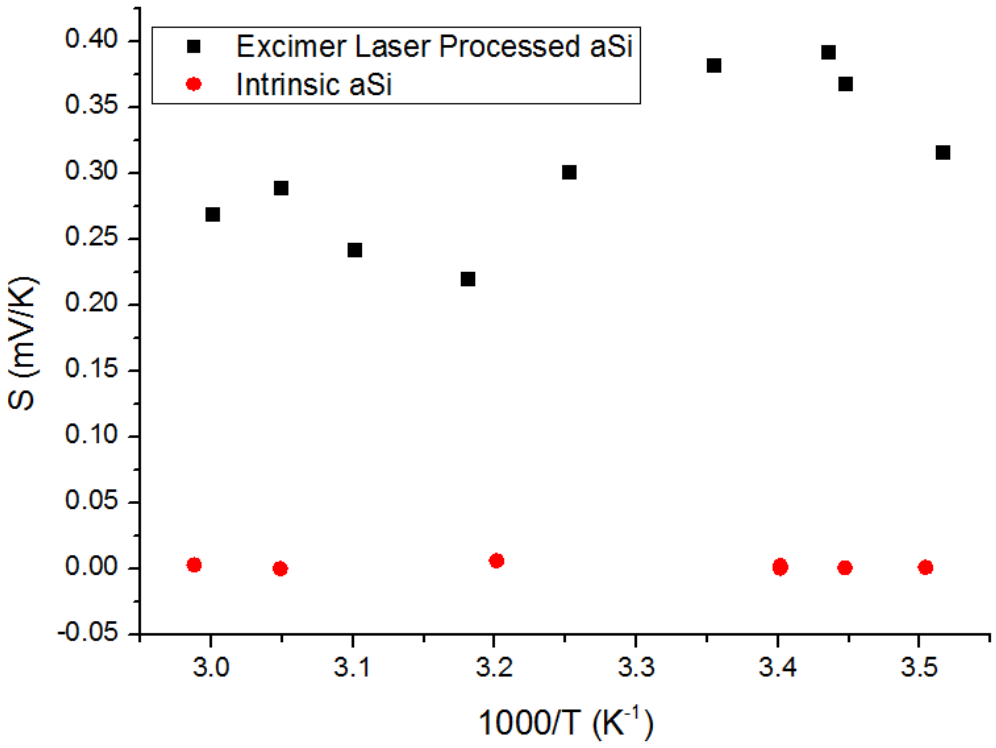

Figure 75: Thermopower of the intrinsic and excimer laser irradiated 100 nm amorphous silicon deposited on polished Cu foil.

In *figure 75*, the thermopower measurements of intrinsic and excimer laser processed a-Si films were studied. The positive Seebeck value of the ELP a-Si:H, average of 0.3mV/K, was obtained which indicates that the excimer laser processed a-Si:H on Cu foil emerges as p-type behavior. This was because during the excimer laser processing, the ELP melts the amorphous silicon as well as the bottom Cu substrate, and Cu nanoparticles were diffused into the molten a-Si:H and re-solidified to form a Cu doped a-Si as well as create the pathway for the electrons (*figure 76*), which resulted in a p-type material rather than the original intrinsic a-Si:H. The intrinsic a-Si:H film showed a near zero thermopower value due to no electron and hole pairs exchange in the intrinsic film. The carrier type of the semiconductors can also been confirmed by classical Hall Effect measurement.

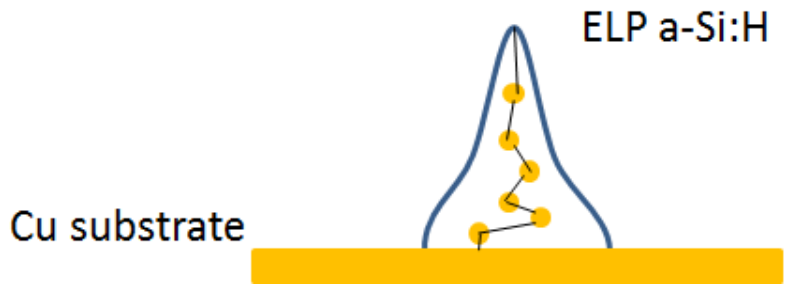

Figure 76: The mechanism of the ELP a-Si:H on Cu substrate.

The thermionic emission of the laser irradiated a-Si:H film was studied in *figure 77*.

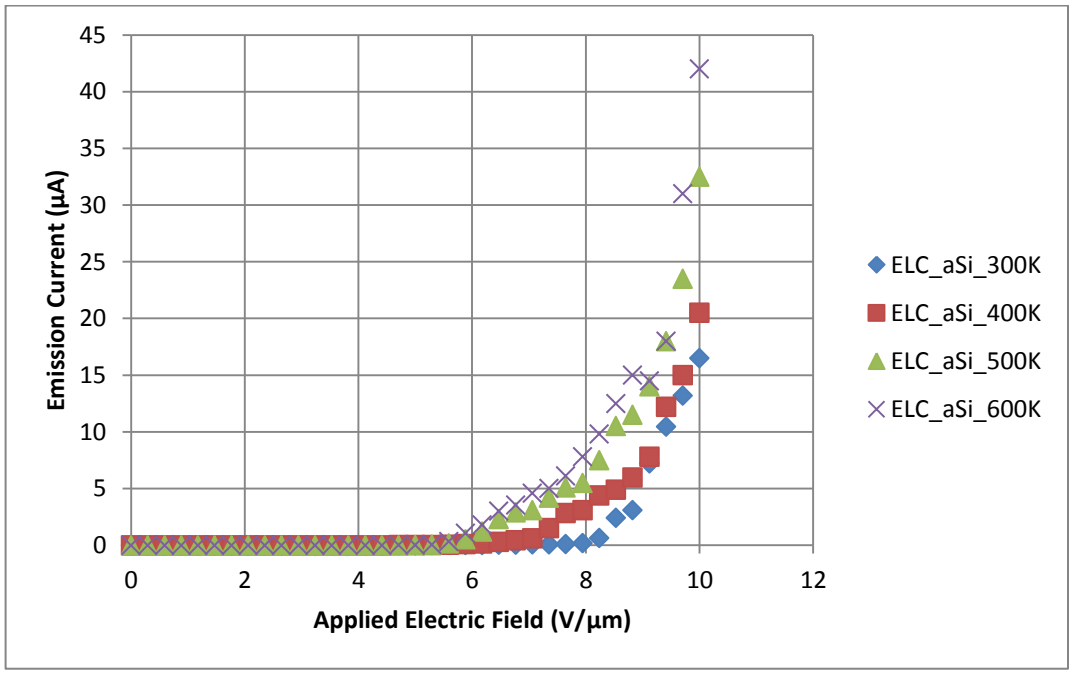

Figure 77: Thermionic emission curves of ELP a-Si films at 300K, 400K, 500K and 600K.

The above figure displayed the thermionic emission from ELP a-Si:H at various temperature, 300 K, 400 K, 500 K and 600 K. The threshold field was clearly improved from 7.8 V/μm to 5.5 V/μm while the emission current was also increased when the

temperature was raised from room temperature to 600 K. The maximum of the emission current of the emitting material at 600 K was up to 42 μA. This was higher than the thermionic emission current measured in previous a-Si:H on Al films.

The thermionic emission can be further enhanced by adding a gate structure, which has been used in several applications [55, 169]. SiO_2 is the best candidate as the gate structure in this study as this material has a high thermal and resistivity. In this thermal device, an optional bias was purposed to attach between the cathode and gate to support the emitting materials to free the electrons when they were heated up.

The work function ϕ, as mentioned in Chapter 2.5.1, together with temperature are the main factors which will determine the thermionic emission current density. As the device is going to be applied in high temperature surrounding to collect the waste heat, the temperature on the cathode material shall be considered as an external factor and the temperature can be enhanced through some optical concentration methods. Therefore, the work function is actually playing the most important role in the thermionic emitting materials. The excimer laser processed a-Si:H film as studied in this device, possesses 3.6 eV [170] while intrinsic a-Si:H is 4 eV. Even it is higher than the diamond material, the ELP a-Si:H has the advantage in cost effective, rapid development and large scalable, which are attractive to the real industry.

7.3 Summary

In this chapter, a solar thermionic energy device was purposed and studied. The black silicon layer as the sun light collector studied in Chapter 4 and the excimer laser processed a-Si:H examined in Chapter 6 were adapted into this device. These two layers were grown on the two sides of the thin Cu foil, which was different from the substrates used in previous studies and experiments. This device is a vacuum based device that all the experiments were carried out in the vacuum chamber, and the spacer materials used in this application was 1.7 μm mica films.

It was also demonstrated that the heat can be absorbed by the black silicon film on the Cu foil and transferred to the other side that the materials can use as the thermal source for activating the thermionic emission. The nanocomposited emitting materials were developed by the excimer laser processing technique of a-Si:H film and Cu substrate, resulting in an promising property in thermionic emission. The measurements displayed an clear enhancement of the threshold field and the increase of the anode current.

In the device design, some thermionic emission enhanced methods can also be linked to the device. The external bias could support the electrons to be freed from the emitting material. However, to obtain a total positive electricity output of the device, the bias voltage should be lower than the output voltage. The other way was to add a SiO_2 gate structure to enhance the field/thermionic threshold field and strength the device performance. These need to be further studied and investigated.

This device shall work excellent in high temperature and the higher the better. Due to the limitation of the heat source in the thermionic emission measurements, the author did not have the chance TO examine the temperature higher than 600 K of ELP a-Si:H materials. This novel thermal device is able to take advantage of the waste heat, which will be very attractive to the industries as this research required cost effective materials, rapid processing laser processing, which are able to produce large size of the device. The device

idea can also be very interesting in the applications in the space, such as the satellite that can solve the vacuum degrade issue.

8 Summary and Further Work

A general summary of the studies of this PhD research is presented in this chapter. Conclusions and suggestions for the future work on the p-i-n junction nanowire solar device and the solar thermal converter application are also discussed in this chapter.

8.1 Summary

In this PhD work, all the studies were emphasized on amorphous silicon material and excimer laser processing technique and novel solar energy applications. In these studies, amorphous silicon films were grown by PECVD system with introducing silane and film thickness was controlled by the processing time. The novel excimer laser processing is a rapid thin film process which is able to produce large scale samples. In this study, from the field emission and thermionic emission results, the excimer laser irradiated and crystallized amorphous silicon was adapted as emitters for the application of the novel solar thermal converter. In this application, 'black silicon' film was studied as the solar light absorber. To growing bSi film, thicker a-Si was deposited on Cu foil and then the excimer laser processing was carried out to create the micro-structure which can enhance the light absorption as well as transfer the heat to the thermionic emitters with less thermal loss.

In parallel, the promising technique of fabricating bSi film was adopted to develop a n-i-p junction amorphous silicon nanowire solar cell. Different from the classical planar a-Si solar cell, this n-i-p nanowire device can trap the lights to enhance the solar cell efficiency. The p and n type were developed by using excimer laser doping Al and N_2 with intrinsic a-Si, and determined by thermopower measurements. In this study, a solar cell efficiency of 0.1% was initially obtained, however, with some future optimization steps, for example, p, i and n layers thickness control , interface removing and cell design, the

excimer laser processed silicon nanowire device will be able to show a good potential in clean energy devices.

8.2 Future Work

In this PhD study, several works have been done, such as nanowire solar cell, excimer laser processing, field emission and thermionic emission and a solar thermal energy device. Due to the time limitation and other issues, there are still several things that can be added to my researches to improve the device performances. In this section, a list of some possible works is to discuss.

8.2.1 p-i-n Single Junction Nanowire Solar Cell Design

Besides the n-i-p nanowire structure described in Chapter 5, a p-i-n superstrate can also be developed by ELP as shown in *figure 78*. General speaking, a p-i-n solar cell structure always having higher efficiency than a n-i-p one.

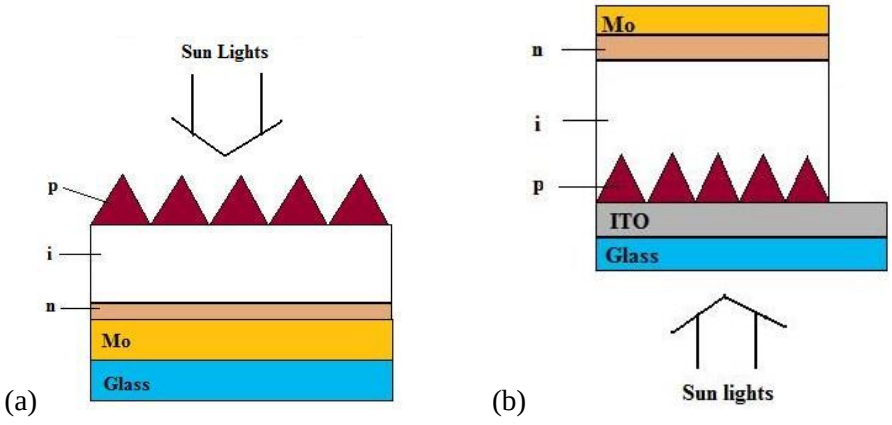

Figure 78: Two possible p-i-n silicon nanowire PV cells structures.

The first method is to develop a laser processed and doped n a-Si with an 500 – 600 nm intrinsic a-Si on the top as after laser processing, this a-Si:H layer will be divided into a nanowire structure and original laser untreated layer. Then ELP is carried to fabricate nanowires followed by a thin layer of Al (~ 30nm) on the top. The substrate is then annealed by 400 degree for 4 hours to dope the Al into the nanowires. This doping process is known as Aluminum Induced Crystallization (AIC). In this structure, the standard PV industry back metal contact Mo with 100 nm thickness is used. The device idea is shown in *figure 78 (a).*

The second way is adopting traditional method of developing p- i- n a-Si:H thin film SC based on commercial TCO glasses. In our lab, ITO could be used as the conducting layer and also anti- reflection layer. In this method, sun lights come to the glass side, photons go through the ITO and bombard the p a-Si:H to activate the PV effect, the device structure is shown in *figure 78 (b).* Intrinsic and n type layers are deposited exactly same ways as in n-i-p structures. Mo contact (100 nm) is deposited and patterned on the top of the n layer as the contact. However, in this structure, the light trapping effect from the microstructured a-Si:H might not be as strong as in the n-i-p structure but the ITO layer can contribute the lights absorbing.

In addition, to optimize the performance of the device and solve the interfaces between layers, argon plasma etching can be used to remove the oxide layer or clean the surface of the air-exposed film when the samples move between one processing chambers.

The thermopower measurement in the solar thermal device was just taken on a particular laser energy processed a-Si. In the future, it will be valuable to measure the thermopower on various laser energies irradiated amorphous silicon films to have a comprehensive understanding of laser processing of the material.

8.2.2 Improvements of Solar Thermionic Generator

Due to the heater capacity in the thermionic emission measurement, the author did not have chance to study the ELP a-Si above 600K. It will be very interested to investigate this novel material by higher temperature in thermionic emission with mechanical controlled probe, which can provide precious control on the gap distance between cathode and anode and then a comparison among CNTs, Diamond materials and ELP a-Si film can be made.

The solar thermal converter device was characterized in a vacuum chamber, and if the vacuum sealing technique can be adapted in the solar thermal device, a portable protype can be developed for a better measurements, cost assessment and public demonstration.

The solar thermionic energy device in this PhD study was focused on a-Si:H material, which is a good but not excellent cathode material regarding to the threshold field and current density. However, In order to maximize the emission from the cathode array, some materials such as phosphors doped diamond film (very low work function material) by CVD method or carbon relative materials – graphene or GaN semiconductors can be investigated as several research institutes have demonstrated the excellent thermionic emission ability and low cost fabrication methods of it.

References

[1] B. Goss, *Choosing Solar Electricity*, Centre for Alternative Technology 2010

[2] K. A. Tsokos, *Physics for the IB Diploma*, Cambridge University Press 2008

[3] CRC Handbook of Chemistry and Physics

[4] www.wiki.com

[5] J. Zhao, A. Wang, M. Green and F. Ferrazza, *Applied Physics Letters* **73**, 1991-1993 (1998)

[6] O. Schultz, S. Glunz, G. Willeke, *Progress in Photovoltaics: Research and Applications 2004* **12**, 553-558 (2004)

[7] S. Benagli, D. Borrello, E. Vallat-Sauvain, J. Meier, U. Kroll, J. Hotzel, J. Spitznagel, J. Steinhauser, L. Castens and Y. Djeridane, *24th European Photovoltaic Solar Energy Conference*, in Hamburg, (September 2009)

[8] M. Green, K. Emery, Y. Hishikawa, W. Warta and E. Dunlop, *Progress in Photovoltaics: Research and Applications* **21**, 827-837 (2013)

[9] T. Todorov, J. Tang, S. Bag, O. Gunawan, T. Goken, Y. Zhu and D. Mitzi, *Advanced Energy Materials*, (2012)

[10] B. Kayes, H. Nie, R. Twist, S. Spruytte, F. Reinhardt, I. Kizilyalli and G. Higashi, *Proceedings of the 37th IEEE Photovoltaic Specialists Conference*, (2001)

[11] A. Greene, greenrednecks.com (2009)

[12] D. Kraemer, B. Poudel, H. S. Feng, J. C. Caylor, B. Yu, X. Yan, Y. Ma, X. Wang, D. Wang, A. Muto, K. McEnaney, M. Chiesa, Z. Ren and G. Chen, *Nature Materials* **10**, 532-538 (2011)

[13] P. Manning, *Business Day* (2009)

[14] R. Newman, *Phys. Rev. Lett.*, **100**(2), 700-703 (1955)

[15] P. J. Cousins, D. D. Smith, H. C. Luan, J. Manning, T. D. Dennis, A. Waldhauer, K. E. Wilson, G. Harley and G. P. Mulligan, *35th IEEE PVSC* (2010)

[16] M. A. Green, *Chapter 4: Crystalline Silicon Solar Cells*, World Scientific 2001

[17] D. Niinobe, K. Nishimura, S. Matsuno, H. Fujioka, T. Katsura, T. Okamoto, T. Ishihaha, H. Morikawa and S. Arimoto, *23rd European Photovoltaic Solar Energy Conference and Exhibition* (2008)

[18] D. E. Carlson, C. R. Wronski, J. I. Pankove, P. J. Zanzucchi, D. L. Staebler, *RCA Review* **(38)**, 211-225, (June 1977)

[19] D. E. Carlson and C. R. Wronski. *Appl. Phys. Lett.* **28**, 671 (1976)

[20] K. Zweibel, *Harnessing Solar Power: the Photovoltaic Challenge*, Plenum Publishing Corporation 1990

[21] A. Catalano, R. D'Aiello, J. Drensner, B. Faughnan, A. Firester, J. Kane, H. Schade, Z. E. Smith, G. Swartz, A. Triano, *Proceedings of the 16th IEEE Photovoltaic Specialists Conference*, 1421- 1422 (1982)

[22] B. M. Kayes, H. A. Awater and N. S. Lewis. *J. Appl. Phys.***97** (11), 114302 (2005)

[23] D. Derkacs, S. H. Lim, P. Matheu, W. Mar and E. T. Yu, *Appl. Phys. Lett.* **89**, 093103 (2006)

[24] T. Soderstrom, F. J. Haug, V. Terrazzoni- Daudrix and C. Ballif. *J. Appl. Phys.* **103**, 114509 (2008)

[25] V. Terrazzoni- Daudrix, J. Guillet, X. Niquille, L. Feitknecht, F. Freitas, P. Winkler, A. Shah, R. Morf, O. Parriaux and D. Fischer. *3rd World PVSC*, 2003

[26] J. Yang, A. Banerjee and S. Guha. *Appl. Phys. Lett.* **70**, 2975- 2977 (1997)

[27] J. Meier, R. Fluckiger, H. Keppner and A. Shah. *Appl. Phys. Lett.* **65**, 860 (1994)

[28] B.Yan, G. Yue, X. Xu, J. Yang and S. Guha. *Phys. Status Solidi A* 207 (**3**), 671- 677 (2010)

[29] B. Yan, G. Yue, J. Yang and S. Guha, *Proceeding of the 33rd IEEE PVSC* paper No. **257**, (May 2008)

[30] K. L. Chopra and S. R. Das, *Thin Film Solar Cells*, Plenum Press 1983

[31] B. T. Debney, *Solid- State and Electron Device*, **2**, special issue, s15- s17 (June 1978)

[32] A. A. Damitha, T. Adikaari, S. Ravi, P. Silva, M. J. Kearney and M. Shannon, *Mater. Res. Soc. Symp. Proc.* (**836**), L8.2.1- L8.2.6 (2005)

[33] E. Garnett and P. Yang. *Nano Lett.* **10**, 1082-1087 (2010)

[35] M .M. Adachi, M. P. Anantram and K. S. Karim. *Nano Lett.* **10**, 4093-4098 (2010)

[36] E. Garnett and P. Yang. *J. AM. CHEM. SOC.* **130**, 9224-9225 (2008)

[37]L. Tsakalakos, J. Balch, J. Fronheiser and B. A. Korevaar. *Appl. Phys. Lett.* **91**, 233117 (2007)

[38] S. Thiyagu, Z. Pei, M. S. Jhong. *Nanoscale Research Letters* **7**,172 (2012)

[39] J. Zhu, Y. Xu, Q. Wang and Y. Cui. *Photovoltaic Specialists Conference (PVSC), 35th IEEE* , 453- 456 (June 2010)

[40] J. Kim, A. J. Hong, J. Nah, B. Shin, F. M. Ross and D. K. Sadana. *ACS Nano* **6** (1), 265- 271 (2012)

[41] *Z. Pei, S. Chang, C. Liu and Y. Chen. IEEE Electron Device Lett.* **30** (12), 1305- 1307 (2009)

[42] J. Nelson, *The Physics of Solar Cells*, Imperial College Press 2003

[43] D. N. R. Payne, S. A. Boden, O. D. Clark, A. E. Delahoy and D. M. Bagnall, *35th IEEE Photovoltaic Specialists Conference*, (2010)

[44] C. G. Bernard, *Endeavour* **26**, 79- 84 (1967)

[45] P. B. Clapham and M. C. Hutley, *Nature* **244**, 281- 282 (1973)

[46] Y. F. Huang, S. Chattopadhyay, Y. J. Jen, C. Y. Peng, T. A. Liu, Y. K. Hsu, C.L. Pan, H. C. Lo, C. H. Hsu, Y. H. Chang, C. S. Lee, K. H. Chen, L. C. Chen, *Nature Nanotechnology* **2**(12), 770–774 (2007)

[47] H. Toyota, K. Takahara, M. Okano, T. Yotsuya, H. Kikuta, *Japanese Journal of Applied Physics Part 2*, **40**(7B), L747–L749 (2001)

[48] S. A. Boden and D. M. Bagnall, *Progress in Photovoltaics: Researches and Applications*, **18**, 195–203, (2010)

[49] M. A. Green, *Silicon Solar Cells: Advanced Principle & Practice*, University of New South Wales 1992

[50] R. Biswas, J. Bhattacharya, B. Lewis, N. Chakravarty, V. Dalal, *Solar Energy Materials and Solar Cells*,**94**(12), 2337–2342 (2010)

[51] N. G. Basov, V. A. Danilychev, Y. Popov and D. D. Khodkevich. *Zh. Eksp. Fiz. i Tekh. Pis'ma. Red.* **12**, 473 (1970)

[52] T. Sameshima, S. Usui and M. Sekiya, *IEEE Electron Device Lett., vol. EDL-***7**, 276-278 (1986)

[53] J. B. Boyce, P. Mei, R. T. Fulks, and J. Ho, *Phys. Stat. Sol.* **166**, 729-741 (1998)

[54] P. Mei, J. B. Boyce, M. Hack, R. A. Lujan, R. I. Johnson, G. B. Anderson, D. K. Fork and S. E. Ready. *Appl. Phys. Lett.* **64**(8), 1132- 1134 (February 1994)

[55] S. R. P. Silva, R. D. Forrest, D. A. Munindradasa and G. A. J. Amaratunga, *Diamond Relat. Mater.* **7**, 645 (1998)

[56] Street (Ed.), *Technology and Applications of Amorphous Silicon*, Springer (1999)

[57] T. Sameshima, M. Hara, S. Usui, Jpn. *J. Appl. Phys*. Part 1 **28**, 1789 (1989)

[58] R. B. Bergmann, J. Kohler, R. Dassow, C. Zaczek, J. H. Werner. *Phys. Stat. Sol. (a)* **166**, 729 (1998)

[59] C. Liu, X. Jia, B. Ai, J. Lai, Y. Deng and H. Shen. *American Journal of Engineering and Technology Research* **11**(12), 1033-1035 (2011)

[60] H. Azuma, A. Takeuchi, T. Ito, H. Fukushima, T. Motohiro and M. Yamaguchi. *Solar Energy Materials & Solar Cells* **74**, 289-294 (2002)

[61] J. R. Woodyard, 'Nonlinear Circuit Device Utilizing Germanium' issued 1950-11-14

[62] U.S. Patent 2,631,356, K. Teal and M. Sparks, 'Method of Making P-N Junctions in Semiconductor Materials', issued 1953-03-17

[63] S. K. Zhang, K. Sugioka, J. Fan, K. Toyoda and S. C. Zou, *Appl. Phys. A* **58**, 191-195 (1994)

[64] S. Chichibu, T. Nii, T. Akane, and S. Matsumoto, *J. Vac. Sci. Technol. B* **11**(2), 341 (1993)

[65] A. Slaoui, F. Foulon, R. Stuch and P. Siffert, *Appl. Phys. A* **50**, 479-484 (1990)

[66] K. Sugioka, K. Toyoda, *Appl. Phys. Lett.* **55**(7), 619-621 (1989)

[67] D. Yang, J. Lu, Y. Shen, D. Tian, X. Ma, L. Li, D. Que, *International Conference on Solid State Crystals*, in Zekopane (October 2000)

[68] M. Shao, L. Cheng, M. Zhang, D. D. D. Ma, J. A. Zapien, S. T. Lee and X. Zhang, *Appl. Phys. Lett.* **95**, 143110 (2009)

[69] R. H. Fowler and L. Nordheim. *Proc. Roy. Soc*., **A119**, 173 (1928)

[70] B. H. Bransden, C. J. Joachin, *Introduction to Quantum Mechanics*, Longman Scientific and Technical (1989)

[71] K. H. Bayliss and R. V. Latham, *Proc. R. Sco*. A **403**, 285 (1986)

[72] Y. F. Tang, PhD Thesis, University of Surrey (2002)

[73] G. A. J. Amaratunga and S. R. P. Silva. *Appl. Phys. Lett.* **68**, 2529 (1996)

[74] X. W. Zhang et al. *Thin Solid Film* **429**, 261-266 (2003)

[75] C. H. P. Poa and S. R. P. Silva. *Vacuum Nanoelectronics Conference (IVNC)*, 76- 77 (July 2004)

[76] C. A. Spindt, *Journal of Applied Physics* **39** (7), 3504-3505 (1968)

[77] C. A. Spindt, I. Brodie, L. Humphrey and E. R. Westerberg. *Journal of Applied Physics* **47**, 5248-5263 (December 1976)

[78] Access Science

[79] S. Iijima. *Nature* **354**, 56- 58 (1991)

[80] S. Iijima, and T. Ichihashi. *Nature* **363**, 603- 605 (1993)

[81] D.S. Bethune, C.H. Kiang, M.S. De Vries, G. Gorman, R. Savoy, J. Vazquez, and R. Beyers. *Nature* **363**, 603-605 (1993)

[82] W. A. de Heer, A. Chatelain and D. Ugarte. *Science* **270**, 1179- 1180 (1995)

[83] H .Murakami, H. Hirakawa, C. Tanaka and H. Yamakawa. *Appl. Phys. Lett*. **76**(13), 1776 (2000)

[84] M. S. Dresselhaus, G. Dresselhaus and P. Avouris. *Topics in Appl. Phys.* **80**, (2000)

[85] Y. Chen, S. Patel, Y. Ye. *Appl. Phys. Lett.* **73**(15), 2119 (1998)

[86] S. Hofmann, C. Ducati, B. Kleinsorge. *Appl. Phys. Lett.* **83**(22), 4661 (2003)

[87] R. G. Lacerda, F. Wyczisk and M. Chhowalla. *J. Appl. Phys.* **96**(8), 4456 (2004)

[88] Q. S. Goher, Y. Fan and M. J. Rose. *Proceedings of the 2nd International Conference on Nanotechnology: Fundamentals and Applications*, 304 (July 2011)

[89] W. B. Choi, D. S. Chung, J. H. Kang, H. Y. Kim, J. W. Jin, I. T. Han, Y. H. Lee, J. E. Jung, N. S. Lee, G. S. Park and J. M. Kim. *Appl. Phys. Lett.* **75**(20), 3129-3131 (1999)

[90] R. C. Smith, D. C. Cox and S. R. P. Silva. *Appl. Phys. Lett.* **87**,103112 (2005)

[91] Y. Cheng and O. Zhou. *C. R. Physique* **4**, 1021-1033 (2003)

[92] L. Chen and M. M. El-Gomati. *Ultramicroscopy* **97**, 135- 140 (1999)

[93] A. A. Evtukh, E. B. Kaganovich, V. G. Litovchenko, M. Y. M. Litvin, D. V. Fedin and E. G. Manoilov. *Semiconductor Physcis, Quantum Electronics & Optoelectronics.* **3**(4), 474-478 (2000)

[94] X. D. Bai, C. Y. Zhi, S. Liu, E. G. Wang and Z. L. Wang. *Solid State Communications* **125**, 185-188 (2003)

[95] B. W. Han, J. S. Lee and B. T. Ahn. *IEEE Electron Device Letters* **23**(1), 10-12 (January 2002)

[96] H. Wu, T. Tsai, F. Chu, N. Tai, H. Lin, H. Chiu and C. Lee. *J. Phys. Chem. C* **114**, 130-133 (2010)

[97] Y. Fan, M. J. Rose, S. K. Persheyev and M. Z. Shaikh. *IEEE, International Symposium on Photonics and Optoelectronics*, (2009)

[98] W. Zhu, G. P. Kochanski and S. Jin. *Science* **282**(20), 1471-1473 (1998)

[99] W. P. Kang, J. L. Davidson, A. Wisitsora-at, Y. M. Wong, R. Takalkar, K. Holmes and D. V. Kerns.. *Diamond & Related Materials* **13**, 1944-1948 (2004)

[100] N. A. Fox, W. N. Wang, T. J. Davis, J. W. Steeds and P. W. May. *Appl. Phys. Lett.* **71**(16), 2337-2339 (1997)

[101] S. R. P. Silva, G. A. J. Amaratunga and K. Okano. *J. Vac. Sci. Technol. B* **17**(2), 557-561 (March/April 1999)

[102] P .W. May, S. Hohn and M. N. R. Ashfold. *J. Appl. Phys.* **84**(3), 1618-1625 (August 1998)

[103] S. F. Ahmed, S. Das, M. K. Mitra and K. K. Chattopadhyay. *Proc. Of ASID `06*, 440-443 (October 2006)

[104] C. R. Crowell, *Solid-State Electronics* **8** (4), 395–399 (1965)

[105] M. E. Kiziroglou, X. Li, A. A. Zhukov, P. A. J. De Groot, C. H. De Groot. *Solid-State Electronics* **52** (7), 1032–1038 (2008)

[106] M. C. Kan, J. L. Huang, J. C. Sung, K. H. Chen and B. S. Yau. Carbon **41**, 2839-2845 (2003)

[107] F. A. M. Koeck, J. M. Garguilo, B. Brown and R. J. Nemanich. *Diamond & Related Materials* **11**, 774- 779 (2002)

[108] F. A. M. Koeck, R. J. Nemanich, A. Lazea, K. Haenen. *Diamond & Related Materials* **18**, 789- 791 (2009)

[109] F. A. M. Koeck, Y. Yang and R. J. Nemanich. *Industrial Electronics Society*, 31st Annual Conference of IEEE, 2389- 2394 (November 2005)

[110] D. C. Cox, R. D. Forrest, P. R. Smith and S. R. P. Silva. *Appl. Phys. Lett.* **85** (11), 2065- 2067 (2004)

[111] P. Liu, Y. Wei, K. Jiang, Q. Sun, X. Zhang, S.Fan, S. Zhang, C. Ning and J. Deng. *Physical Review B* **73**, 235412 (2006)

[112] J. M. Elich, B. J. Landi, R. P. Raffaelle, T. Gennett, I. L. Krainsky, G. Landis and S. G. Bailey. *Proceedings of the First Int. Energy Conversion Engineering Conference: Portsmouth, VA* , 233- 236 (August 2003)

[113] J. H. Lee, I. Bargatin, J. Provine, W. A. Clay, J. W. Schwede, F. Liu, R. Maboudian, N. A. Melosh, Z. X. Shen and R. T. Howe. *PowerMEMS*, 149-152 (December 2009)

[114] L. Bergeron, *Stanford Report*, (August 2010)

[115] *Science Daily* (August 2010)

[116] G. P. Smestad. *Sol. Energy Mater. Sol. Cells* **82**, 227-240 (2004)

[117] T. E. Madey and J. T. Yates. *J. Vac. Sci. Technol*. **8**, 39-44 (1971)

[118] F. A. M. Koeck, R. J. Nemanich, A. Lazea and K. Haenen. *Diamond Relat. Mater.* **18**, 789-791 (2009)

[119] D. R. Mills, G. L . Morrison and P. Le Lievre. *EuroSun 2004 Conf. Proc.* (2004)

[120] J. W. Schwede, I. Bargatin, D. C. Riley, B. E. Hardin, S. J. Rosenthal, Y. Sun, F. Schmitt, P. Pianetta, R. T. Howe, Z. X. Shen and N. A. Melosh. *Nature Material **9*** (9), 762-767 (September 2010)

[121] C. B. Vining. *Nature* **451**, 132-133 (January 2008)

[122] Z. Dughaish. *Physica* B **322**, 205-223 (2002)

[123] K. Davami, J. S. Lee and M. Meyyappan, *Transactions on Electrical and Electronci Materials*, **12** (6), 227-233 (December 2011)

[124] R. Yang and G. Chen, *Mater Integr* **18** (9), 31-36 (2005)

[125] R. Venkatasubramanian, E. Siivola, T. Colpitts, B. O'Quinn, *Nature* **413**, 597-602 (2001)

[126] W. Xie, X. Tang, Y. Yan, Q. Zhang, T.M. Tritt, *Journal of Applied Physics* **105**, 113713 (2009)

[127] T.C. Harman, P.J. Taylor, M.P. Walsh, B.E. LaForge, *Science (New York)* **297**, 2229-2232 (2002)

[128] K. M. Blundell, *Concepts in Thermal Physics*, Oxford University Press 2006

[129] T. H. Her, R. J. Finlay, C. Wu, S. Deliwala and E. Mazur. *Appl. Phys. Lett*. **73**(12), 1673- 1675 (1998)

[130] C. H. Crouch, J. E. Carey, M. Shen, E. Mazur and F. Y. Genin, *Appl. Phys. A* **79**, 1635-1641 (2004)

[131] J. S. Yoo, I. O. Parm, U. Gangopadhyay, Kyunghae Kim, S. K. Dhungel, D. Mangalaraj, Junsin Yi, *Solar Energy Materials & Solar Cells* **90**, 3085-3093 (20060

[132] Y. Xia, B. Liu, J. Liu, Z. Shen, C.Li, *Solar Energy* **85**, 1574-1578 (2011)

[133] H. M. Branz, V. E. Yost, S. Ward, K. M. Jones, B. To and P. Stradins, *Appl. Phys. Lett.* **94**, 231121 (2009)

[134] S. Koynov, M. S. Brandt and M. Stutzmann, *Phys. Stat. Sol. (RRL)* **1** (2), R53- R55 (2007)

[135] H. P. Porte, D. Turchinovich, S. Persheyev, Y. Fan, M. J. Rose and P. U. Jepsen, *J Infrared Milli Terahz Waves*, **32**, 883- 886 (2011)

[136] Y. Fan, M. J. Rose, S. K. Persheyev, M. Z. Shaikh and C. Main. *ICCE-17 proceeding*, 239- 240 (2009)

[137] J. Perrin et al. Plasma Phys. Control, *Fusion* **42**, B353-B363 (2000)

[138]

[139] A. H. Mahan, J. Carapella, B. P. Nelson, M. Vanecek, I. Balberg, *J. Appl. Phys.* (**6**), 6728 (1991)

[140] P. Brogueira, J.P. Conde, S. Arekat, V. Che, *J. Appl. Phys.* (**79**), 8748 (1996)

[141] J. Doyle, R. Robertson, G. H. Lin, M.Z. He, A. Gallagher, *J. Appl. Phys.* (**64**), 3215 (1988)

[142] Intertek Group Plc., available via: http://www.intertek.com/analysis/microscopy/edx/

[143] J. D. J. Ingle and S. R. Crouch, *Spectrochemical Analysis*, Prentice Hall, New Jersey 1988

[144] T. Ashida, A. Miyamura, N. Oka, Y. Sato, T. Yagi, N. Taketoshi, T. Baba and Y. Shigesato, *Journal of Applied Physics*, **105**, 073709 (2009)

[145] The Engineering ToolBox, via: http://www.engineeringtoolbox.com/thermal-conductivity-d_429.html

[146] T. H. Her, R. J. Finlay, C. Wu and E. Mazur, *Appl. Phys.* ***A*** (70), 383-385 (2000)

[147] D. M. Goldie and S. K. Persheyev, *J Mater. Sci.* **41**, 5287-5291 (2006)

[148] A. Asadollahbaik, S. Boden, M. Charlton, D. Payne, S. Cox and D. Bagnall, *Optical Express*, **22** (S2), 402-415 (2014)

[149] H. P. Porte, D. Turchinovich, S. Persheyev, Y. Fan, M. J. Rose and P. U. Jepsen, *IEEE Transactions on Terahertz Science and Technology*, **3**(3), 331- 341 (2013)

[150] P. Vukusic and J. R. Sambles, *Nature* **424**, 825- 855 (2003)

[151] S. A. Boden and D. M. Bagnall, *Proceedings of the Fourth World Conference on Photovoltaic Energy Conversion*, Hawaii (2006)

[152] Q. Chen, G. Hubbard, P. A. Shields, C. Liu, D. W. E. Allsopp, *Appl. Phys. Lett*. **94**, 263118 (2009)

[153] D. Macdonald, A. Cuevas, M. Kerr, C. Samundsett, D. Ruby, S. Winderbaum and A. Leo, *Sol. Energy* **76**, 277 (2004)

[154] C. H. Sun, P. Jiang and B. Jiang, *Appl. Phys. Lett*. **92**, 061112 (2008)

[155] S. A. Boden and D. M. Bagnall, *Appl. Phys. Lett*. **93**, 133108 (2008)

[156] G. Tang and A. Abdolvand, *Optical Materials Express* **1**(8), 1425- 1432 (December 2011)

[157] D. S. Ghosh, L. Martinez, S. Giurgola, P. Vergani and V. Pruneri, *Opt. Lett.* **34** (3), 325- 327 (2009)

[158] K. V. Rajani, S. Daniels, P. J. McNally, F. Olabanji Lucas and M. M. Alam, *Phys. Status Solidi A* **207** (7), 1586- 1589 (2010)

[159] Kurt J. Lesker Company, *Technical Notes* (2013), http://www.lesker.com/newweb/Process_Instruments/processequipment_technotes.cfm

[160] S. Pei, J. Du, Y. Zeng, C. Liu and H. M. Cheng, *Nanotechnology* **20**, 235707 (2009)

[161] Q. Goher, PhD Thesis, University of Dundee (2012)

[162] M. Z. Shaikh, PhD Thesis, University of Dundee (2008)

[163] T. Yamamoto, K. Watanabe and E. R. Hernandez, *Carbon Nanotubes, Topics Appl. Physics* **111**, 165-195 (2008)

[164] J. C. M. Sung, K. Kan, M. Sung, J. L. Huang, E. Sung, C. P. Chen, K. H. Hsu and M. F. Tai, *NSTI- Nanotech* **2**, 193- 196 (2005)

[165] F. A. M. Koeck, R. J. Nemanich, Y. Balasubramaniam, K. Haenen and J. Sharp, *Diamond & Related Materials* **20**, 1229- 1233 (2011)

[166] T. Sun, F. A. M. Koeck, C. Zhu and R. Nemanich, *Applied Physics Letters* **99**, 202101 (2011)

[167] E. Starodub, N. C. Bartelt and K. F. Carty, *Applied Physics Letters* **100**, 181604 (2012)

[168] P. Yaghoobi, M. V. Moghaddam and A. Nojeh, *Applied Physics Letters Advances* **2**, 042139 (2012)

[169] G. C. Tettamanzi, A. Paul, G. P. Lansbergen, J. Verduijn and S. Lee, *IEEE ElectronDevice Lett.*, **31**(2), 150–152 (2010)

[170] Y. F. Tang, S. R. P. Silva, B. O. Boskovic, J. M. Shannon and M. J. Rose, *Applied Physics Letters* **80** (22), 4154- 4156 (2002)